Portal Imaging with Amorphous Selenium:

A Signal and Noise Analysis and Comparison with Fluoroscopic Systems

by

Dennis Mah

A thesis
submitted in conformity
with the
requirement of the degree of
Doctor of Philosophy
at the
University of Toronto

Department of Medical Biophysics
University of Toronto

Dennis Wai Mah
Doctor of Philosophy
Department of Medical Biophysics, University of Toronto
Convocation Year: 1997

Abstract

Conformal radiation therapy is being developed to increase cancer patient survival by closely tailoring the radiation dose distribution to match the shape of the tumour. For conformal therapy to be effective, improved patient position verification through portal imaging is required. Existing portal imaging systems produce poor images. By increasing the optical coupling, the x-ray quantum noise in a fluoroscopic portal imaging system was measured for the first time and compared to other sources of noise. It is shown that fluoroscopic systems are dominated by noise in the vacuum tube camera and although significant improvements in the SNR can be made by reducing this source of noise, practical clinical systems can only be made quantum noise limited up to a spatial frequency which is too low to optimize the dose distribution. Flat panel imaging systems currently show promise for improving image quality beyond that possible for fluoroscopic systems. Some of these systems use a photoconductor known as amorphous selenium (*a*-Se) as the sensor. Thus the signal and noise properties of *a*-Se for portal imaging are explored. Measurements of the charge signal produced by *a*-Se irradiated by x-rays showed that the x-ray sensitivity (charge produced per energy absorbed) increased somewhat with energy. This was interpreted as a linear energy transfer (LET) dependence. Two recombination models (geminate and columnar) were compared with the data but neither mechanism alone could explain the results. It was concluded that both mechanisms were occurring at high LET but only geminate was present at low LET. This was shown to be consistent with an existing microdosimetric model. Next, a Monte Carlo code that simulates photon-electron transport was used to model the signal-to-noise ratio (SNR) of a metal plate + *a*-Se layer. The model was verified by measuring the SNR of the *a*-Se target of a vidicon directly irradiated by ^{60}Co γ-rays. The model *a*-Se detector was found to be capable of producing images with better SNR than a fluoroscopic system or a metal plate + phosphor primary detector. Finally, the image quality of the latent image on *a*-Se is demonstrated by using a photoinduced discharge readout of an *a*-Se layer.

Table of Contents

Acknowledgements

I would like to express my gratitude to:

- John Rowlands for permitting me to work with him and his group, for guidance in the work in this thesis and for providing a model for scholarship and gentlemanly conduct and his wife Cheryl for her all to often thankless proof reading of papers.

- Alan Rawlinson for his interest in and support of this work.

- Don Plewes and Brian McParland, for the guidance they provided as the other members of my committee.

I have had the privilege to work in three distinct and excellent facilities and would like to thank the staff and students of each one. In particular,

- *Reichmann Research Building* Members of John's group (past and present): Randy, Giovanni, Wei, Dave, Pia, James, Esther, Ira, Neil, Dylan and Winston and honorary members Norm and Andrew for providing friendship, enthusiasm and ideas .

- *Princess Margaret Hospital* Past and present members of the department of Clinical Physics including, but not exclusive to: Stuart, Martin, Steve, James, John, Phil, Cindy, Mohammad, Chris, Sam, Janice, and Duncan for helpful discussions, encouragement, and friendship.

- *Toronto Sunnybrook Regional Cancer Centre:* Members of the department of Medical Physics including Milton, Peter, Bruce, Rose, Ann, and Ian for interest in my work and for lending me access to their treatment units.

- My family for their continued support, love and encouragement.

- Friends in Toronto outside of these institutions who helped cheer me up when things were rotten: Vincent, Faith, François, Marie Josée, Marina, Susan, Shannon, and Sandy.

List of symbols and abbreviations

a	constant that accounts for energy losses (eg. phonon production)
A	atomic mass
A_q	quantum efficiency
A_s	Swank factor
b	empirical constant for field dependence of $W_\pm$
B	bandwidth
C	contrast
CTV	clinical treatment volume
C_{Se}	capacitance of *a*-Se per area
d_{glass}	mass thickness of glass
d_{max}	depth of maximum dose
d_{plate}	thickness of buildup plate
d_{Se}	thickness of *a*-Se layer
$(d\Phi/dE_e)_p$	electron number fluence spectrum generated by x-ray spectrum P
$\dot{D}_A$	dose rate
D	diffusion constant
D_L	diameter of lens
D_M	diameter of field of view on monitor
D_o	diameter of active area of camera target
DQE(f)	detective quantum efficiency
$DQE_C(f)$	DQE calculated from PHS_c
$DQE_E(f)$	DQE calculated from PHS_E
$DQE_M(f)$	measured DQE obtained from irradiation of saticon and measured $NPS_q(f)$ and $MTF_s(f)$
$DQE_p(f)$	theoretical DQE calculated from pulse height spectrum using Monte Carlo measured $MTF_g(f)$ and corrected for non-linear gain
e	fundamental charge
E	energy
E_{abs}	energy absorbed in *a*-Se per area per exposure
E_e	electron energy
E_i	energy of the *i*th bin of pulse height spectrum
f	spatial frequency
f_c	spatial frequency at camera plane
f_r	fraction of charges lost to recombination
f_s	spatial frequency at screen plane
F	electric field
F_c	critical field in columnar theory
FPE	field placement error
GTV	gross tumour volume
H	conversion factor from time to space on face of vidicon
I_s	signal current
ITO	indium tin oxide
k	Boltzmann constant
K	number of frames blanked
L	focal length of lens

LET	linear energy transfer
<LET>	average LET
LSF	line spread function
M	demagnfication
M_j	jth moment of distribution function
MTF	modulation transfer function
MTF_b	MTF of buildup material
MTF'_c	point scanned MTF of camera and lenses
MTF'_{filter}	point scanned MTF of anti-aliasing filter
MTF_g	modulation transfer function of glass measured using film
MTF'_p	product of MTF'_c and MTF'_s
MTF_d	modulation transfer function of saticon directly irradiated by ^{60}Co
MTF_s	modulation transfer function of screen
MTF'_s	point scanned MTF of screen
n	index of refraction
N_B	number of incident x-rays under bone
N_i	number of pulses in the ith bin of the pulse height spectrum
N_T	number of incident x-rays (under tissue)
NPS	noise power spectrum
NPS_0	noise power spectrum normalized to 1 at f=0
NPS_e	electron shot noise power spectrum
NPS_L	noise power spectrum from light illumination
NPS_p	quantum noise power spectrum shaped by MTF'^2_p
NPS_q	x-ray quantum noise power spectrum
NPS_v	video camera noise power spectrum
NPS_x	noise power spectrum from x-ray irradiation
NTCP	normal tissue complication probability
P	photon spectrum
PHS	pulse height spectrum
PHS(E)	pulse height spectrum scored as a function of energy absorbed
PHS(Q)	pulse height spectrum scored as a function of charge generated
PSF	point spread function
PTV	planned treatment volume
q	number of times a procedure was repeated
r	radius of column in columnar recombination = radius of spur
r_0	separation of electron and hole in Onsager theory
R_e	CSDA range of electron
R_{SI}	slope to ordinate intercept ratio
S	collisional stopping power of electrons
S	Schubweg (carrier range)
S_c	carrier signal
S_d	differential signal
SNR	signal to noise ratio
SNR_d	differential signal to noise ratio
SNR_c	carrier signal to noise ratio
t_b	thickness of bone

T	absolute temperature
TCP	tumour control probability
U	separation of spurs
V	volume of spur
V_i	*i*th measurement of surface potential
V_{Se}	surface potential of *a*-Se
w_f	width of rectangular function in frequency domain
W_0	energy required to produce electron hole pair assuming Klein's formula ($W_0 \approx$ 7 eV in *a*-Se)
$W_{\pm}$	measured energy required to produce an electron hole pair
W_p	energy required for an optical photon to be emitted from a screen
W'	relative value of $W_{\pm}$ at 10 V/μm to 50 eV
W_{air}	energy required to produce a unit charge in air
X	exposure
Z	atomic number
α	recombination coefficient
δ	energy of spur
ΔE_{LET}	difference in energy between a low LET electron and a high LET electron
Δt	irradiation time
ΔT	sampling period of digital oscilloscope
$\Delta\mu$	difference between attenuation coefficients
ΔV	small change in surface potential
ΔV_{Se}	change in surface potential of *a*-Se layer
ΔX	small exposure
$\Delta\sigma_{Se}$	change in surface charge density of *a*-Se layer
ε_g	band gap
ε_0	permittivity of free space
ε_{Se}	relative permittivity of Se
γ	slope of H-D curve in the linear region
η	photogeneration efficiency
μ_e	mobility of electron
μ_h	mobility of hole
μ_{glass}	attenuation coefficient for glass
μ_{Se}	attenuation coefficient for a-Se
θ	ratio of amplifier noise to x-ray noise
ρ	charge density
$\dot{\rho}_c$	charge density per volume per time
ρ_0	initial charge density
ρ_M	mass density
σ	noise (standard deviation of signal)
σ_{Al}	surface charge density of Al substrate
σ_{probe}	surface charge density of probe
σ_{Se}	surface charge density of *a*-Se layer
τ	bulk transmissivity of lens
τ_h	hole lifetime
τ_e	electron lifetime
ξ	light collection efficiency of lens
ω	fitting parameter for electron range

Chapter 1

Introduction

"X-rays. Their moral is thus - that a right way of looking at things will see through almost anything."
- Samuel Butler 1835-1902

I. INTRODUCTION

Cancer is the second leading killer of Canadians[1] accounting for 55 000 deaths annually, a number which is expected to increase as the population ages over the next few decades. Although a variety of alternative therapies are actively being explored,[2,3,4,5] most cancers today are treated with some combination of surgery, chemotherapy and radiation. Approximately half of all cancer patients are treated with radiation at some point in the course of their overall care.[6] The radiation may be administered using sealed sources in a catheter which is surgically inserted into the patient's body (brachytherapy), or most commonly using directed external beams of x-rays or electrons. As shown in Fig. 1, radiation treatment units for external beam therapy typically consist of a radiation source which is mounted on a gantry capable of moving in a 360° arc around the patient who lies on a treatment couch. The treatment volume is placed at the centre of rotation (called the isocentre) so that multiple beams from different directions will intersect at that point, maximizing the dose delivered to the tumour while minimizing the dose to healthy tissue surrounding it. As more radiation is delivered, the tumour control probability (TCP) increases, but because the radiation must usually pass through healthy tissue to reach the tumour, the normal tissue complication probability (NTCP) increases as well; thus, in most cases, the amount of radiation delivered, and hence the TCP is limited by an acceptable NTCP.

The process of radiation therapy consists of diagnosis, treatment planning and treatment delivery. Patients diagnosed with cancer may be referred to a radiation oncologist, who, through palpation, biopsies, and imaging procedures (e.g. magnetic resonance imaging, MRI), determines the nature, location, and extent of the gross tumour volume (GTV).[7] The radiation oncologist adds two margins

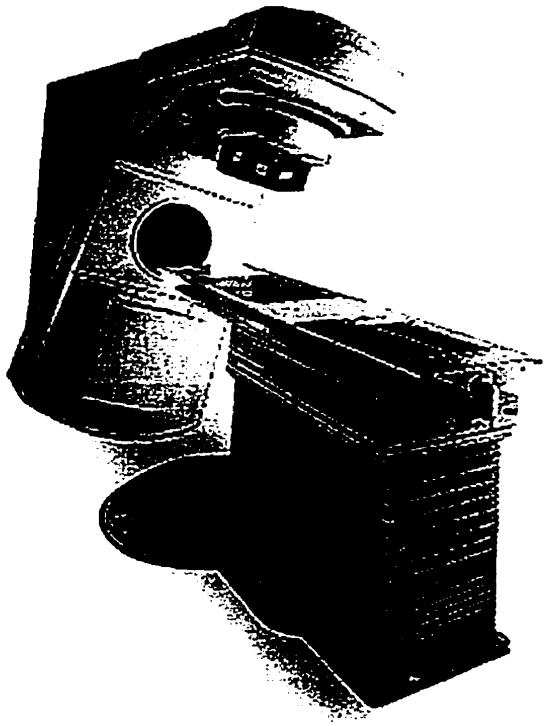

Fig. 1 Photograph of an isocentrically mounted linear accelerator. The accelerator and couch are capable of moving independently around the same point in space.

to the GTV. The GTV plus the margin added for microscopic disease forms the clinical treatment volume (CTV).[7] In addition, a margin is added for field placement errors (FPEs; see section III.A) of the daily treatments. The combination of the margin for FPEs and CTV form a fixed geometric volume in which the CTV is constrained to remain throughout the treatment. This volume is known as the planned treatment volume (PTV).[7]

To aid in treatment planning, the patient is then imaged on either a simulator, a computed tomography (CT) scanner, or both. A simulator is a diagnostic x-ray unit designed to mimic the movements, alignment properties and geometry of an isocentric treatment unit. It is used to take radiographs under the geometry in which the treatment is to occur. The CT scanner is a device capable of producing x-ray images of slices of the patient. In either case, the images are used by the radiation oncologist to outline and prescribe the radiation dose to the PTV. The physician also indicates the location of particularly radiosensitive structures (e.g. spinal cord) and the maximum dose permitted to them. The radiation prescription includes the size of the daily treatment dose or fraction (e.g. 200 cGy/day over 6 weeks).

At the simulator, measurements of the patient contour are also made to aid in the design of beam shaping devices (e.g. attenuators, missing tissue compensators). Marks are made on the patient's skin which will be used to realign the patient on the treatment unit using the identically positioned field light and orthogonal wall lasers at the treatment unit. Other methods to help ensure proper patient positioning include casts moulded to the shape of the patient, pillows, bite blocks, nose bridges, and head rests.[8] The treatment is then planned by a dosimetrist or a physicist who calculates the radiation dose distribution within the patient. The number, energy and orientation of the beams is selected to

obtain a dose distribution that meets the prescription. Finally, the patient is set up on the treatment unit and irradiated.

One limit of curative* radiation therapy is that the tumour must be localized to a region, i.e. radiation therapy cannot cure where there is large spread of the cancer (metastasis). It has been estimated[9] that 72% of cancer patients, when diagnosed, have localized disease, and thus are potential candidates for curative radiation therapy. However, the overall three year survival rate of cancer patients is only ~50%,[9] implying that current treatments including radiation therapy do not cure all localized tumours. Failure of radiation therapy to cure may result from either: (i) metastatic cancer which was undetected and therefore untreated, or (ii) the inability of radiation to cure the original tumour (i.e. produce local control) due to either improper (e.g. geometric misses) or inadequate delivery of radiation, which may lead to recurrence at the original site or metastatic disease from the original site. If the former is the case, then increasing the amount of radiation delivered to the target volume (dose escalation) will not improve local control and increase survival. However, there is compelling evidence to indicate that the latter situation may be relevant hence, dose escalation could improve survival. In fact, metastatic disease appears to occur as a result of failure to locally control the tumour. For instance, Liebel *et al.*[10] found that for head and neck tumours, local failure correlated with a 4-15 fold increase in likelihood of metastatic disease. Studies of other sites including breast,[11] lung,[12] rectum,[13] prostate,[14] soft tissue carcinomas,[15] head and neck tumours,[16] and uterine cancer[17] also suggest that the incidence of metastasis correlated with local failure. Since this can often lead to death, these studies suggest that increasing local control could potentially increase patient survival. One approach to delivering a higher curative dose while retaining protection of surrounding normal tissues is known as conformal therapy[18] and is described in the next section.

---

* Radiation therapy is often used for palliation as well.

II. CONFORMAL THERAPY

A. Description

Williams *et al.*[19] found by studying a variety of clinical sites, that the amount of additional radiation required for an increase in the tumour control probability (TCP) from 40% to 60% may be little as 3% (and as much as 35%). Thus, the success rate of curative radiation therapy can be increased if more radiation could be delivered to the tumour while sparing healthy tissue. One approach is to reduce the amount of healthy tissue irradiated by reducing the margin. In particular, if the planned target volume could approach or equal the clinical target volume by reducing the field placement errors (FPE; see section III.A), the tumour control probability could be increased without increasing the normal tissue complication probability.[20]

To exploit this possibility, conformal therapy,[21,22,23] is being developed. Conformal therapy was first introduced by Takahashi[24] in 1965. Fig. 2 illustrates the general concept behind conformal therapy as it first appeared. Imagine an arbitrarily shaped tumour in the patient, surrounded by healthy tissue. Using conventional therapy, the tumour is irradiated by two rectangularly shaped fields. Because the shape of the tumour does not match that of the treatment volume, the healthy tissue in the box shaped treatment volume is irradiated to the same treatment dose as the tumour volume. Conversely, in conformal therapy, the dose distribution formed by many more shaped beams rotating in an arc about the tumour match its shape, thus minimizing the dose to healthy tissue. The evolution of conformal therapy from conventional radiation therapy requires improved immobilization, understanding of and ability to monitor and account for organ motion[25,26,27] (both inter- and intra-fractional), better

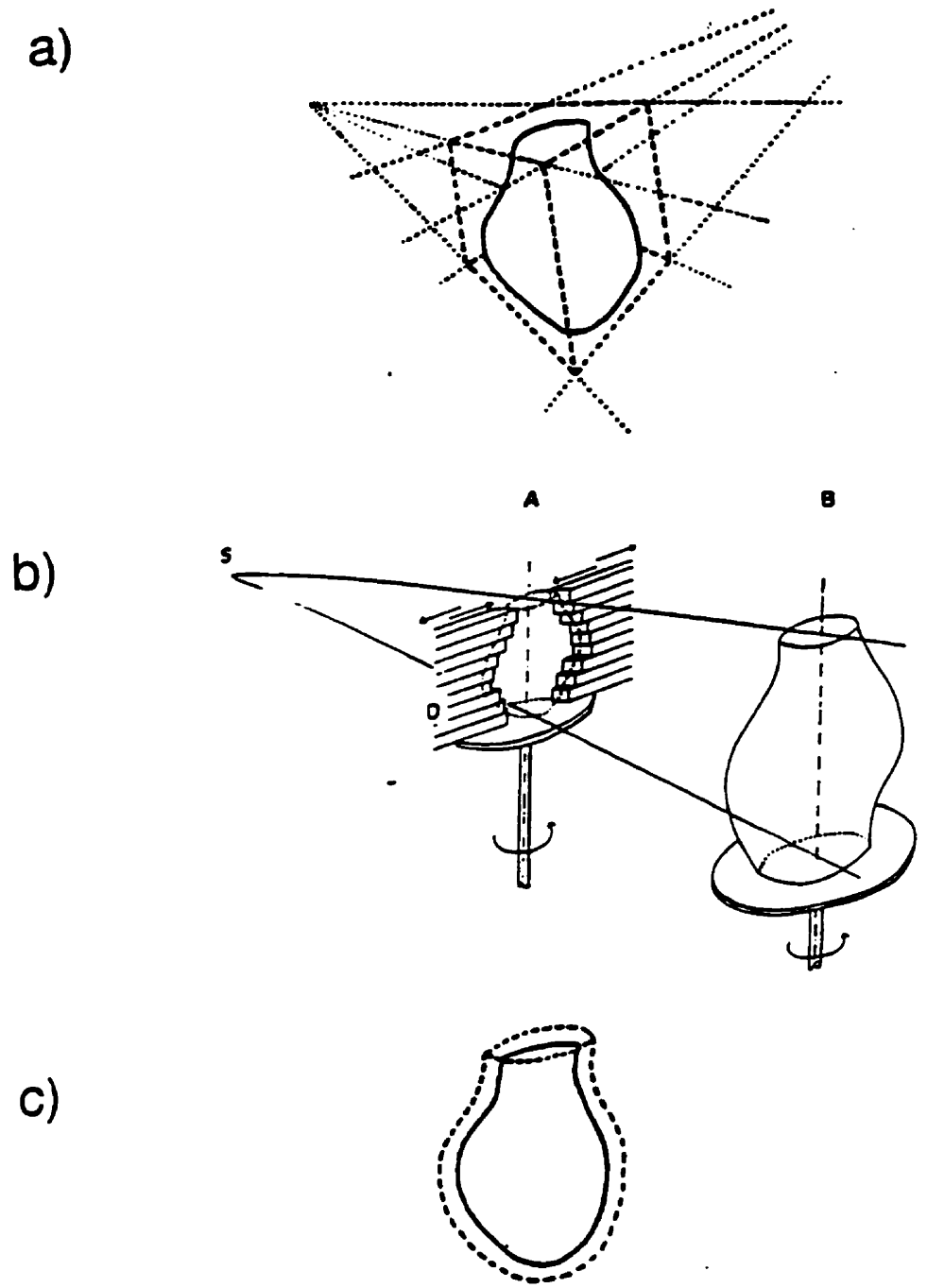

Fig. 2 Illustration of conformal therapy. This figure was taken from the early work of Takahashi[24] who was among the first to suggest the concept. (a) Conventional radiotherapy, in which a tumour and surrounding healthy tissue is irradiated to the prescribed (high) dose. (b) By introducing a multileaf collimator to shape the treatment field and rotating the beam about the patient (or by rotating the patient with respect to a stationary beam), the high dose region can be shaped to more closely match that of the tumour as shown in (c).

knowledge about radiobiological effects[28] (e.g. partial volume, fractionation), and improvements in the technology used to deliver the radiation. Clinical trials on conformal therapy are just beginning[29,30,31,32] and have in part resulted from the introduction of a variety of new technologies. Improvements in medical imaging[33] have led to better knowledge about the location and extent of the tumour. In addition, these technologies[34] (e.g. x-ray computerized tomography), give digital volumetric information which may be used by three dimensional treatment planning systems[35] that are also being developed. The growth of computer controlled accelerators with multileaf collimators[36,37] have made it practical to routinely shape multiple treatment fields to match that of the malignant tissue. Together, these technologies should permit margins to be reduced as treatment plans become more sophisticated and aggressive to increase the tumour control probability.

B. Potential Impact

What sites would benefit from conformal therapy and how will this affect long term survival ? There is insufficient data to completely answer this question. However, several sites have been suggested for clinical research in conformal therapy based upon two criteria: (i) high local failure with current radiotherapy doses and (ii) significant incidence of complications at current dose levels. These are summarized in Table I. Ling *et al.*[38] calculated, using a mathematical model of metastatic spread, the potential impact of conformal therapy on prostatic cancer survival. Their results, shown in Fig. 3, indicate that conformal therapy could enhance cure in prostatic cancer and is likely applicable to other sites in which metastases occur as a relatively late event. Early results from clinical trials using conformal therapy for prostate cancer have shown promise.[29,30]

Site	High Local Failure (type/stage)	Complication	Clinical Trials
Brain	Glioblastoma Multiforme	-	
Head and Neck	T_1, T_3, N_3	Xerostomia	yes
Lung-NSCLC	T_1, T_4, N+	Lung, heart	yes
Esophagus	Yes	Lung, heart	?
Pancreas	Yes	Small Bowel	?
Rectum	B_1, C	Small Bowel	?
Prostate	T_1, T_4	Rectum	yes
Skull Base	Different histopathologies	Brainstem, spinal cord	?
Sarcomas	-	Yes, in some, e.g. lymphedema	?

Table I List of possible sites for clinical trials in conformal therapy. The table was taken from reference 32. In the column for clinical trials, a "yes" indicates feasibility and/or an ongoing clinical study while a "?" indicates doubt of whether a sufficient number of patients can be recruited in any single institution for such studies.

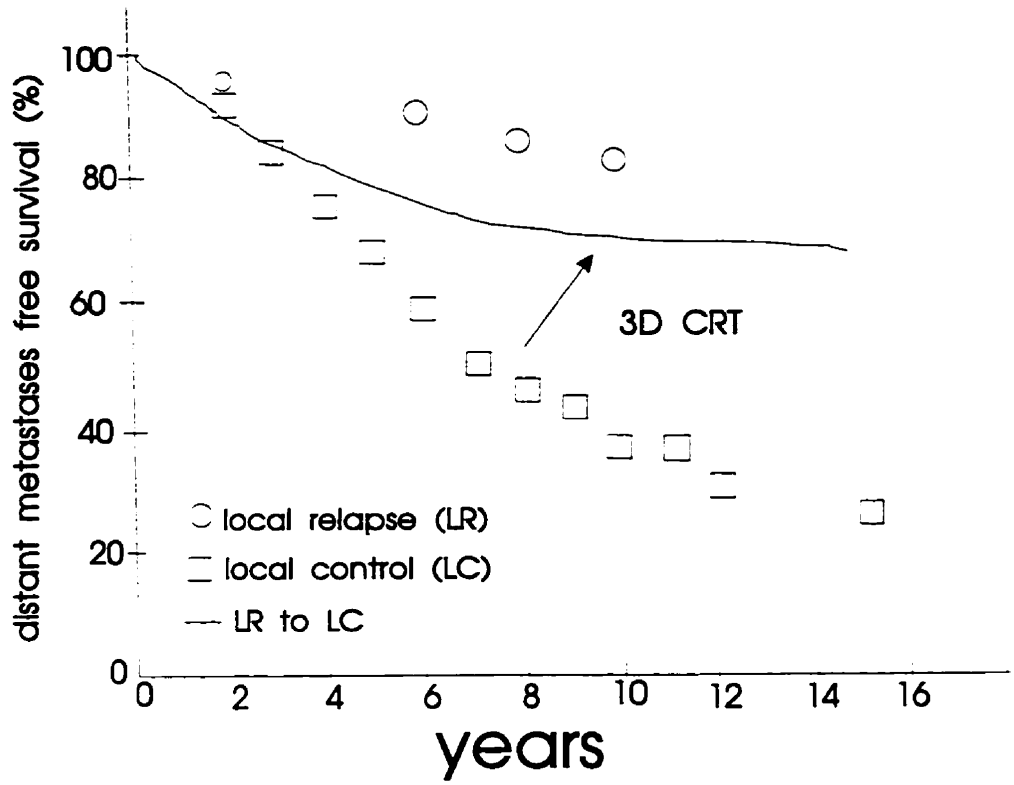

Fig. 3 Calculation of potential benefit of conformal therapy on prostatic cancer using a biomathematical model adapted from reference 38. The circles and squares are clinical distant metastases free survival (DMFS) for paitients with local control (LC) and local relapse (LR) respectively. The solid cuve represents the calculated DMFS if all LR were converted to LC.

Attempts have been made to estimate the impact of 100% local control. A review of some of these data for three pelvic sites are provided by Suit.[39] Data collected from several large institutions indicated that salvage surgery** for radiotherapy failures results in 15-40% additional long term (5 year) survival rates. Considering the incidence of cervical, colorectal, and ovarian cancers, Suit calculated that if there were complete (100%) local control, there would be an additional 21 000 survivors/ year in the United States. For oral cavity and oropharynx cancers, there could be an additional 2000 survivors/year. Overall, for cancer of the head and neck region, ~1/3 of patients fail locally implying that there could be potentially an increase of up to 10 000 survivors/year of such patients. The values are by no means comprehensive since they only consider four types of cancer. DeVita[40] estimated that 380 000 patients annually were treated with radiation therapy in the U.S.A. Of these, 180 000 were treated with intent to cure, however, he estimated that only 90 000 of these were in fact curable. However, of the other 90 000 who were *not* curable, 60 000 were expected to relapse at the original site. If local control could be improved, some fraction of these 60 000 patients may survive. If one were to divide these numbers by a factor of 10, this should be approximately the number of curable patients in Canada if 100% local control were achieved through techniques such as conformal therapy.

** Salvage treatments result in prolonged disease free survival and are considered proof that treatment of a tumour locally could have resulted in cure. If the original treatment had been successful, secondary (salvage) treatments would not be necessary.

III. PORTAL IMAGING

A. Field Placement Errors

For conformal therapy to be successful, with its tighter margins, it is important that the patient be positioned (set up) very accurately relative to the beam. This implies that field placement errors (FPE) must be detected, monitored, and minimized. FPEs may occur as a result of internal and external changes in the patient due to weight loss and movement of internal organs relative to the skin markings used to align the patient. They may also be caused by set up errors such as the improper use of beam modifying devices (e.g. wedges, compensators) or errors in patient positioning. FPEs are of particular concern since they are the largest source of uncertainty in dose delivery[41] compared to other uncertainties such as variations in treatment unit output, gantry and couch stability and dosimetry.

Both clinical and theoretical studies indicate that the consequences of FPEs can be serious. Kinzie *et al.*[42] found that inadequate patient positioning (e.g. if a prescribed node were not included in the field or if tumour is partially shielded) resulted in an increase in relapse rate of Hodgkin's disease from 14% to 54% and an increase in the infield or marginal recurrence rate from 7% to 33%. White *et al.*[43] found that for oat cell carcinoma of the lung, those with major protocol violations, 80% of which were due to in part or completely to shielding errors, had statistically worse survival. Boyer and Schultheiss,[44] employing a radiobiological model, found that increasing the precision of dose delivery by 1% would increase the cure rate by 2%. Daftari *et al.*[45] found using dose volume histograms and a radiobiological model that patient positioning must be kept to within 2 mm to ensure a normal tissue complication probability (NTCP) of 1%. McParland[46] calculated the tumour control probability (TCP)

as a function of field placement error, the size of the penumbra,[***] and the margin used for a fixed NTCP. For smaller penumbra (~3 mm) and margins of 0.5-1 cm, field placement errors greater than 2 mm resulted in a significant loss of tumour control probability for a given normal tissue complication probability (e.g. increasing the FPE to 5 mm resulted in a TCP of 0.6 compared to 0.75 for an FPE 2 mm). Similarly, Brahme *et al.*[47] found using a radiobiological model that the tumour control probability would decrease by between 3-7% (depending upon the slope of the dose response curve) for a 2 mm shift. Thus, these theoretical considerations suggest that the beam should be localized with respect to patient anatomy to within 2 mm.

B. Current Portal Imaging Practice

To monitor patient setup and as a final check that the patient has been set up properly, a film may be placed behind the patient and exposed using the treatment beam. The location of the bony landmarks on the resulting radiographs relative to the beam edges may be compared to those prescribed on the simulator radiographs to verify that the beam has passed through the patient in the desired orientation. This film also serves to provide a legal record of the treatment and is of particular importance because the skin marks may shift with respect to internal patient anatomy,[48] or be removed over the 4 to 8 week treatment time. To properly monitor and prevent FPEs, films should be taken frequently.

Because the radiation beam used to produce the image exits through the treatment port of the accelerator, these films are often referred to as *portal* images. Portal films exposed with the entire

---

[***] Penumbra refers to the spread of the edges of the radiation field within tissue. In a ^{60}Co beam, it is dominated by source size effects whereas in linear accelerator beams it is dominated by electron transport. Typical values of penumbra are 8 mm for ^{60}Co and 2-4 mm for linac beams, based upon the 80-20% penumbra for at a 10 cm depth for a 10 cm x 10 cm field.

daily treatment fraction are known as *verification* images whereas those exposed with a portion of the daily treatment fraction are known as *localization* images.

Unlike diagnostic radiology, where x-rays are detected in a phosphor screen and converted into light which is used to expose the film, in portal imaging, the film is exposed in a metal plate cassette. The plate serves to:[52] (i) increase the quantum efficiency above that of film alone because it provides electron equilibrium in the film, thus maximizing the signal from the x-ray beam, (ii) remove some lower energy scattered x-rays and all scattered electrons from the patient (which carry no image information but add noise and reduce contrast) and (iii) if it is high density, it minimizes the spread of electrons within it, producing good resolution. Because film is still the most common detector for portal imaging, many investigators have attempted to optimize the image quality by using different thicknesses and types of front and rear plates.[49,50,51]

Despite these efforts, film still has two limitations: (i) poor image quality and (ii) inconvenience. Fig. 4(a) shows a simulator radiograph and Fig. 4(b) shows the portal film of the same patient. As explained in section C.2, noise and poor display limit the quality of portal films. The inconvenience of films arises from the time and effort necessary to position them, an interruption in the treatment fraction for retrieval (of localization images) from the treatment room, and the additional time required to transport them to an often remote dark room for development. Thus portal films are usually viewed the day after they were exposed, precluding interactive positioning. As a result of these limitations, portal films are taken only once a week (per patient) in American institutions and even less frequently in Canadian ones.[52,53]

a)

b)

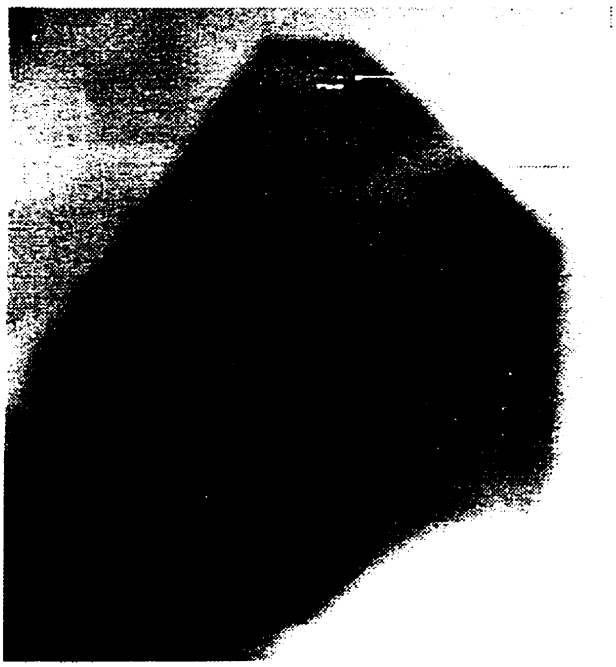

Fig. 4 a) Typical diagnostic radiograph from a simulator. (b) Typical portal radiograph (film) from linear accelerator. The film was exposed in a Kodak therapy verification cassette using Kodak Ortho G film. It is a double exposure radiograph in which the collimator jaws of the treatment unit are opened wide and the film is exposed. The jaws are then reset and an additional exposure is given. The resulting image has the treatment field superimposed on a larger background to determine where the treatment field is relative to the patient. The use of double exposure radiographs is a consequence of the poor image quality of the portal film and requires that healthy tissue outside the treatment field be irradiated.

For conformal therapy to become a practical reality requires better portal image quality and more convenient image acquisition than film can provide. To address this need, a variety of electronic portal imaging devices have been developed which detect the x-ray beam after it has passed through the patient and display a portal image on a video monitor located outside the treatment room within seconds. This permits routine monitoring of the patient and in principle, correction of the patient-beam positioning without having to enter the treatment room.[48] A variety of detectors have been proposed and developed,[54] two of which have become commercial systems, a liquid ionization chamber array and a fluoroscopic system. The former, illustrated in Fig. 5(a) consists of two perpendicular sets of copper strips with an insulating liquid between them. The strips form 256x256 liquid filled ionization chambers and the detector spans an area of 32.5 cm x 32.5 cm. The high energy electrons resulting from incoherent x-ray scattering in the stainless steel buildup material above the copper strips or in the liquid itself produce ions which are collected by applying a high voltage across one of the electrodes. The detector is read off by switching the high voltage on one row and collecting the charges along each column. Then the next row is switched on and the detector is read off in a scanning fashion. Since the entire detector is being irradiated but only one row is actively collecting charge, only a small fraction (1/256) of the incident x-ray fluence is being completely collected. Charge trapping in the liquid increases the total fraction of collected charge signal, and the overall efficiency of the system is dependent upon the electrode distance, applied potential, and some of the liquid characteristics.[55] Currently, due to the added noise in the readout, the best images are obtained when the detector is scanned slowly, resulting in a larger signal per pixel. Consequently, a relatively high dose (~50 cGy) is required to produce an image. Moreover, the relatively large pixels limit the resolution of the system. One advantage of the system is that it is slim in profile making it relatively unobstructive when used clinically. The other commercially available device, the fluoroscopic portal imager, is shown schematically in Fig. 5(b). The use of a metal plate bonded to a phosphor to convert

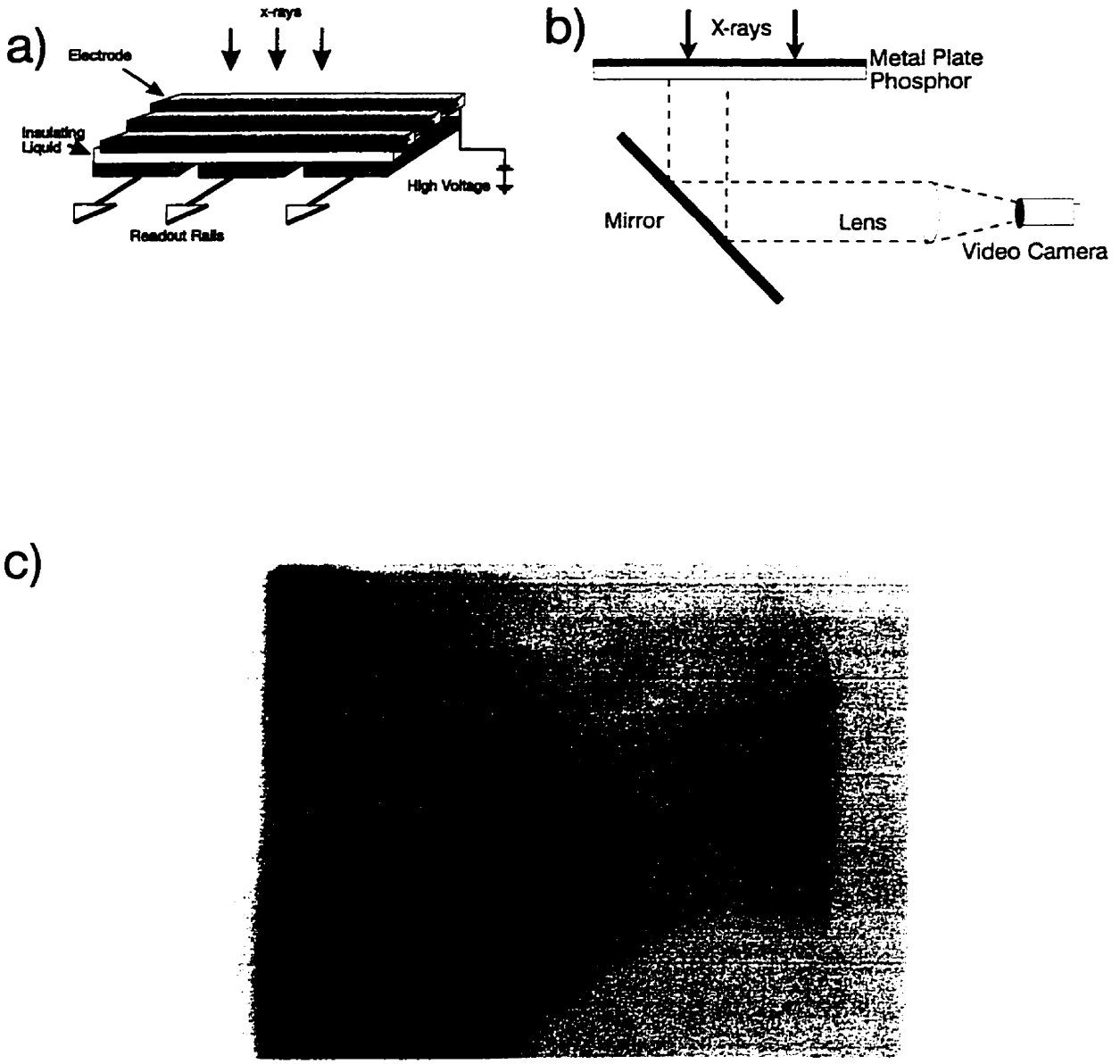

Fig. 5 a) Schematic of liquid ion chamber array. Not shown is a stainless steel plate which is above the high voltage rails and acts as the buildup material.
b) Schematic of fluoroscopic portal imaging system.
c) Typical portal image from a fluoroscopic system. This is a double exposure radiograph of the same patient as in Figs. 2(a) and (b).

the x-rays into light and a video camera to view the image was introduced in the modern era by Baily *et al.*[56] Unfortunately, as will be described in more detail in Chapter 2, to view the large fields (40 cm square) used in radiation therapy, the camera must be placed far away from the phosphor screen. Consequently, it collects only a small fraction of the light generated at the screen thereby degrading the image quality. Thus, although these devices have made it more convenient to take a portal image, image quality, as illustrated in Fig. 5(c), remains poor and in some cases clinically inadequate.[48,57,58] Moreover, the design of the fluoroscopic system makes it bulky, thus increasing the likelihood of collisions between the patient, gantry and portal imager and limiting its use in some dynamic treatments. In addition, the bulkiness precludes the installation of the imager on units with a beam stop.

C. Image Quality in Portal Imaging

Portal images are inferior to diagnostic radiographs for a variety of reasons, some specific to the problem of portal imaging and others dependent upon the individual detectors.

1. Fundamental issues for portal image quality

There are three reasons that portal images could be poorer than diagnostic images: (a) reduced contrast, (b) additional noise and (c) reduced resolution. The first two are related to each other by the signal-to-noise ratio (SNR). As shown in Fig. 6(a), there are two types of signal. The first is called the carrier signal and refers to the size of the signal above the dark level and the second is called the differential signal which considers the difference in transmission beneath an object with respect to its

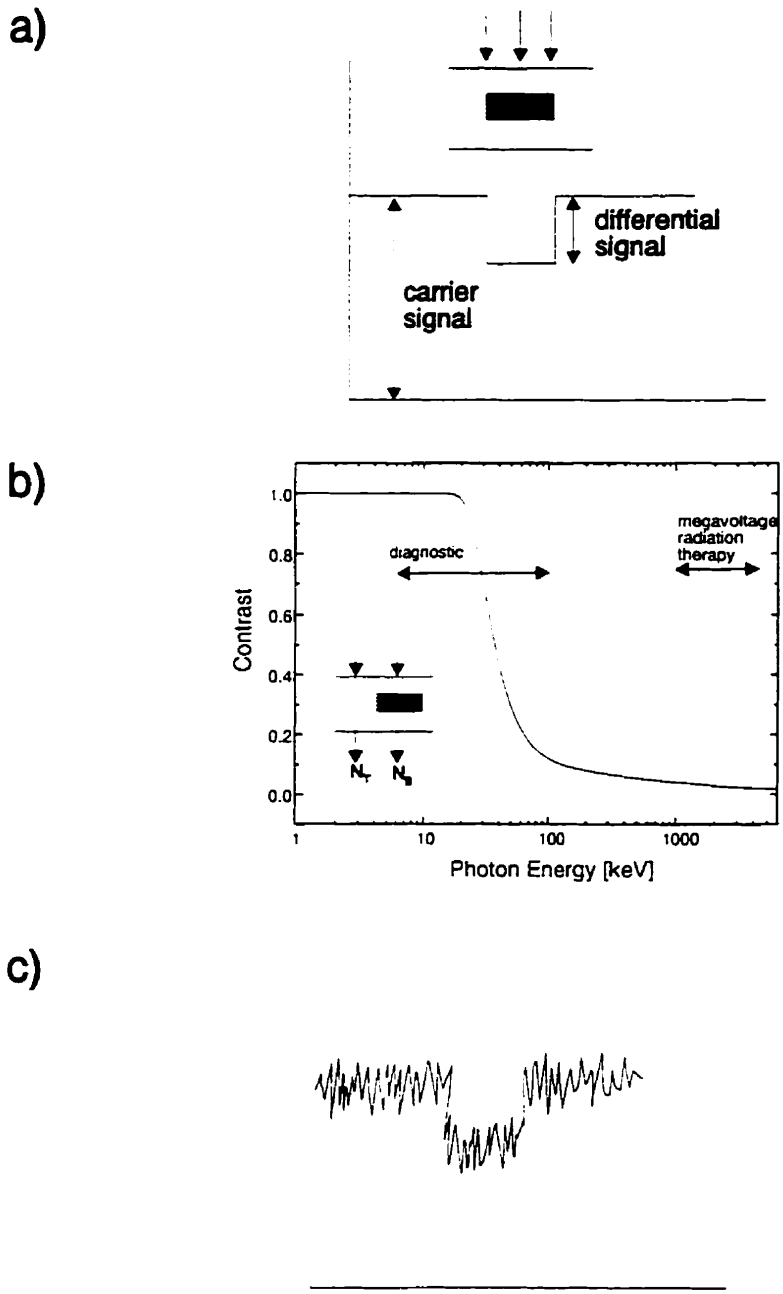

Fig. 6 (a) Illustration of carrier signal and differential signal. (b) Contrast of 1 cm of bone in tissue as a function of x-ray energy. The choice of bone thickness is arbitrary. (c) Illustration of effect of added noise to the signal shown in (a).

background. If N_T monoenergetic x-rays pass through tissue, and are incident on a detector which counts photons, the carrier signal is given by

$$S_c = A_q N_T , \qquad [1]$$

where A_q is the quantum efficiency or the fraction of incident x-rays that are detected. Assuming the object is bone, then the differential signal is given by

$$S_d = A_q C N_T , \qquad [2]$$

where the contrast, C, which is typically small in portal imaging and describes the difference between the signal beneath the bone and its background, is given by

$$C = \frac{N_T - N_B}{N_T} = 1 - e^{-\Delta\mu t_b} . \qquad [3]$$

N_B is the number of x-rays incident on the detector in the shadow bone, $\Delta\mu$ is the difference between the linear attenuation coefficients of bone and tissue (water),[59] and t_b is the thickness of bone. Fig. 6(b) shows that for 1 cm of bone in tissue, the contrast decreases rapidly as the x-ray energy increases from the diagnostic to radiation therapy range. Hence one reason that portal images are poor is due to low contrast resulting from the use of high energy beams which are required to provide the prescribed dose distribution. Fig. 6(c) shows that if noise is present, detection of the bone will depend upon the differential signal-to-noise ratio,

$$SNR_d = \frac{S_d}{\sigma} , \qquad [4]$$

where σ refers to the standard deviation of the signal. To identify an object, Rose[60] indicated that the SNR_d measured over the total area of the object must be greater than approximately five. All x-ray images contain noise, some from the readout and recording of the image, and another part resulting from the use of a limited number of x-rays. This latter form of noise is known as x-ray quantum noise

and results from the counting statistics associated with x-ray detection. The best SNR that can be obtained from an x-ray imaging detector occurs when all other sources of noise have been reduced to the point where the x-ray noise is the dominant source of noise. If this is achieved, the image quality can only be improved by increasing the number of x-rays used or by increasing the quantum efficiency of the detector. In such a situation, the system is said to be *quantum noise limited*. The ratio of the carrier signal to the noise, $SNR_c=S_c/\sigma$, of a quantum noise limited detector is equal to $(A_qN_T)^{1/2}$ since $\sigma=(A_qN_T)^{1/2}$ for Poisson distributed x-ray noise.

Based upon the definitions above, Boyer *et al.*[54] calculated the zero spatial frequency (large area) quantum noise limited SNR_d for 1 cm of bone in tissue for a typical diagnostic radiograph and a typical portal film. Remarkably, they found them comparable because although both the contrast and quantum efficiency are lower for portal imaging, the carrier signal-to-noise ratio, SNR_c, is higher since many more x-rays are used clinically in therapy.

Resolution will also affect the image quality. The eye is particularly sensitive to edges,[61] hence blurring will reduce the observer's ability to detect landmarks. Furthermore, blurring will increase the uncertainty of the location of an edge, and hence the ability to localize the beam within the ±1 mm required to maximize the tumour control probability (section IIIA). However, since the resolution of a metal plate is superior to that of a diagnostic screen,[51] and since the source size of modern linear accelerators can be made as small as ~0.5 mm, it is possible to make source size blur insignificant (e.g ~7 mm^{-1} at a magnification of 1.2).[62] Patient motion will also reduce image quality, but since most portal images are made within a few seconds and since patient motion is <1 mm over the course of a ~ 1 minute treatment,[63] for many sites, this source of blurring is small.

Thus, although theoretically there is sufficient information detected by a metal plate in a megavoltage beam to produce a diagnostic quality image, existing portal imagers and film still produce poor images. Hence, they are not optimized from an SNR perspective (i.e. not quantum noise limited). Therefore, if a better detector system could be constructed, image SNR_d, and hence image quality could be improved.

2. Portal image quality requirements

For portal imaging to be effective in either conventional or conformal therapy, the images must be of sufficient quality to identify and locate (bony) landmarks relative to field edges. Since conformal therapy will have multiple small fields, often with no or few bony landmarks, the role and requirements of portal imaging in conformal therapy may be greater than those in conventional radiation therapy. There have been a variety of possible approaches suggested. Among them:

a. use a diagnostic x-ray tube to produce the background image.[64] This technique produces good quality images but suffers from the possible errors associated with the fact that the source of the x-ray tube and the treatment unit are not in the same position.

b. use an x-ray beam with both a megavoltage and diagnostic energy component and extract the diagnostic part of the spectrum using a detector that preferentially absorbs low energy photons.[65] Unfortunately, with this approach, image quality becomes worse as the patient thickness increases due to beam hardening and scattered radiation.[66]

c. superpose the treatment field on a background image which includes landmarks (double exposure image; see Fig. 4(b)). Unfortunately this requires that the healthy tissue outside the treatment volume be irradiated. With the increased number of fields in conformal therapy, the detector must use the radiation as efficiently as possible (i.e. the detector sensitivity should be increased).

d. add landmarks to the small field in the form of surgically implanted radio-opaque markers.[27] To reduce the invasiveness of this technique, the markers should be as small as possible, which in turn requires that the detector have high resolution as well as sensitivity.

The latter two results suggest that as many x-rays should be detected as possible. Moreover, since detection of small landmarks or edges requires high resolution, the resolution should be as high as possible. Indeed, the required uncertainty for field placement has been estimated to be submillimeter,[67] requiring better than 1 mm resolution. Thus the resolution of a portal imager should at least meet, and ideally surpass the 2 mm required by radiobiological considerations (see section A).

3. Specific limitations of existing approaches

Noise and poor display contrast limit the quality of portal films. Shown in Fig. 7 is a characteristic curve (also known as a H and D curve[68]) of film, plotted as the optical density as a function of the logarithm of the incident exposure. The slope of the straight line part of the curve (γ) relates the difference in contrast between bone and tissue to the optical density (darkness) of the film. One approach to increase the difference in brightness and darkness between bone and tissue, is to increase γ,[69] but this reduces the latitude and requires improved accuracy in exposing the film. A second approach to improve display contrast is to digitize the film using a video camera[70] or scanning array[71] and store the image in a computer. The digital image can then be processed[72,73] to improve the display contrast thus permitting the viewer to extract the information in the image. The results of such approaches have been mixed. In some cases, if sufficient time is allotted to view the images, observer performance of digitized and non-digitized films is the same,[74] but in other cases,[75] digitization has been shown to improve observer performance slightly. The reason for these different

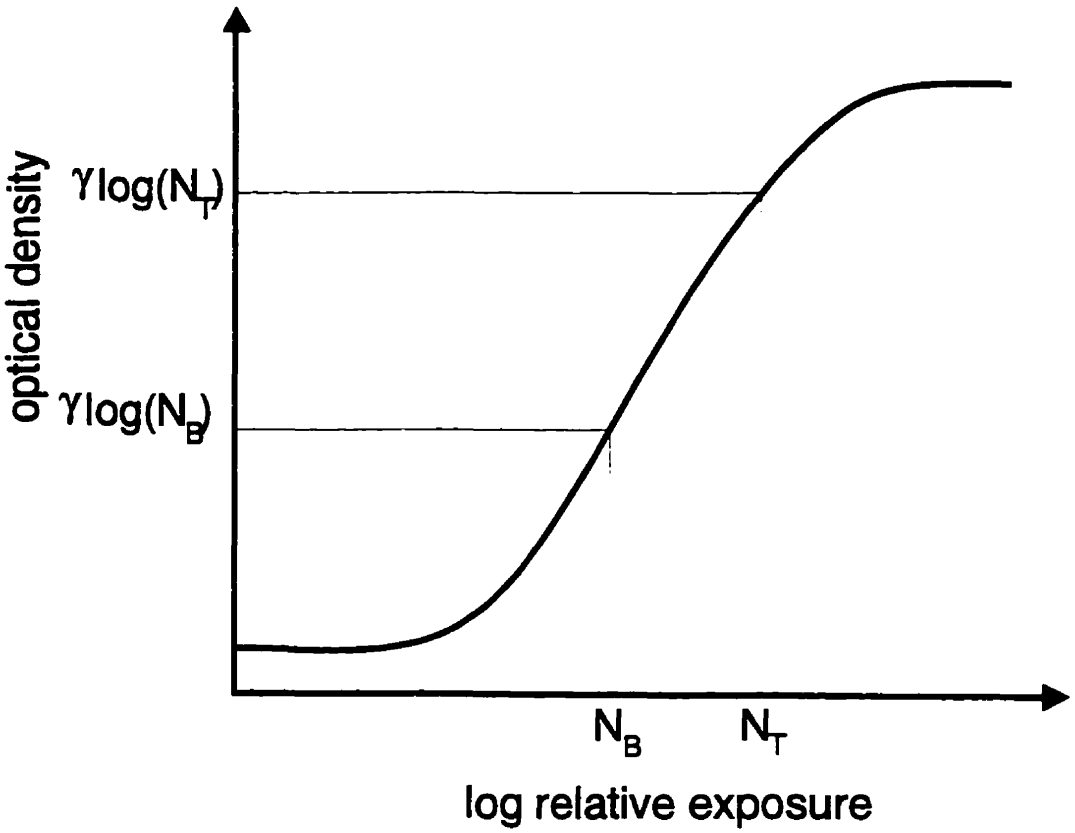

Fig. 7 Characteristic curve of film. The slope of the curve in the straight line region is known as the gamma (γ) of the film. The optical density is defined as $\log(I_o/I)$ where I is the light intensity transmitted by the film and I_0 is the light intensity incident upon the film. If N_B represents the number of x-rays incident on the film under bone and N_T represents the number of x-rays incident on the film under tissue, then the differences in optical density will vary linearly with γ and the differences between $\log(N_B)$ and $\log(N_T)$.

results may be due to different film and processing conditions, and different display and digitization methods. Regardless of the utility of image processing on portal films, digitization of the film cannot produce a quantum noise limited image since film granularity is the dominant source of noise.[51] Thus, film digitization cannot produce an optimal portal image.

The poor image quality produced by fluoroscopic portal imaging systems has been presumed to be limited by the poor optical coupling between the lens and phosphor[76,77] resulting in a loss of information between the primary detection of the x-ray at the phosphor screen and the final displayed image. This explanation is consistent with the observation that fluoroscopic imagers are not quantum noise limited.[75] Experimental measurements[75,78] to date only indicate that the systems are not quantum noise limited, do not indicate how far the system is from the quantum noise limit. Thus in Chapter 2, we sought to determine the potential for improvement in fluoroscopic portal imagers by measuring the x-ray quantum noise in a test fluoroscopic system and comparing it to other sources of noise. We found that these systems fail to be quantum noise limited due to poor optical coupling and the added noise of the video camera. We also found that the resolution of the system is limited by blur in the camera, lens and phosphor. Theoretically, with significant modifications, fluoroscopic systems could be made quantum noise limited over the spatial frequency range 0-0.2 mm^{-1}, but this is insufficient to meet the resolution requirements to maximize the tumour control probability and optimize the image quality (see sections III.A and III.C.2. of this chapter).

To summarize, the liquid ion chamber system suffers from the inability to store the image before it is read off (section III.B) and the fluoroscopic systems suffer from poor optical coupling. Both approaches suffer from poor resolution. A better approach might be to produce a detector that is directly bonded to the buildup plate to avoid the optical coupling problem and with the ability to store

the image until it was read off. Ideally, this detector should also provide high resolution. We hypothesized that using a photoconductor as the image sensor could overcome both weaknesses of the existing systems, thus Chapters 3 and 4 of this thesis explore the possible use of amorphous selenium for portal imaging.

D. Amorphous Selenium

Amorphous selenium (*a*-Se) is a photoconductor, a semiconductor that conducts electricity if illuminated by light or irradiated by x-rays. *A*-Se has been used previously for both diagnostic and portal imaging using the xeroradiographic process[79,80] and is currently being further developed for a variety of reasons:

(i) It has useful photoconductive properties in the amorphous state, and hence can be readily made into large area sensors, i.e. comparable to the size of body parts.

(ii) It has a reasonably high atomic number (Z=34) and hence when made into a layer of the appropriate thickness, has a high quantum efficiency, A_q for detecting diagnostic x-rays.[81] For portal imaging however, its lower atomic number compared to phosphors, may be advantageous because it will not absorb lower energy scattered x-rays, which carry no image information, as strongly.[82]

(iii) Because of its importance in photocopying technology, it has been developed to the point that it has good materials properties including: very low dark current, radiation damage resistivity, very little charge trapping (no lag or ghosting), physical uniformity and few point defects.

(iv) It has very high spatial resolution[83] compared to phosphor screens. As illustrated in Fig. 8, phosphor screens consist of grains imbedded in a supporting medium. X-rays Compton scatter in the metal plate and phosphor and produce electrons which spread laterally degrading resolution (see Chapter 4). However, in a phosphor, they also generate light which scatters within the screen multiple

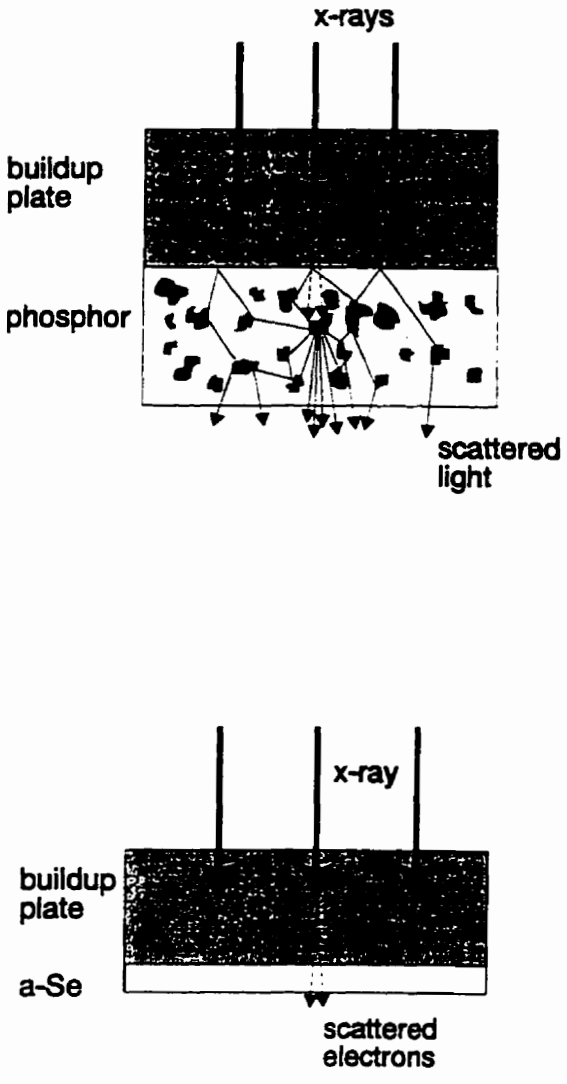

Fig.8 Illustration differences in the spread of a signal in a phosphor and in a-Se.

times before exiting, resulting in additional blurring. In *a*-Se however, only the loss of resolution due to the spread of Compton scattered electrons within the metal plate and *a*-Se occurs.

Image formation in *a*-Se is illustrated in Fig. 9. As the Compton scattered electron travels through the *a*-Se, it deposits energy, liberating electrons and holes. The *a*-Se has been electrically charged (biased) before irradiation, and the resulting electric field draws the electrons and holes vertically to opposite surfaces withour further blur where they neutralize surface charges. The latent image may then be read off using a variety of approaches[84,85,86,87] which are being developed for diagnostic radiology. A description of some of these readout methods is given in Chapter 6.

To summarize, *a*-Se has the following potential advantages over existing portal imaging systems:
(i) It does not suffer from the poor optical coupling problems in fluoroscopic systems since many of the readout devices can be brought very close to or in contact with the *a*-Se. Unlike the liquid ionization chamber array, it is a fully integrating detector hence it is sufficiently sensitive for portal imaging (see Chapter 3), and provided a low noise readout is used, it can have a higher SNR_d than existing portal imaging systems (see Chapter 4).
(ii) It is thin and can be directly bonded to the metal buildup plate, which serves as the substrate[88] during the evaporation procedure used for prepare an *a*-Se layer. This along with the fact that the electric field draws the electrons and holes vertically to opposite surfaces with no spreading, maximizes resolution.
(iii) Finally, *a*-Se may be read off in real time and with some readout approaches,[84] may be made slim, making the detector less obtrusive. This would reduce the restrictions of treatment plans which result from concerns about collisions between the gantry, couch and portal imager, and permit the device to be used on existing units with beam stops. Therefore, in principle, *a*-Se can be used as the basis

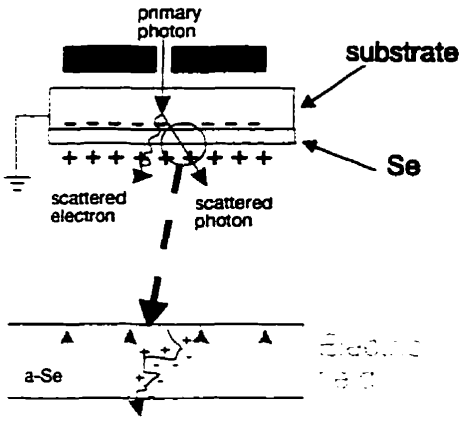

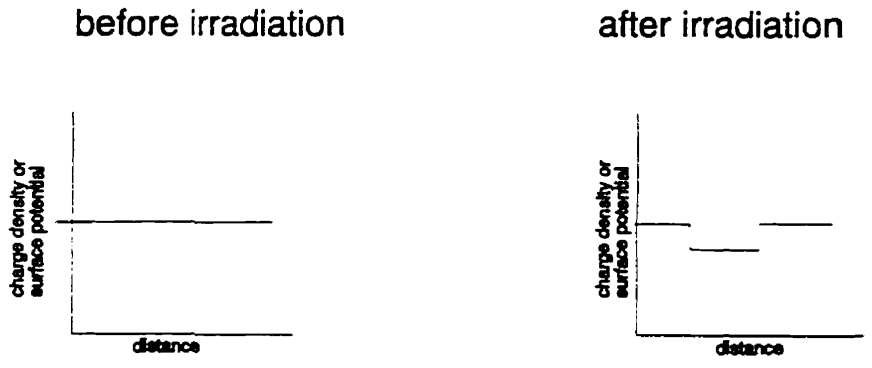

Fig. 9 Illustration of image formation process in a-Se for portal imaging. Initially the a-Se is uniformly charged and then an x-ray interacts in the buildup material (substrate) to produce a secondary electron which enters the a-Se. As it passes through the a-Se, the electron deposits energy, creating electron hole pairs. These charge carriers are drawn to opposite surfaces by the electric field (shown by vertical arrows) where they neutralize charges resulting in a latent charge image.

of a real time portal imaging system capable of producing images with improved SNR_d and resolution, possibly of diagnostic quality as calculated by Boyer *et al.*[54]

To produce a portal imaging system using *a*-Se will require both an understanding of the nature of the latent image on the surface of the *a*-Se as well as the chosen readout method. The former should lead the design of the latter. The change in surface charge density (signal) generated by a given fluence of megavoltage x-rays will depend upon the electric field, **F**, *a*-Se thickness, d_{Se}, x-ray energy and the energy deposited. Similarly, the noise properties will depend upon these parameters and the size and distribution of the energy deposition events. By understanding the signal and noise characteristics of the latent image on *a*-Se in radiation therapy beams, appropriate choices of d_{Se} and **F** for a given x-ray fluence may be made to optimize the choice and design of any readout system.

IV. OUTLINE OF THESIS

This thesis describes a comparison of the signal and noise properties of an *a*-Se based portal imaging system with the most common commercial approach - the fluoroscopic system. Chapter 2 describes measurements of the signal and noise properties of a fluoroscopic portal imager and in particular, its quantum noise. Specifically, we establish and apply a new method for measuring the x-ray quantum noise in fluoroscopic systems. We found that existing systems are not quantum noise limited due to poor optical coupling and the added noise of the video camera. Although it is possible in principle to make the systems quantum noise limited over the spatial frequency range 0-0.2 mm^{-1}, this is inadequate to meet the radiobiological and perhaps not the image quality resolution requirements of conformal therapy. Thus we concluded that a radical change in the design of the detector was worthwhile. One encouraging approach is to use a flat panel imaging system. These detectors consist

of a pixelated panel bonded to a sensor, either a phosphor screen or a photoconductor known as amorphous selenium. The physics of phosphor screens for portal imaging is well understood, however the understanding of the properties *a*-Se for portal imaging is only beginning to be explored.[89] In Chapter 3, the signal formation properties on *a*-Se in portal imaging are established. In Chapter 4, we use this information to investigate the signal and noise properties of *a*-Se for portal imaging with the goal of providing information about the resolution, signal and noise properties of the latent image on the *a*-Se surface. The motivation for this work was to determine if *a*-Se was capable of producing better portal images and compare *a*-Se for portal imaging to phosphor screens. In Chapter 5, a laser readout is used to produce portal images using *a*-Se as the sensor. It is demonstrated that image quality is improved over existing approaches by comparison of the images of a contrast-detail phantom. Images of an anthropomorphic phantom and a patient also show improvement. Chapter 6 summarizes the thesis and sets directions for future work.

REFERENCES

1. *Statistics Canada Catalogue No. 82-221-XDE*, 1992.

2. G.H. Hahn, *Hyperthermia and Cancer*, (Plenum, New York, 1982).

3. L.J. Old, "Immunotherapy for Cancer," *Sci. Am.*, **275(3)**, 136-143 (1996).

4. A. Oliff, J.B. Gibbs, and F. McCormick, "New molecular targets for cancer therapy," *Sci. Am.*, **275(3)**, 144-149 (1996).

5. J.K. Folkman, "Fighting cancer by attacking its blood supply," *Sci. Am.*, **275(3)**, 150-154 (1996).

6. A.H. Knowlton, "General principles of radiation therapy," in *Cancer Therapy*, edited by D.S. Fischer and J.C. Marsh (G.K. Hall Medical Publishers, Boston, 1982) pp. 169-175.

7. *ICRU Report 50: Prescribing, recording and reporting photon beam therapy*, (International Commission on Radiological Units, Bethesda, MD, 1993).

8. F.M. Kahn, *The Physics of Radiation Therapy*, (Williams and Wilkins, Baltimore, 1984).

9. H.R. Menick, L. Garfinkel, and G.D. Dodd, "Preliminary report of the national cancer data base," *CA - A Cancer Journal for Clinicians*, **41**, 7-18 (1991).

10. S.A. Liebel, G.J. Kutcher, L.B. Harrison, D.E. Fass, C.M. Burman, M.A. Hunt, R. Mohan, M.S. Brewster, C.C. Ling, and Z. Fuks, "Improved dose distributions for 3-D conformal boost treatments in carcinoma of the nasopharynx," *Int. J. Radiat. Oncol. Biol. Phys.* **20**, 823-833 (1991).

11. J. Hayward and M. Caleffi, "The significance of local control in the primary treatment of breast cancer," *Ann. Surg.*, **122**, 1244-1247 (1987).

12. C.K. Chung, J.A. Styker, M. O'Neill, and W.E. DeMuth, "Evaluation of adjuvant postoperative radiotherapy for lung cancer," *Int. J. Radiat. Oncol. Biol. Phys.*, **8**, 1877-1880 (1982).

13. S.E. Schild, J.A. Martenson, L.L. Gunderson, D.M. Ilstrup, K.K. Berg, M.J. OConnell, and L.H. Weiland, "Postoperative adjuvant therapy of rectal cancer: an analysis of disease control, survival and prognostic factors," *Int. J. Radiat. Oncol. Biol. Phys.*, **17**, 55-62 (1989).

14. C.A. Perez, M.V. Pilepich, and F. Zivnuska, "Tumor control in definitive irradiation of localized carcinoma of the prostate," *Int. J. Radiat. Oncol. Biol. Phys.*, **12**, 523-531 (1986).

15. G. Markhede, L. Angervall, and B. Stener, "A multivariate analysis of the prognosis after surgical treatment of soft tissue tumors," *Cancer*, **49**, 1721-1733 (1982).

16. A.W. Lee, J.S. Sham, Y.F. Poon, and J.H. Ho, "Treatment of stage I nasopharyngeal carcinoma: Analysis of the patterns of relapse and the results of withholding elective neck irradiation," *Int. J. Radiat. Oncol. Biol. Phys.*, **17**, 1183-1190 (1989).

17. P. Anderson and S. Dische, "Local tumor control and subsequent incidence of distant metastatic disease," *Int. J. Radiat. Oncol. Biol. Phys.*, **7**, 1645-1648 (1981).

18. A.S. Lichter, "Three-dimensional conformal radiation therapy: A testable hypothesis," *Int. J. Radiat. Oncol. Biol. Phys.*, **21**, 853-855 (1991).

19. M.V. Williams, J. Denekamp, and J.F. Fowler, "Dose-response relationships for human tumors: Implications for clinical trials of dose modifying agents." *Int. J. Radiat. Oncol. Biol. Phys.*, **10**, 1703-1707 (1984).

20. M. Goitein and J. Busse, "Immobilization error: Some theoretical considerations," *Radiol.*, **117**, 407-412 (1975).

21. D.M. Tait and A.E. Nahum, "Conformal therapy," *Eur. J. Cancer*, **26**, 750-753 (1990).

22. S.A. Liebel, C.C. Ling, G.J. Kutcher, R. Mohan, C. Cordon-Cordo, and Z. Fuks, "The biological basis for conformal three-dimensional radiation therapy," *Int. J. Radiat. Oncol. Biol. Phys.*, **21**, 805-811 (1991).

23. B.A. Fraass, "Development of conformal therapy," *Med. Phys.*, **22**, 1911-1921 (1995).

24. S. Takahashi, "Conformation Radiotherapy: Rotation techniques as applied to radiography and radiotherapy of cancer," *Acta Radiol. Suppl.* **242**, 1-142 (1965).

25. M. van Herk, A. Bruce, A.P. Kroes, T. Shouman, A. Touw and J.V. Lebesque, "Quantification of organ motion during conformal radiotherapy of the prostate by three dimensional image registration," *Int. J. Radiat. Oncol. Biol. Phys.*, **33**, 1311-1320 (1995).

26. G.S. Mageras, G.J. Kutcher, S.A. Leibel, M.J. Zelefsky, E. Melian, R. Mohan and Z. Fuks, "A method of incorporating organ motion uncertainties into three-dimensional conformal treatment plans," Int. J. Radiat. Oncol. Biol. Phys. **35**, 333-342 (1996).

27. J.M. Balter, H.M. Sandler, K. Lam, R.L. Bree, A.S. Lichter, and R.K. ten Haken, "Measurement of prostate movement over the course of routine radiotherapy using implanted markers," *Int. J. Radiat. Oncol. Biol. Phys.*, **31**, 113-118 (1995).

28. A. Niemierko and M. Goitein, "Modeling of normal tissue response to radiation: the critical volume model," *Int. J. Radiat. Oncol. Biol. Phys.*, **25**, 135-145 (1993).

29. S.A. Leibel, M.J. Zelefsky, G.J. Kutcher, C.M. Burman, S. Kelson and Z. Fuks, "Three-dimensional conformal radiation therapy in localized carcinoma of the prostate: interim report of a phase I dose-escalation study," *J. Urol.*, **152**, 1792-1798 (1994).

30. G.E. Hanks, A. Hanlon, T. Schultheiss, B. Corn, W.U. Shipley, W.R. Lee," Early prostate cancer: the national results of radiation treatment from the Patterns of Care and Radiation Therapy Oncology Group studies with prospects for improvement with conformal radiation and adjuvant androgen deprivation," *J. Urol.* **152**, 1775-1780 (1994).

31. G.S. Mageras, Z. Fuks, J. O'Brien, L.J. Brewster, C. Burman, C.S. Chui, S.A. Leibel, C.C. Ling, M.E. Masterson, R. Mohan *et al.*, "Initial clinical experience with computer-controlled conformal radiotherapy of the prostate using a 50-MeV medical microtron," *Int. J. Radiat. Oncol. Biol. Phys.*, **30**, 971-978 (1994).

32. S. Vijayakumar and G.T.Y. Chen, "Implementation of three dimensional conformal radiation therapy: Prospects, opportunities, and challenges," *Int. J. Radiat. Oncol. Biol. Phys.*, **33**, 979-983 (1995).

33. R.M. Henkelman, "New imaging technologies: Prospects for target definition," *Int. J. Radiat. Oncol. Biol. Phys.*, **22**, 251-257 (1991).

34. B.S. Kuszyk, D.R. Ney, and E.K. Fishman, " The current state of the art in three dimensional oncologic imaging: An overview," *Int. J. Radiat. Oncol. Biol. Phys.*, **33**, 1029-1039 (1995).

35. R. Mohan, "Three dimensional radiation treatment planning," *Australasian Physical and Engineering Sciences in Medicine*, **12**, 73-91 (1989).

36. C.X. Yu, M.J. Symons, M.N. Du, A.A. Martinez and J.W. Wong, "A method for implementing dynamic photon beam intensity modulation using independent jaws and a multileaf collimator," *Phys. Med. Biol.*, **40**, 769-787 (1995).

37. A. Brahme, "Design principles and clinical possibilities with a new generation of radiation therapy equipment," *Acta Oncol.*, **26**, 403-412 (1987).

38. C.C. Ling, C. Burman, C.S. Chui, A. Jackson, G.J. Kutcher, S. Leibel, T. LoSasso, G. Mageras, R. Mohan, E. Yorke, and Z. Fuks, "Perspectives of multidimensional conformal radiation treatment," *Radiotherapy and Oncology*, **29**, 129-139 (1993).

39. H.D. Suit, "Potential for improving survival rates for the cancer patient by increasing the efficacy of treatment of the primary lesion," *Cancer*, **50**, 1227-1234 (1982).

40. V.T. DeVita, "Progress in cancer management," *Cancer*, **51**, 2401-2409 (1983).

41. A. Dutreix, "When and how can we improve precision in radiotherapy," *Radiother. Oncol.*, **2**, 275-292 (1984).

42. J.J. Kinzie, G.E. Hanks, C.J. Maclean, and S. Kramer, "Patterns of care study:Hodgkin's disease relapse rates and adequacy of portals," *Cancer*, **52**, 2223-2226 (1983).

43. J.E. White, T. Chen, J. McCracken, P. Kennedy, H.G. Seydel, G. Hartman, J. Mira, and M. Kahn, "The influence of radiation therapy quality control on survival, response and sites of relapse in oat cell carcinoma of the lung," *Cancer*, **50**, 1084-1090 (1982).

44. A.L. Boyer and T. Schultheiss, "Effects of dosimetric and clinical uncertainty on complication-free local tumor control," *Radioth. Oncol.*, **11**, 65-71 (1988).

45. I. Daftari, P.L. Petti, J.M. Collier, J.R. Castro, and P. Samuel. "The effect of patient motion on dose uncertainty in charged particle irradiation for lesions encircling the brain stem or spinal cord," *Med. Phys.*, **18**, 1105-1115 (1991).

46. B.J. McParland, "Effects of random field placement uncertainties on tumour control probability (abstract)" *Med. Phys.*, **20**, 815 (1993).

47. A. Brahme, "Dosimetric precision requirements in radiation therapy," *Acta Radiol. Oncol.*, **23**, 379-391 (1984).

48. W. De Neve, F. Van den Heuvel, M. De Beukeleer, M. Coghe, L. Thon, P. De Roover, M. Van Lancker, and G. Storme, "Routine clinical on-line portal imaging followed by immediate field adjustment using a tele-controlled patient couch," *Radiother. Oncol.*, **24**, 45-54 (1992).

49. R.T. Droege and B.E. Bjarngard, "Influence of metal screens on contrast in megavoltage x-ray imaging," *Med. Phys.*, **6**, 487-493 (1979).

50. T. Falco and B.G. Fallone, "MTF, NPS, and DQE of metal-plate/film detectors for therapy imaging (abstract)," *Med. Phys.*, **23**, 1131 (1996).

51. P. Munro, J.A. Rawlinson, and A. Fenster, "Therapy Imaging: A signal-to-noise analysis of metal plate/film detectors," *Med. Phys.*, **14**, 975-984 (1987).

52. *AAPM Report no.24 : Radiotherapy Portal Imaging Quality*, (American Institute of Physics, New York, 1987).

53. P. Dunscombe, "Portal radiography practice in Canada," *Int. J. Radiat. Oncol. Biol. Phys.*, **24**, 177-179 (1992).

54. A.L. Boyer, L. Antonuk, A. Fenster, M. Van Herk, H. Meertens, P. Munro, L.E. Reinstein, and J. Wong, "A review of electronic portal imaging devices (EPIDs)," *Med. Phys.*, **19**, 1-16 (1992).

55. M. Van Herk, "Physical aspects of a liquid-filled ionization chamber with pulsed polarizing voltage," *Med. Phys.*, **18**, 692-702 (1991).

56. N.A. Baily, E.C. Lasser, and R.A. Keller, "Tumor localization and beam monitoring-electrofluorotomography," *Med. Phys.*, **3**, 176-180 (1976).

57. D. Vemellen, W. De Neve, F. Van den Heuvel, W. Coghe, O. Louis, and G. Storme, "On-line portal imaging: Image quality defining parameters for pelvic fields - A clinical evaluation," *Int. J. Rad. Oncol. Biol. Phys.*, **25**, 517-524 (1993).

58. J.M. Michalski, M.V. Graham, W.R. Boshc, J. Wong, R.L. Geber, A. Cheng, A. Tinger and R.K Valecenti, " Prospective clinical evaluation of an electronic portal imaging device," *Int. J. Radiat. Oncol. Biol. Phys.*, **34**, 943-951 (1996).

59. H.E. Johns and J.R. Cunningham, *The Physics of Radiology*, (Thomas, Springfield, 1983).

60. A. Rose, *Vision:Human and Electronic* (Plenum Press, New York, 1973).

61. D.E. Pearson, *Transmission and Display of Pictorial Information* (Pentech, London, 1975).

62. D.A. Jaffray, J.J. Battista, A. Fenster and P. Munro, "X-ray sources of medical linear accelerators: focal and extra-focal radiation," *Med. Phys.*, **20**, 1417-1427 (1993).

63. H.M. Norwood and B. Stubbs, "Patient motion during radiotherapy," *B.J.R.*, **57**, 155-158 (1984).

64. D.A. Jaffray, C. Chawla, C. Yu, and J.W. Wong, " Dual beam imaging for online verification of radiotherapy field placement," *Int. J. Radiat. Oncol. Biol. Phys.*, **33**, 1273-1280 (1995).

65. D.M. Galbraith, "Low-energy imaging with high-energy bremsstrahlung beams," *Med. Phys.*, **16**, 734-746 (1989).

66. D.W. Mah, D.M. Galbraith and J.A. Rawlinson, "Low-energy imaging with high energy bremsstrahlung beams: Analysis and scatter reduction," *Med. Phys.*, **20**, 653-665 (1993).

67. B.J. McParland, "Uncertainty analysis of field placement error measurements using digital portal and simulation image correlations," *Med. Phys.* **20**, 679-685 (1993).

68. F. Hurter and V.C. Driffield, *J. Soc. Chem. Ind.*, **9**, 455 (1890).

69. R. Sephton, M. Green and C. Fitzpatrick, "A new system for port films," *Int. J. Radiat. Oncol. Biol Phys.*, **16**, 251-258 (1989).

70. J. Leong, "A digital image processing system for high energy x-ray portal images," *Phys. Med. Biol.*, **29**, 1527-1535 (1984).

71. R. J. Meeder, D.A. Jaffray, and P. Munro, "Tests for evaluating laser film digitizers," *Med. Phys.* **22**, 635-642 (1995).

72. W.D. Powlis, I. Brikman, S.B. Seshadri, and P. Bloch, "Portal radiographs: digital enhancement of contrast," *Radiol.*, **169**, 839-841 (1988).

73. K.W. Leszczynski, S. Shalev, and N.S. Cosby, "An adaptive technique for digital noise suppression in on-line portal imaging," *Phys. Med. Biol.*, **35**, 429-439 (1990).

74. L.E. Reinstein, L. Alquist, H.I. Amols, and B. Lagueux, "Qualitative evaluation of a portal contrast enhancement technique," *Med. Phys.*, **14**, 309-313 (1987).

75. P. Munro, J.A. Rawlinson, and A. Fenster, "Therapy imaging: A signal-to-noise analysis of a fluoroscopic imaging system for radiotherapy localization," *Med. Phys.*, **17**, 763-772 (1990).

76. P. Munro, J.A. Rawlinson, and A. Fenster, "A digital fluoroscopic imaging device for radiotherapy localization," *Int. J. Rad. Oncol. Biol. Phys.*, **18**, 641-649 (1990).

77. W. Swindell, "The lens coupling efficiency in megavoltage imaging," *Med. Phys.*, **18**, 1152-1153 (1991).

78. T. Radcliffe, G. Barnea, B. Wowk, R. Rajapakshe, and S. Shalev, "Monte Carlo optimization of metal/phosphor screens at megavoltage energies," *Med. Phys.*, **20**, 1161-1169 (1993).

79. J.W. Boag, "Xeroradiography," *Phys. Med. Biol.*, **18**, 3-37 (1973).

80. J.N. Wolfe, L. Kalisher, and B. Considine, "Colbalt 60 Treatment Field Verification by Xeroradiography," *Am. J. Roent.*, **119**, 916-918, (1973).

81. R. Fahrig, J.A. Rowlands and M.J. Yaffe, "X-ray imaging with amorphous selenium: Detective quantum efficiency of photoconductive receptors for digital mammography," *Med. Phys.*, **22**, 153-160 (1995).

82. D.A. Jaffray, J.J. Battista, A. Fenster and P. Munro, "X-ray scatter in megavoltage transmission radiography: physical characteristics and influence on image quality," *Med. Phys.*, **21**, 45-60 (1994).

83. W. Que and J.A. Rowlands, "X-ray imaging using amorphous selenium: inherent spatial resolution," *Med. Phys.*, **22**, 365-374 (1995).

84. W. Zhao and J.A. Rowlands, "X-ray imaging using amorphous selenium: Feasibility of a flat panel self-scanned detector for digital radiology," *Med. Phys.*, **22**, 1595-1605 (1995).

85. D.M. Korn, S.P. Johnson, O.L. Nelson, and J. Ziegler, "A method of electronic readout of electrophotographic and electroradiographic images," *J. Appl. Photo. Eng.*, **4**, 178-182 (1978).

86. U. Schiebel, W. Hillen, and T. Zaengel, "Image quality in selenium-based digital radiography,"*SPIE Medicine XIV/ PACS IV*, **626**, 176-184 (1986).

87. U. Neitzel, I. Maack and S. Gunther-Kohfahl, "Image quality of a digital chest radiography system based on a selenium detector," *Med. Phys.*, **21**, 509-516 (1994).

88. H. Wang, T. Falco, and B.G. Fallone, "A metal screen-amorphous selenium based image receptor for megavoltage portal imaging (abstract)" *Med. Phys.*, **23**, 1130 (1996).

89. H. Wang, B.G. Fallone, and T. Falco, "Monte Carlo simulations of a metal/a-Se portal detector," *Radiotherapy and Oncology*, **30**, 291-297 (1996).

Chapter 2
Measurement of Quantum Noise in Fluoroscopic Systems for Portal Imaging

"Work, finish, publish"
- Michael Faraday 1791-1867

A version of this chapter was published in Medical Physics, **23**, 231-238 (1996).

I. INTRODUCTION

Fluoroscopic systems are becoming more widely used for radiation therapy portal imaging. A schematic of a typical system is shown in Fig. 1(a). The x-ray sensor consists of a metal buildup plate bonded to a phosphor screen; i.e. x-rays interact with the plate and phosphor to produce forward directed, high energy electrons which deposit energy in the phosphor. The fluorescent light produced is imaged onto the target of a video camera with a lens. Usually, a plane mirror is placed at 45° in the optical path to keep the camera out of the primary x-ray beam.

Unfortunately, the image quality of these systems is still so poor that clinically important landmarks are sometimes invisible.[1,2] Demand for improvements in image quality is expected to increase as conformal therapy develops. Previous analyses[3,4] have suggested that the poor optical coupling causes significant excess noise, thus obscuring x-ray quantum noise in fluoroscopic systems. We reduced the demagnification, M, (M=diameter of screen area viewed/diameter of active area of video tube), thus improving the light collection efficiency, thereby permitting the first measurement of the x-ray quantum noise in fluoroscopic portal imagers. The measured data was then extrapolated to a clinical M. Our goal was to understand the relationship between the x-ray quantum noise, video camera noise and the electron shot noise, and to use this information to suggest system modifications to improve image quality.

II. APPROACH

Using an optical bench as a framework, we constructed a test fluoroscopic imaging system which could operate with variable M in the single lens arrangement shown in Fig. 1(a). To change M, the

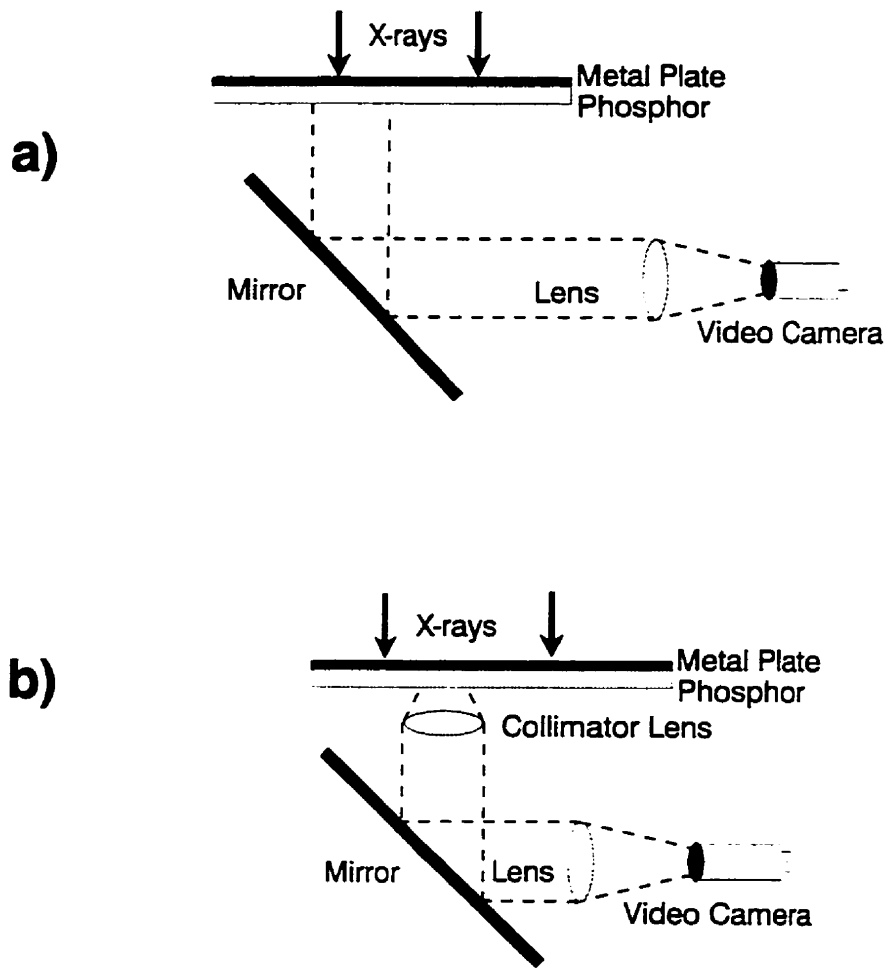

Fig. 1 a) Schematic illustration of fluoroscopic portal imager. In our test system, the same geometry was used but M could be changed by moving the lens relative to the video tube. (b) Schematic of an alternative coupling arrangement which is similar to (a) except a collimator lens has been interposed between the screen and camera lens.

camera was moved closer or further away from the screen so that a smaller or larger area of the screen was viewed.* Focus of the camera lens was established visually by observation of a monitor. The lens was moved relative to the camera target until the image of the edge of a razor blade temporarily placed on the surface of the screen appeared sharp. To maximize the light collection efficiency at small M, a relay lens assembly consisting of a collimator lens and a camera lens was also used (see Fig. 1(b)). The focal lengths, L, diameters, D_L and bulk transmissivities, τ of the lenses are given in Table I. The relay lens may be modelled by an equivalent single lens whose effective diameter is given by the smaller of the diameters of the two component lenses and whose effective focal length, L_{relay}, is given by $1/L_{relay}=1/L_{coll}+1/L_{cam}$. For the relay lens assembly, the camera lens was focussed to infinity and the collimator lens was moved relative to the screen for focussing. The x-ray sensor, a 2 mm thick brass plate bonded to a nominally 450 mg/cm^2 thick Gd_2O_2S:Tb screen**, was irradiated using an AECL Theratron 780 ^{60}Co unit (1.25 MeV gamma rays).

X-ray quantum noise in fluoroscopic portal imaging systems has not previously been measured because the number of light photons detected by the camera per interacting x-ray is too small.[3] Hence, the correlation between the burst of light photons produced at the screen by an individual x-ray is difficult to detect in the output signal current of the camera. If a greater fraction of the light burst could be detected, x-ray quantum noise should be identifiable. The fraction, ξ, of light photons emitted from a Lambertian source, (i.e. screen) and subsequently captured by a lens, is[5]:

---

*A device capable of changing the demagnification in this manner has been commercialized by Eliav Medical Imaging Systems, (PORTpro, PO Box 10404, Haifa, Israel).

** From Levy Hill Laboratories Ltd., 5 Sheffield House, Fieldings Road, Chesnut, Herts, England EN8 9TJ

Table I

Lens	L (mm)	D_L (mm)	τ
collimator	75	53	0.70
camera	50	53	0.85

Table I Description of Lenses. The camera lens had an aperture which was set at f/0.95 for all measurements. The collimator lens and camera lens were used to form a relay lens with M=1.5.

$$\xi = \frac{\tau}{4(M+1)^2(\frac{L}{D_L})^2+1} . \qquad [1]$$

Thus to detect the x-ray quantum noise, ξ should be increased. This was done by reducing M from its typical clinical value of ~35 to values approaching unity, thus permitting an increase in ξ approaching three orders of magnitude. The value of ξ required to detect an x-ray photon depends upon system noise and the number of optical photons collected per x-ray. In the absence of significant system noise, the latter quantity has been needs[6] to be ~10.

The relay lens assembly (see Fig. 1(b)) was used to measure the diameter of the active area of the camera tube, D_o. The ratio of the (manufacturer specified) focal lengths of the collimator and camera lenses is M. An optically illuminated ruler was placed in the screen plane. The diameter of the image displayed on the monitor, measured at the screen plane by viewing the image of the ruler on the monitor, was MD_o. For the single lens geometry (see Fig. 1(a)), the same procedure was followed, but this time, M was determined by dividing the diameter of the displayed image, by D_o; i.e. $M=(MD_o)/D_o$. The relationship between spatial distance at the screen plane and video scan time was determined by measuring the time on the oscilloscope between dips in the video signal produced by the lines of an optically illuminated ruler at the screen surface. To facilitate interpretation of our results, measurements performed at the camera plane were re-scaled to the input of the system at the screen plane. The relationship between the spatial frequencies at the camera plane, f_c and the spatial frequencies at the screen plane, f_s is given by:

$$f_s = \frac{f_c}{M} . \qquad [2]$$

III. CAMERA CHARACTERISTICS

In this section we describe measurements of the characteristic curve, conversion factor, dark current, and resolution of the camera. The camera used was a conventional medical fluoroscopic camera (Machlett model SS600) with a one inch Saticon tube, modified to permit multiframe integration on the camera target. This was achieved by "blanking" the electron beam readout, i.e., the beam was turned off at the beginning of a frame for an integral number of frames. This blanking permitted a buildup, or integration, of image charge on the target. After a preset integration delay, the beam was then reactivated and the accumulated charge read off. Thus, the camera could integrate for several frames, or could operate in its normal fashion with continuous scanning.

The characteristic curve of the camera was measured in two ways: (i) signal current (I_s) as a function of light intensity for continuous scanning and (ii) I_s as a function of integration time at constant light intensity. The light source for these measurements consisted of green LEDs in an integrating sphere[7] which ensured a uniform spatial distribution over the output port. The camera lens was focussed on the edge of a razor blade temporarily placed on the surface of the output port. At a separate port, the light output of the sphere, which was adjusted by changing the current to the LED source, was monitored using a photodiode photometer. To minimize the effects of lens vignetting,[8] all measurements were confined to the central ~7 mm of the camera target. We found that over this central region, I_s was constant to within ±10%. The characteristic curves of the camera are shown in Fig. 2. The curves are non-linear below a 100 mV signal but became linear between 100 and 700 mV. By directly injecting current into the target electrode and noting that the non-linearity was still present, we established that the non-linearity was due to the camera preamplifier. All noise measurements (see section IV) were confined to the range of signal 200-300 mV, well within the linear region.

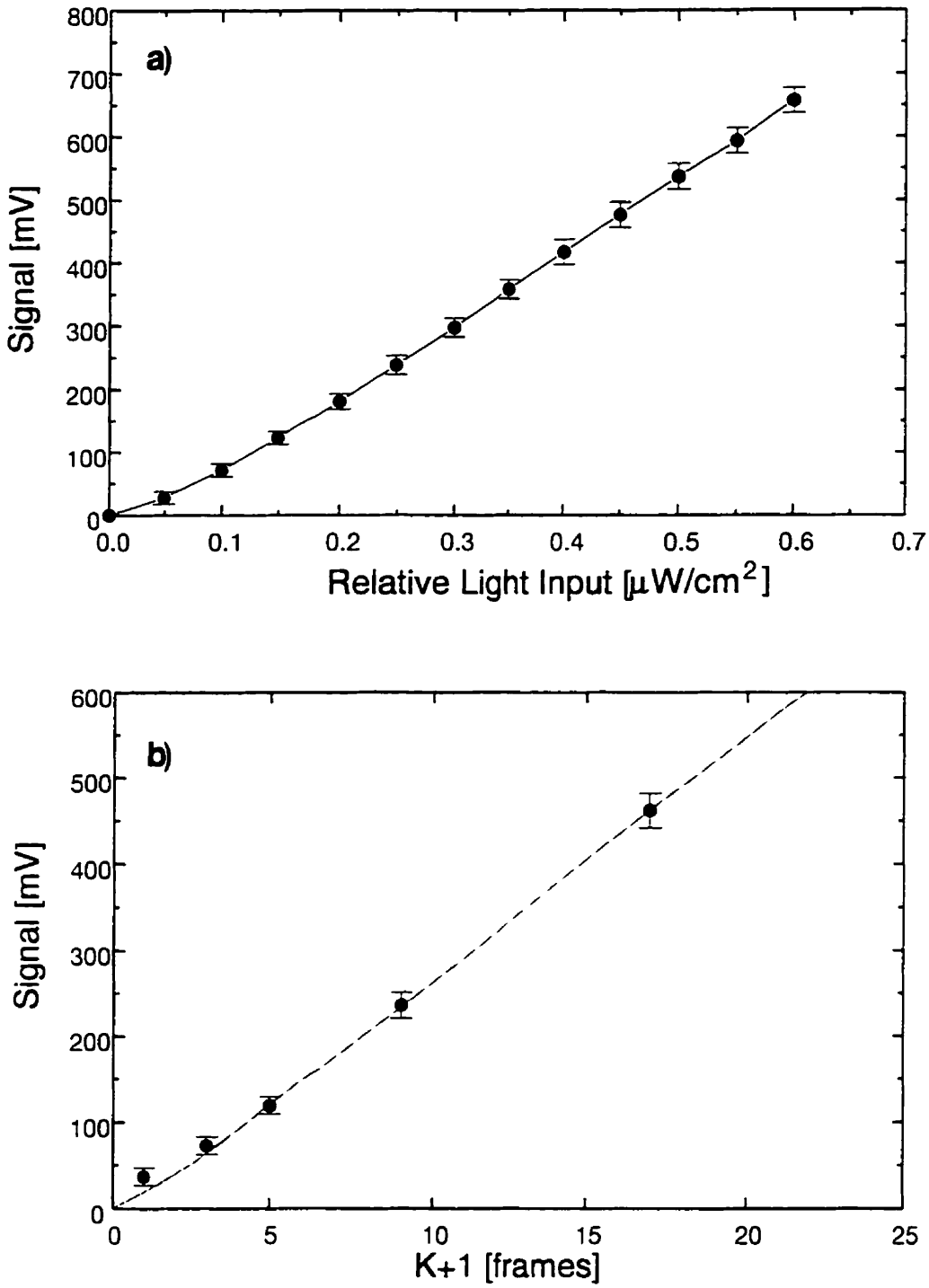

Fig. 2 Video camera signal as a function of light input measured in two different ways, (a) using a uniform green light source set to variable intensities measured using a photometer (b) with the same light source, but variable target integration times.

The conversion factor of the camera is the ratio of the signal current (I_s) to the camera output signal potential (V_s). It was directly measured by applying a square wave current, I_s, into the camera voltage amplifier using a waveform generator and measuring V_s on an oscilloscope per I_s. To confirm this result, the average signal current was measured from the potential drop produced across a 1.1 MΩ resistor using a multimeter. (The resistor was part of a jumper circuit designed by the camera manufacturer for this purpose). The measured average current was corrected for the retrace time (16% of total time) of the video signal. A correction for the fraction of the time spent scanning the circular field of view to the total scan time[9] was also made to obtain I_s. By averaging the results from the two methods, the camera conversion factor was determined to be 0.65 mV/nA (±5%).

The camera dark current was measured with the camera covered by an opaque cloth and the electron beam blanked for K frames. The current resulting from K+1 frames was then measured using an oscilloscope. The dark current was found to be less than 5 nA after an integration time of 68 s (K=2048). Dark current was therefore negligible (<22 pA) for the values of K (1-2) used in subsequent measurements.

The resolution of the camera and relay lens combination was measured from an optical line spread function (LSF) resulting from an illuminated 5 μm slit[***] placed at the focal plane of the collimator lens. The LSF was obtained using a selected video line from the camera, measured on a digital oscilloscope whose gain was set to the largest possible value without saturation so as to minimize digitization noise from the 8-bit analog to digital (A/D) converter. The line was averaged 256 times to reduce noise and digitized at 25 megasamples/s in the oscilloscope. The temporal sampling interval of 40 ns corresponded to a spatial distance of 14 μm at the camera plane and the full 512 point LSF.

[***] Melles Griot, Irvine, California

a distance of ~ 7 mm. The LSF was transferred to an IBM PC compatible computer (using the IEEE 488 digital instrumentation bus) where it was fast Fourier transformed to obtain the modulation transfer function of the camera and lenses, $MTF_c'(f_c)$.

IV. NOISE POWER SPECTRA

The primary goal was to measure the x-ray quantum noise in our test fluoroscopic system as a function of M. In a fluoroscopic system, the total noise power measured during irradiation, $NPS_X(f_c)$ consists of three components: (i) the x-ray quantum noise power spectrum, $NPS_q(f_c)$; (ii) the video camera noise power spectrum arising from the amplifier, $NPS_v(f_c)$; and (iii) the electron shot noise power spectrum, $NPS_e(f_c)$. If the same signal current is produced using a light source, the resulting noise power spectrum, $NPS_L(f_c)$ consists only of the video amplifier and electron shot noises. Thus, assuming NPS_X and NPS_L are independent, $NPS_q=NPS_X-NPS_L$. The $NPS_q(f_c)$ includes both the fluctuations associated with x-ray interactions and the additional noise associated with the distribution of energy deposition events,[10] but not the fluctuations associated with the detection of light quanta at the camera target. To calculate this latter source of noise, we assumed that each detected light photon released a single electron on the video target. The light quantum noise is thus equivalent to the electron shot noise on the camera signal current, I_s. The electron shot noise is given by[11]

$$\int_0^B NPS_e(f_c)df_c = 2I_sBe \ , \qquad [3]$$

where B is the bandwidth of the measuring system and e is the charge of an electron. The $NPS_e(f_c)$ is assumed to be constant as a function of f_c, but is shaped by the low pass (5 MHz) filter that we introduced to prevent aliasing with the 25 megasamples/s A/D converter in the oscilloscope used for

measurement of the noise power spectrum (see section IV). The response of this filter was measured using an oscilloscope and a waveform generator.

For measurement of the noise power spectrum under illumination, $NPS_L(f_c)$, two light sources were used: an incandescent source (used in the clinic) and the LED source. It was confirmed that for the same I_s, the $NPS_L(f_c)$ was the same for either light source. The $NPS_X(f_c)$ for the test fluoroscopic system was acquired from the digitized video signal during flat field irradiation.[16] In the signal range ~200-300 mV, individual point scans consisting of a selected video line were acquired using a digital oscilloscope. Each such realization was digitized in the same manner as the LSF measurement (see section III) except there was no averaging of the video line. Sequential point scans were subtracted (to remove structural noise), then Fourier transformed and the resulting spectrum was stored. This procedure was repeated q times ($q \geq 200$) and the spectra averaged. For statistically independent noise realizations, the noise power is equivalent in each realization. Thus subtracting two realizations doubles the noise power which was corrected by division by two. The statistical uncertainty in noise power spectra has been shown[12] to be $(2/q)^{1/2}$.

To assess if leakage radiation was generating spurious signals, the camera lens was covered with an opaque material and the signal current was measured under irradiation using an integration time of three frames. No additional signal (within the 2 mV rms noise) was observed demonstrating that no significant signal or noise was being generated by stray radiation.

During x-ray noise power measurement, the collimating lens was in the therapy beam. This irradiation resulted in progressive darkening[13] of the lens. We measured the bulk transmission (τ) of the collimating lens before and after each irradiation using a green He-Ne laser (λ= 543 nm; c.f.

Gd_2O_2S:Tb has a peak spectral fluorescence at ~550 nm) and a photodiode photometer. The ~ 1 mm diameter laser beam was directed at the centre of the 1 cm diameter photodiode and the ratio of the resultant signals with and without the lens was found and equated to τ. We observed that an irradiation at a dose rate of ~300 cGy/min for 5 minutes resulted in a 20% loss in transmission. Our noise power measurements were performed over a comparable time period, but the subtraction of sequential lines taken ~1 s apart eliminated any errors due to lens darkening. A practical implication from our observation of lens darkening is that the lenses in fluoroscopic portal imaging systems in routine clinical use could also be damaged by leakage radiation over their lifetime. Quality assurance programs for portal imagers should take the possibility of such an effect into account.

In Figs. 3(a) - 3(d), the measured x-ray $NPS_X(f_c)$ and optical $NPS_L(f_c)$ are plotted as a function of f_c at the camera plane for M between 1.5 and 14. Also shown in Fig. 3(a) is the electron shot noise power spectrum, $NPS_e(f_c)$ calculated using Eq. 3, the filter response function and the camera conversion factor. The $NPS_e(f_c)$ is negligible compared to the $NPS_L(f_c)$. This implies that under illumination, the overwhelming source of noise is the camera amplifier (i.e. $NPS_v(f_c) \approx NPS_L(f_c)$). The triangular shape of the video camera noise, $NPS_v(f_c)$, arises from two effects. First, vidicons require increasing gain versus frequency in the amplifier. This is required to maintain a flat signal frequency response to compensate for the unavoidable low pass filtration imposed by the stray capacitance of the target to ground.[14] Second, the upper frequency rolloff is imposed by the 5 MHz antialiasing filter. The x-ray quantum noise power spectra, $NPS_q(f_c)$, at different M, are shown in Fig. 3(e). The x-ray quantum noise is concentrated at low f_c for small M but shifts to higher f_c as M increases. This shift is due to the measurement at the camera plane rather than the screen plane.

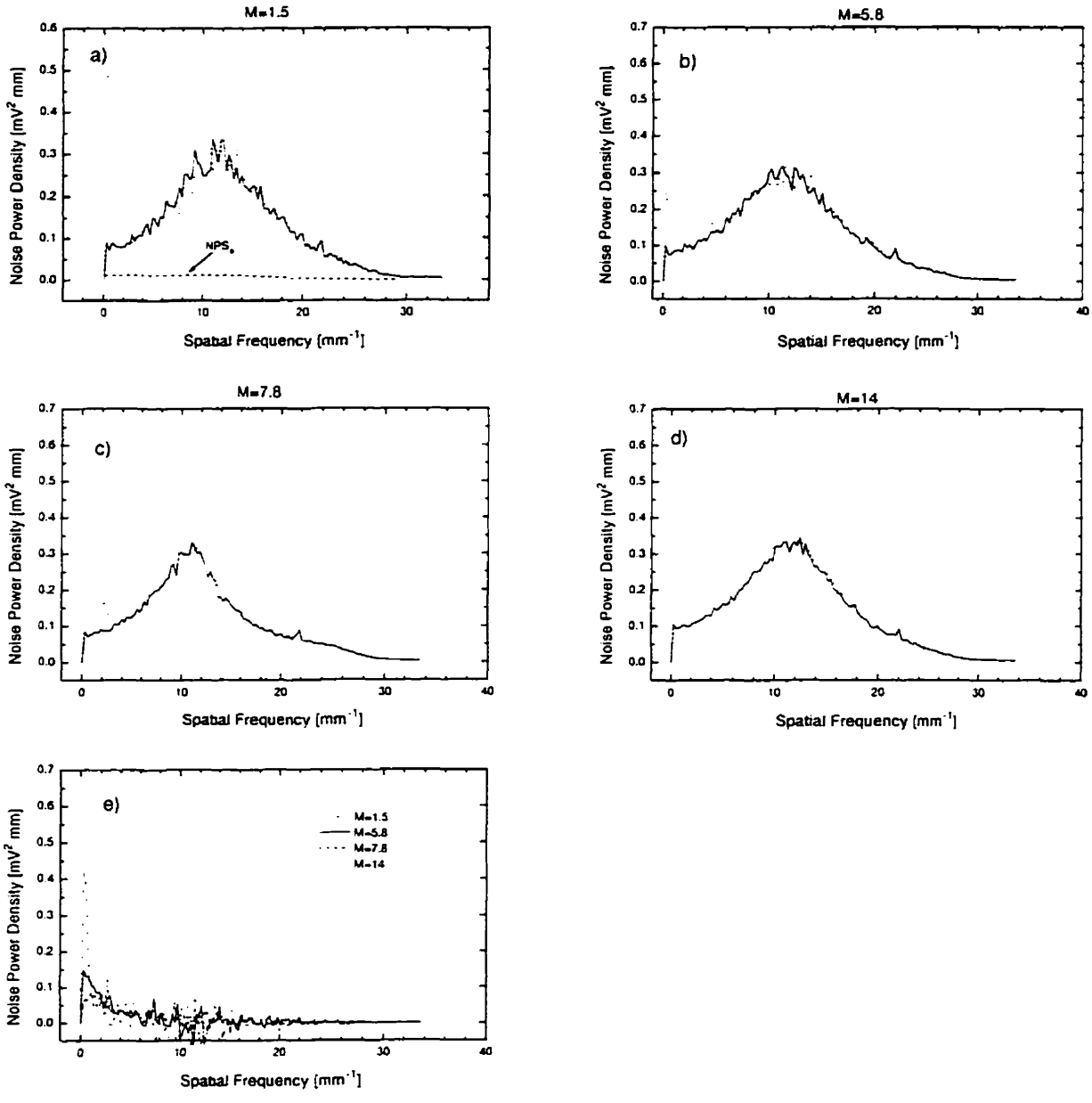

Fig. 3 Noise power spectra at camera plane for various magnifications (a) M=1.5, (b) M=5.8, (c) M=7.8 and (d) M=14. The NPS_L (——) were acquired at I_s~200 mV level produced by using an incandescent light to illuminate the camera. The NPS_x (·····) were acquired at the same signal level, but using ^{60}Co and the metal plate/phosphor. Also shown in (a) is the calculated shot noise at the same I_s. (e) Quantum noise power spectra at camera plane for different M which are obtained as the differences between the curves in (a), (b), (c) and (d).

Thus, in Fig. 4, the quantum noise is rescaled to the screen plane and compared to the electron shot noise at M=1 and M=35, the clinical demagnification corresponding to a 40 cm diameter field of view. The electron shot noise ($NPS_e(f_s)$) were calculated using Eqs. 2 and 3 and are shown in Fig. 4. At M=35, two $NPS_e(f_s)$ are shown, one with the effect of the low pass filter and one without. The curve with the filter represents the real $NPS_e(f_s)$ for our test system, however, the $NPS_e(f_s)$ without the filter is what could theoretically be achieved using a filter with a higher cutoff frequency.

The quantum noise power ($NPS_q(f_s)$) curves are the same data as in Fig. 3(e) but with f_c rescaled to f_s as described in Eq. 2 under the constraint that the total noise power (given by the integral of the NPS) must remain invariant of its plane of reference. As a result of applying Eq. 2, the sampling interval at the screen plane varied with M resulting in both a reduced frequency range and an increased density of data points/spatial frequency for larger M. The data were smoothed by using a box averaging filter that had a width equal to M. The noise is thus averaged over the same bin width for all values of M as for M=1. Two minor corrections were performed to account for differences between the dose rate and optical coupling at different M. First, the $NPS_q(f_s)$ was normalized to a constant x-ray photon fluence by multiplying by the dose correction factors listed in Table II. Second, the differences between I_s at different M for the same x-ray fluence are due to differences in optical coupling. Thus the $NPS_q(f_s)$ curves were also divided by the ratio of the corrected signal squared (Table II) to a constant $I_s^2 = (230\ mV)^2$.

The $NPS_q(f_s)$ obtained in the range M=1.5 to M=14 are identical within experimental error. This is to be expected since the same x-ray fluence is being detected, hence, the x-ray quantum noise per unit area is constant. Ignoring the effect of the 5 MHz filter, at M=35, the $NPS_q(f_s)$ is greater than the $NPS_e(f_s)$ for f_s~0-0.5 mm^{-1}; thus over this range of f_s, the system is potentially x-ray quantum noise

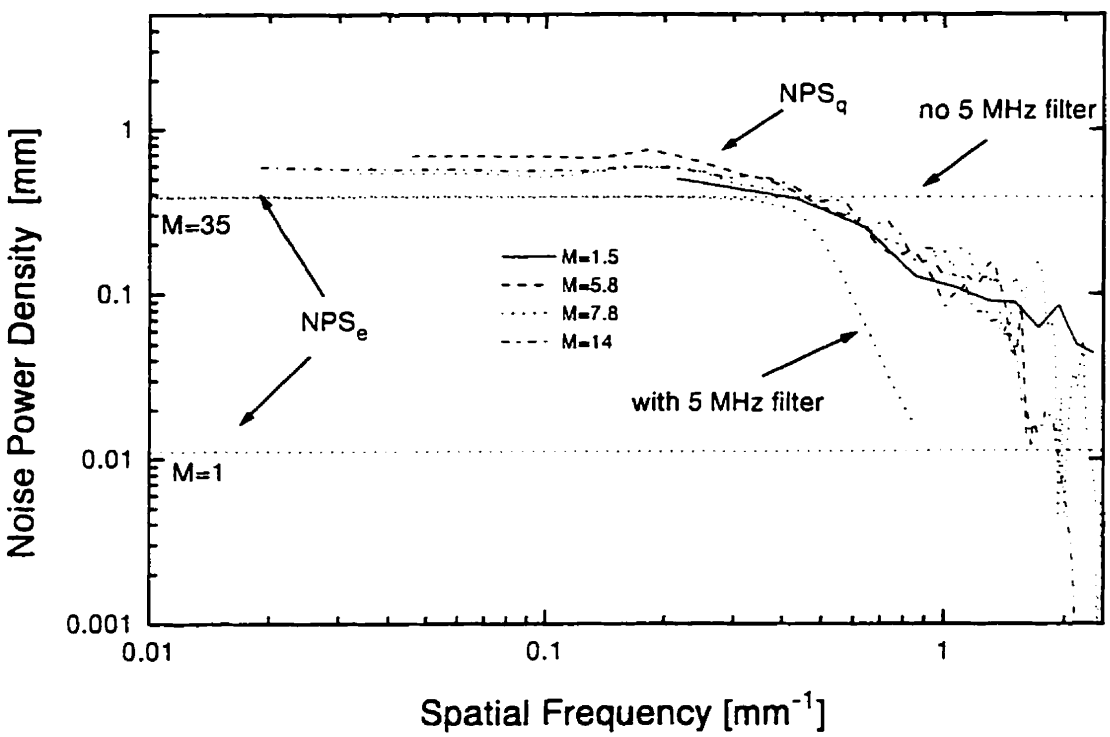

Fig. 4 Measured quantum noise ($NPS_q(f)$) and electron shot noise ($NPS_e(f)$) for M=1.5 to 14 for a constant photon fluence corresponding to 400 cGy/min to water at d_{max} referenced to the screen plane. Data normalized to a 230 mV signal. The horizontal lines are the shot noise at different M calculated using Eq. 3. The shape of the $NPS_e(f_s)$ is shown with the filter and without the filter.

Table II

M	$\dot{D}_A$ (cGy/min)	I_s (mV)	Dose Correction factor	Optical coupling factor	Corrected I_s (mV)
1.5	376	223	1.06	1.05	248
5.8	356	200	1.123	0.983	221
7.8	327	183	1.22	0.948	212
14.5	467	300	0.856	1.25	321

Table II Measured values of dose rate, signal, correction factors and corrected signal. The dose rate correction factor is given by 400 cGy/min/$\dot{D}_A$ where $\dot{D}_A$ is the actual dose rate to water at 0.5 g/cm^2 (d_{max}) at the screen position for K=2. The optical coupling factor was calculated as (I_s x dose correction factor) ^{2}/(230 mV)^2.

limited. Since the 5 MHz filter cuts off at a lower f_s than the quantum noise, we expect that this range is slightly reduced because the $NPS_q(f_s)$ will fall off at least as fast as the low pass filter. The effects of the filter and $MTF_c'(f_s)$ on the shape of the $NPS_q(f_s)$ are discussed below.

The shape of the quantum noise power spectrum may be approximated[15] by the modulation transfer function squared ($MTF_s^2(f_s)$) if: (i) the system is linear, (ii) the input noise is white and (iii) the gain is sufficient.[6] Thus wecan compare the shapes of the $MTF_s^2(f_s)$ and the quantum noise power spectrum. We measured the point scanned quantum noise power spectrum ($NPS_q(f_s)$),[16] so its shape is approximated by the point scanned modulation transfer function of the screen squared ($MTF_s'^2(f_s)$). The $MTF_s'(f_s)$ is obtained by taking the line integral through the rotationally symmetric $MTF_s(f_s)$ so that

$$MTF_s'(f_s) = \int_{-\infty}^{\infty} MTF_s(f_s,h)\, dh \,, \qquad [4]$$

where h is a dummy integration variable. If the $MTF_s(f_s)$ is a rotationally symmetric Gaussian then $MTF_s(f_s)$ is identical[16] to $MTF_s'(f_s)$. Since the $MTF'(f_s)$ of the screen is approximately Gaussian, application of the transformation in Eq. 4 results in an $MTF_s'(f_s)$ similar in shape to the $MTF_s(f_s)$.

In Fig. 5, the average of the quantum noise curves ($NPS_q(f_s)$) from Fig. 4 is compared to the $MTF_s'^2(f_c)$ obtained using Eq. 4 and a previously measured[17] $MTF(f_s)$. There is good agreement between the shapes of the $MTF_s'^2(f_s)$ and the $NPS_q(f_s)$. From the shape of the $NPS_q(f_s)$ curves in Fig. 4, we conclude that the $NPS_q(f_s)$ is proportional to $MTF_s'^2(f_s)$ for all M up to M=14. The constancy of the $NPS_q(f_s)$ when normalized to the screen plane and its similarity to the $MTF_s'^2(f_s)$ provide confirmation that this is indeed x-ray quantum noise.

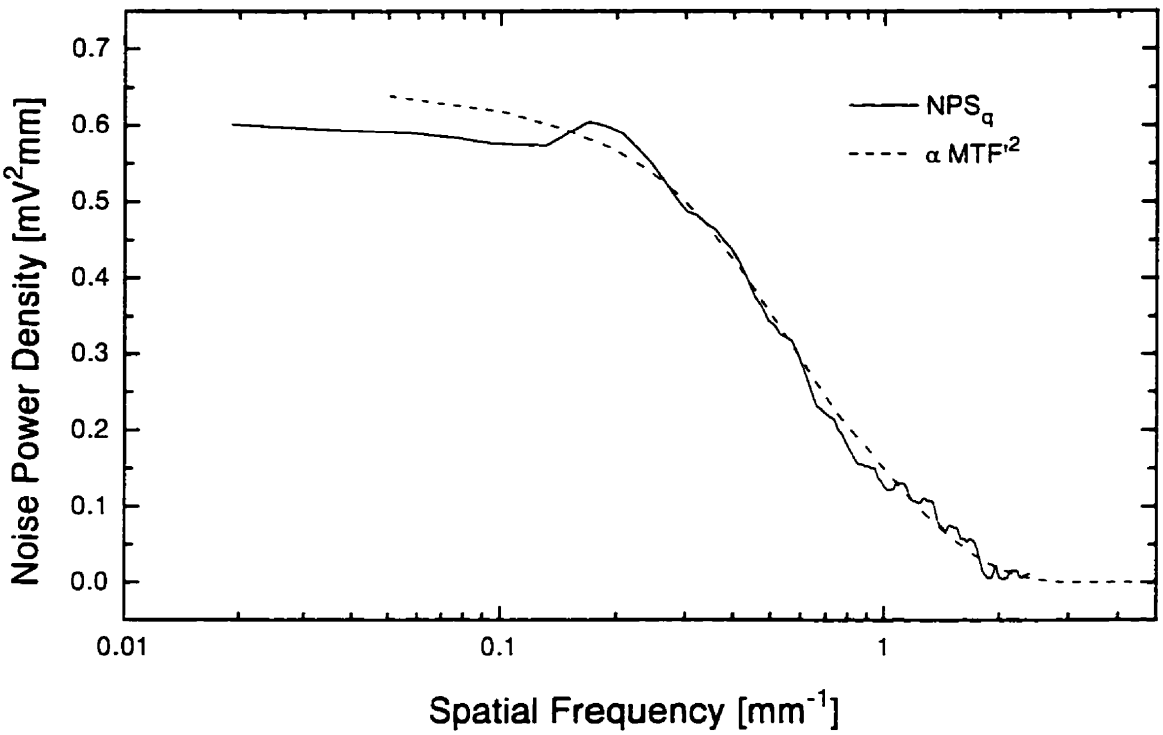

Fig. 5 Comparison of shape of point scanned modulation transfer function squared ($MTF^2(f_s)$) and the average of the quantum noise power spectra ($NPS_q(f_s)$) from the curves in Fig. 4.

The $MTF_c'(f_s)$ was calculated from the measured $MTF_c'(f_c)$ of the camera and lenses together using Eq. 2. They are shown in Fig. 6(a) for different values of M. For all M, the quantum noise ($NPS_q(f_s)$) is shaped by the product of the $MTF_s'^2(f_s)$ of the screen and the $MTF_c'^2(f_s)$ of the camera/lens combination. For $M \leq 20$, the $MTF_c'(f_s)$ of the camera/lens is essentially unity compared to the $MTF_s'(f_s)$ of the screen, thus no correction for the $MTF_c'(f_s)$ of the camera and lens combination was required for our measured data. However as M approaches and exceeds ~20, the $MTF_c'^2(f_s)$ of the camera/lens combination begins to contribute and eventually becomes the dominant term. Fig. 6(b) shows the shape of the $MTF'^2(f_s)$ of the camera/lens, screen and the product of the two curves, $MTF_p'^2(f_s)$, at M=35. Also shown is the square of the response function of the 5 MHz filter (MTF'^2_{filter}). At M=35, we expect the shape of the $NPS_q(f_s)$ curves to be the same as the $MTF_p'^2(f_s)$, thus we define $NPS_p(f_s)=NPS_q(0)\cdot MTF_p'^2(f_s)$. In Fig. 6(c), we compare the $NPS_q(f_s)$ and $NPS_e(f_s)$ from Fig. 4 to the $NPS_p(f_s)$. The $NPS_q(f_s)$ shown in Fig. 4 overestimates the amount of high spatial frequency noise because it does not take into account the blurring of the camera and lens at M=35. It represents the $NPS_q(f_s)$ due to blurring by the screen only, while the lens blurred quantum noise power spectrum, $NPS_p(f_s)$ in Fig. 6(c) is a better estimate of the quantum noise at M=35 for our test system. The $NPS_p(f_s)$ is greater than the $NPS_e(f_s)$ for f_s~0-0.2 mm^{-1} implying that the system is potentially quantum noise limited over this range. Since the electron shot noise ($NPS_e(f_s)$) is shaped by the 5 MHz filter and since the lens blurred quantum noise ($NPS_p(f_s)$) falls off more quickly than the $NPS_e(f_s)$, this implies that the filter does not significantly affect the shape of the $NPS_p(f_s)$ at M=35.

Fig. 7 compares the $NPS_p(f_s)$, $NPS_e(f_s)$ and $NPS_v(f_s)$ at the clinical demagnification (M=35). The $NPS_v(f_s)$ curve was obtained from Fig. 3 and the x-ray quantum noise and electron shot noise were taken from Fig. 4. The amplifier is the dominating noise source at all f_s. The ratio, θ, of the amplifier noise to x-ray quantum noise depends[14] upon the design of the amplifier and field effect transistor

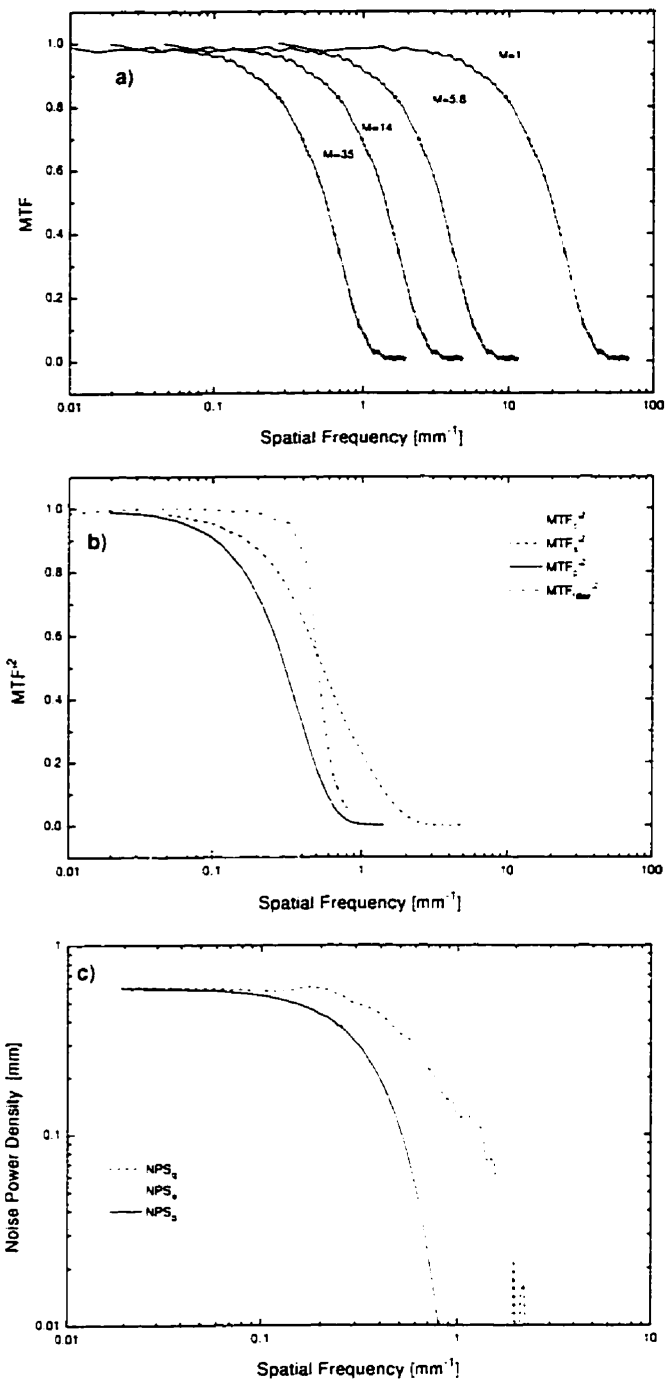

Fig. 6 (a) $MTF_c(f_s)$ of the camera and lenses for different values of M referred to the screen plane in the horizontal scan direction. (b) MTF^2 of camera/lens (MTF_c^2), the screen (MTF_s^2), and the product of the two curves (MTF_p^2) referenced to the screen plane at M=35. Also shown is the response function of the 5 MHz filter. (c) Comparison of the $NPS_e(f_s)$, the $NPS_q(f_s)$ taken from the average of the $NPS_q(f_s)$ curves in Fig. 4 with the $NPS_p(f_s) \alpha MTF_p^2(f_s)$.

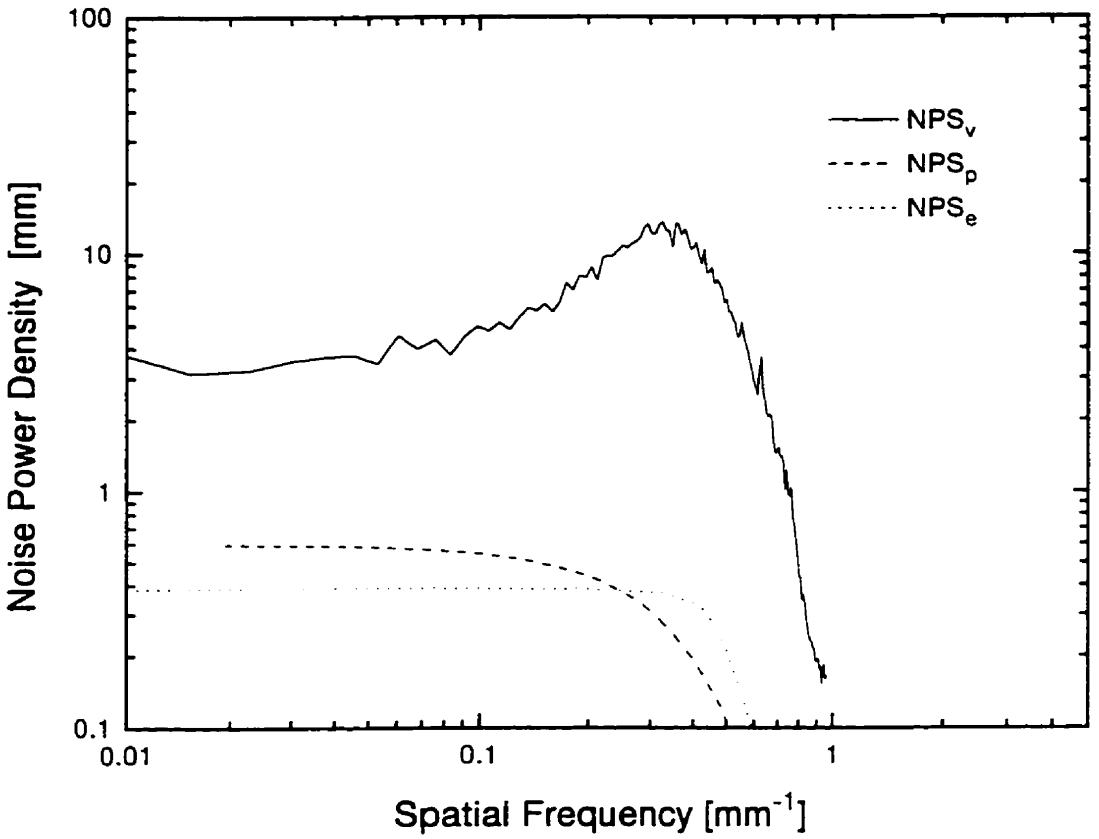

Fig. 7 Comparison of lens blurred quantum noise ($NPS_p(f_s)$), electron shot noise ($NPS_e(f_s)$) and amplifier noise ($NPS_v(f_s)$) at M=35 for a 230 mV signal. The $NPS_v(f_s)$ was measured at M=1.5 and rescaled to M=35. The $NPS_p(f_s)$ was taken from the shape of the $MTF_p'^2(f_s)$ curve in Fig. 6(c).

(FET) used, I_s, f_s and M. For our amplifier, at M=35, with a 230 mV signal at f_s=0.2 mm^{-1}, θ~33 whereas at f_s=0.02 mm^{-1}, θ is reduced to ~6. The x-ray quantum noise is more than the electron shot noise at M=35 for f_s~0-0.2 mm^{-1}. Since amplifier noise is the only source of noise greater than x-ray quantum noise, it must be amplifier noise which is preventing the system from being x-ray quantum noise limited.

V. DISCUSSION

We have shown that our test fluoroscopic portal imaging system is dominated by amplifier noise. What approaches could be used to reduce this source of noise ? Decreasing the input capacitance of the first stage of the amplifier, which is typically a field effect transistor (FET) or slow scanning of the electron beam over the video target are two possible approaches as is the use of a low noise CCD. The coupling of light between the camera and the screen can be increased by using a lens with a larger aperture (e.g. f/0.75 lens) but this may lead to greater lens vignetting effects. Further possible approaches for increasing the signal, and hence the SNR are: (i) an increased target area, (ii) an increased target storage capacitance (~ gain of 2),[18] or (iii) using amplified target methods (gain of 10-100).[19,20] However, these approaches must take into account the effects of dose rate, dynamic range and readout noise of the detector. For the system to become quantum noise limited, the quantum noise power must increase by a factor of ~30, or alternatively the SNR must increase by a factor of $30^{1/2}$ ~5. We believe that a combination of the above approaches can yield this level of improvement.

If we could produce an x-ray quantum noise limited system, then Fig. 7 implies that the system would be x-ray quantum noise limited to a spatial frequency of approximately f_s=0.2 mm^{-1}. How does this limit compare to the important spatial frequencies in portal imaging ? As discussed in Chapter 1, the

required spatial resolution has been estimated to be ±1 mm (or a spatial frequency of ~ 0.5 mm^{-1}) based upon biological modelling of the tumour control probability.[21] This estimate of the required resolution is conservative and perhaps insufficient for identification of landmarks (see section III.A. in Chapter 1). However, the x-ray quantum noise limit does not extend to this spatial frequency and to make it do so would require a reduction in M and a subsequent reduction in the field of view which may not be clinically acceptable.[22] An new approach is to increase the optical coupling through other readout approaches such as the system being developed by Antonuk *et al.*[23] These systems employ a matrix of photodiodes which read out the optical image on the phosphor. An alternative version[24,25] of the flat panel uses a photoconductor known as amorphous selenium (*a*-Se) to produce a charge image which can be read out. To determine if such a sensor is appropriate for portal imaging, in the next two chapters, the signal and noise properties of the latent image on the *a*-Se are explored.

V. CONCLUSIONS

This chapter has described the development of a general method to measure the x-ray quantum noise in fluoroscopic portal imaging systems. It can be applied to existing portal imaging systems to make noise evaluations and assist in redesign and optimization. Using an experimental system, we found by extrapolation to the large M used in portal imaging, that the amplifier noise dominates the x-ray noise by as much as a factor of ~ 30. Although it is possible to produce a quantum noise limited system with significant technical modifications, the range of spatial frequencies over which the system can be made quantum noise limited is only 0-0.2 mm^{-1}, and may be inadequate. Moreover, vast improvements in SNR are available if the optical coupling could be improved. Thus, this work indicates that portal image quality can be significantly improved by altering the readout of the primary detector.

REFERENCES

1. D. Vernellen, W. De Neve, F. Van den Heuvel, W. Coghe, O. Louis, and G. Storme, "On-line portal imaging: Image quality defining parameters for pelvic fields - A clinical evaluation." *Int. J. Rad. Oncol. Biol. Phys.*, **25**, 517-524 (1993).

2. W. De Neve, F. Van de Heuvel, M. De Beukeleer, M. Coghe, L. Thon, P. De Roover, M. Van Lancker, and G. Storme, "Routine clinical on-line portal imaging followed by immediate field adjustment using a tele-controlled patient couch," *Radiother. Oncol.*, **24**, 45-54 (1992).

3. P. Munro, J.A. Rawlinson, and A. Fenster, "A digital fluoroscopic imaging device for radiotherapy localization," *Int. J. Rad. Oncol. Biol. Phys.*, **18**, 641-649 (1990).

4. W. Swindell, "The lens coupling efficiency in megavoltage imaging," *Med. Phys.*, **18**, 1152-1153 (1991).

5. H. Liu, A. Karellas, L.J. Harris, and C.J. D'orsi, "Methods to calculate the lens efficiency in optically coupled CCD x-ray imaging systems" *Med. Phys.*, **21**, 1193-1195 (1994).

6. A.D. Maidment and M.J. Yaffe, "Analysis of the spatial-frequency-dependent DQE of optically coupled digital mammography detectors," *Med. Phys.*, **21**, 721-729 (1994).

7. J.A. Rowlands, K.S. Schulenburg, and G. DeCrescenzo, "A light source for testing radiological television cameras," *Med. Phys.*, **16**, 1-6 (1989).

8. R. Kingslake, "Recording Equipment: Lenses" in *Cinefluorography*, edited by G.H.S. Ramsey, J.S. Watson., T.A. Tristan, S. Weinberg, and W.S. Cornwell, (Charles C. Thomas, Springfield, Illinois, 1960).

9. J.A. Rowlands, "Television camera design and specification," in *Proceedings of the AAPM Summer School 1991: Specification, Acceptance Testing, and Quality Control of Diagnostic X-ray Imaging Equipment* pp. 511-530.

10. R.K. Swank, "Absorption and noise in x-ray phosphors," *J. Appl. Phys.*, **44**, 4199-4203 (1973).

11. L.R. Fortney, *Principles of Electronics: Analog and Digital*, (Harcourt Brace Jovanovich, Toronto, 1987), pp. 545-548.

12. J.C. Dainty and R. Shaw, *Image Science*, (Academic Press, New York, 1974), pp. 285-286.

13. P.W. Levy, "Color Centers" in *Encyclopedia of Physics*, edited by R.G. Lerner and G.L. Trigg, (VCH Publishers, Inc, New York, 1990), pp. 162-171.

14. "Imaging Tubes" in *The Infrared Handbook*, edited by W.L. Wolfe and G.J. Zissis, (Environmental Research Institute of Michigan, Infrared Information and Analysis Center, Washington, 1985).

15. G. Lubberts, "Random noise produced by x-ray fluorescent screens," *J. Opt. Soc. Am.*, **58**, 1475-1483 (1968).

16. J.A. Rowlands and G. DeCrescenzo, "Wiener noise power spectra of radiological television systems using a digital oscilloscope," *Med. Phys.*, **17**, 58-64 (1990).

17. P. Munro, J.A. Rawlinson, and A. Fenster, "Therapy imaging: A signal-to- noise analysis of a fluoroscopic imaging system for radiotherapy localization," *Med. Phys.*, **17**, 763-772 (1990).

18. S. Nudelman, H. Roehrig, and M.P. Capp, "A study of photoelectronic -digital radiology- Part III: Image acquisition components and system design," *Proc. IEEE.*, **70**, 715-727 (1982).

19. K. Tanioka, J. Yamazaki, K. Shidara, K. Taketoshi, T. Kawamura, S. Ishioka, and Y. Takasaki, "An avalanche-mode amorphous selenium photoconductive layer for use as a camera tube target," *IEEE Elect. Dev. Let.*, **EDL-8**, 392-394 (1987).

20. J. Yamazaki, K. Tanioka, and K. Shidara, "Development of the Super-HARP camera, a rival for the human eye for the next generation of broadcasting," *SMPTE*, **101**, 322-4 (1992).

21. B.J. McParland, "Effects of random field placement uncertainties on tumor control probability," (abstract) *Med. Phys.*, **20**, 815 (1993).

22. A. Ezz, P. Munro, A.T. Porter, J. Battista, D.A. Jaffray, A. Fenster and S. Osborne, "Daily monitoring and correction of radiation field placement using a video-based portal imaging system: A pilot study," *Int. J. Radiat. Oncol. Biol. Phys.*, **22**, 159-165 (1992).

23. L.E. Antonuk, J. Boudry, W. Huang, D.L. McShan, E.J. Morton, J. Yorkston, M.J. Longo, and R.A. Street, " Demonstration of megavoltage and diagnostic x-ray imaging with hydrogenated amorphous silicon arrays," *Med. Phys.*, **19**, 1455-1466 (1992).

24. W. Zhao and J.A. Rowlands, "X-ray imaging using amorphous selenium: Feasibility of a flat panel self-scanned detector for digital radiology," *Med. Phys.*, **22**, 1595-1605 (1995).

25. D.L. Lee, L.K. Cheung, and L.S. Jeromin, "A new digital detector for projection radiography," *Proc. SPIE*, **2432**, 237-249 (1995).

Chapter 3

Portal Imaging using Amorphous Selenium: Sensitivity to X-rays from 40 kVp to 18 MV

"When I was directing the research work of students in my days at Princeton University. I always used to tell them that if the result of a thesis problem could be forseen at its beginning it was not worth looking at"

- Karl Taylor Compton 1887-1954

A version of this chapter has been submitted to Medical Physics (1997).

I. INTRODUCTION

The use of photoconductors, in general, and amorphous selenium (*a*-Se) specifically, is a topic of active research in medical x-ray imaging. To date, *a*-Se has been used in commercial systems for mammography[1] and digital chest radiography[2] and is under active consideration for digital mammography,[3] general radiography[4] and fluoroscopy.[5] Photoconductors are useful as x-ray imaging sensors because provided an appropriate electric field is applied, they have a high sensitivity (i.e. conversion of absorbed x-ray energy to charge). Although it has been shown that it is possible to use *a*-Se to produce radiation therapy verification (portal) images,[6,7] there have only been limited investigations[8,9] of the sensitivity of *a*-Se to megavoltage x-ray beams.

We have measured the sensitivity of *a*-Se to x-ray beams ranging in energy from 40 kVp to 18 MV over a range of electric fields, F, in the *a*-Se layer from ~1 to ~30 V/μm, and for *a*-Se layer thicknesses d_{Se} between ~10 and ~300 μm. These data are of interest for two reasons: (i) to predict the characteristics of an *a*-Se based imaging device for producing images from megavoltage x-ray beams (e.g. radiation therapy portal imaging[10] or portal dosimetry[11,12]) and hence permit optimization of detector parameters and (ii) to understand better the physics of electron-hole pair generation and recombination in *a*-Se which may suggest methods for improving the x-ray sensitivity of *a*-Se.

The discharge of *a*-Se layers by diagnostic x-ray beams has been measured by a number of investigators.[13] Most used the xeroradiographic discharge curve method in which the potential of the free surface (i.e. the one facing away from the substrate) is measured as a function of exposure. The energy required to produce an electron hole pair, $W_{\pm}$ can be obtained from the slope of the discharge

curve (see section III.A.2). To compare and summarize the data over a range of electric fields, $W_{\pm}$ is often fitted to the empirical formula:

$$W_{\pm} = W'\left(\frac{F}{10}\right)^{-b}, \qquad [1]$$

where F is the electric field in V/μm, W′ is the value of $W_{\pm}$ at 10 V/μm, and b is a constant. The values of W′ and b found by different investigators are variable, but typically, W′≈50±20 eV and b ≈ 0.66±0.15. In most semiconductors, $W_{\pm}$ is independent of incident x-ray energy and most data to date in *a*-Se has been consistent with this interpretation, within the somewhat large variability of the data.

One exception is the results of Fiedler and Laugwitz,[14] who measured $W_{\pm}$ from an effective energy of ~30 keV to 662 keV and found that $W_{\pm}$ decreased monotonically as a function of the incident x-ray energy. Their data along with the range of those of previous investigators is shown in Fig. 1. We felt it was important to verify this measurement and extend it into the radiation therapy range (i.e. > 1 MeV). Thus, we investigated $W_{\pm}$ of *a*-Se using x-ray beams ranging in energy from 40 kVp to 18 MV and in addition, a 17 MeV electron beam.

II. THEORY

A. Background

When x-rays deposit energy in a photoconductor or a semiconductor, electron-hole pairs are created, and provided the material is of high purity (i.e. free of traps) the freed charge carriers can be collected by a modest applied electric field (e.g. 1 V/μm). Klein[15] has shown that for many materials, the

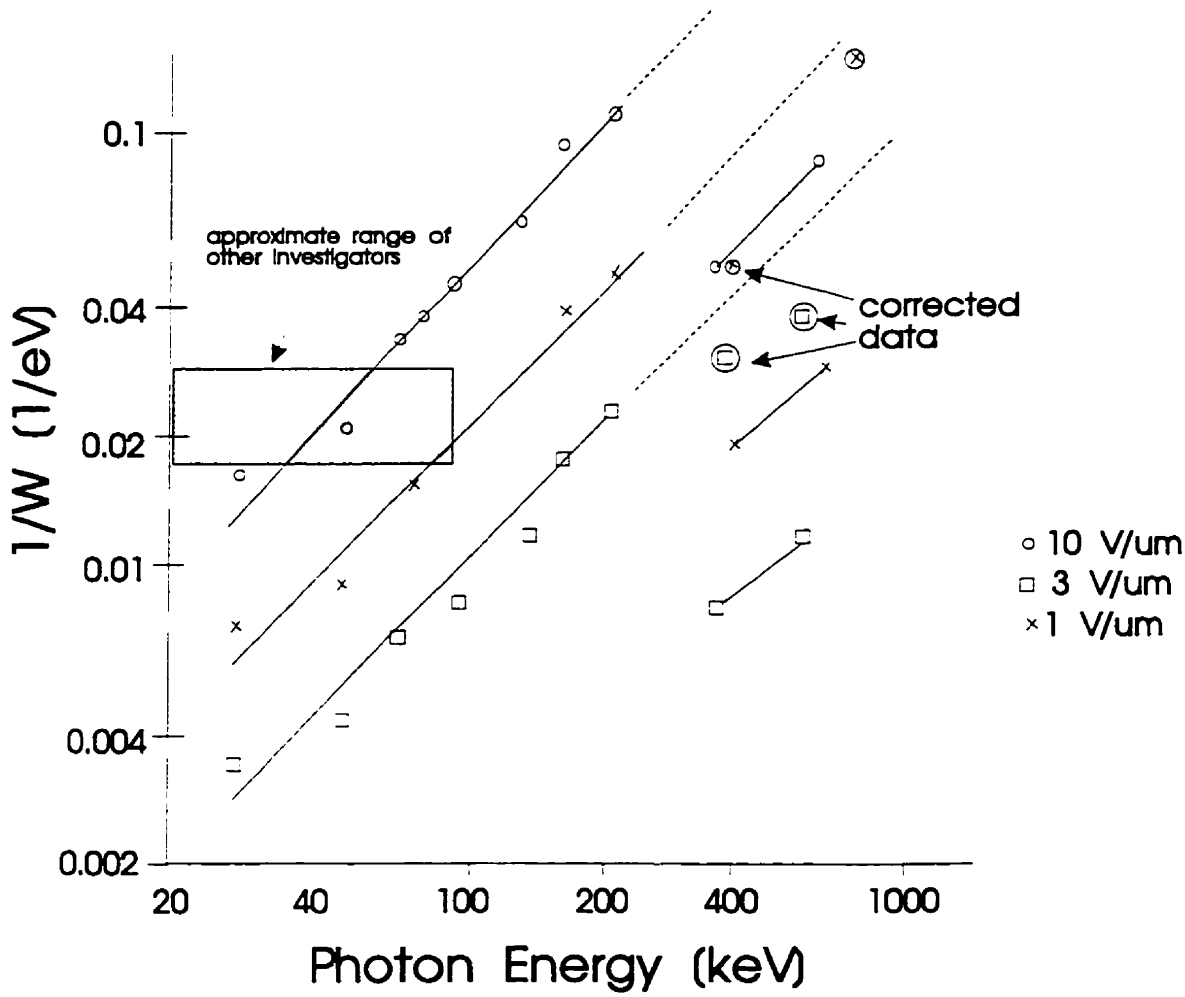

Fig. 1 The experimental results of Fiedler and Laugwitz[14] which show sensitivity ($1/W_{\pm}$) as a function of average photon energy. The discontinuity in the original results may be explained by an error in dosimetry in which the energy attenuated was calculated instead of the energy absorbed. The difference becomes substantial at higher energies where Compton scattered photons carry off a significant fraction of the incident photon energy. Sample corrected data points are shown in as circled data points. Also shown is the range of data from most previous investigators for a field of 10 V/μm (= 10^7 V/m) as compiled by Rowlands *et al.*[13]

amount of energy required to produce an electron-hole pair, is given by the expression

$$W_0 \approx \frac{14}{5}\varepsilon_g + a \ , \qquad [2]$$

where a (≈0.75 eV) is a constant which accounts for energy losses (e.g. phonon production) and ε_g is the width of the forbidden energy gap between the valence and conduction bands. This formula has been shown to hold in a variety of semiconductors[16] and is usually independent of the energy of the radiation used. Application of Klein's formula to *a*-Se (ε_g ~2.2 eV) predicts W_0~7 eV. However, experimental data[13] for *a*-Se indicate a value of $W_\pm >> W_0$. $W_\pm$ is also found to decrease rapidly with increasing electric field, F as shown in Eq. 1. The inequality of W_0 and $W_\pm$ is explicable if it is assumed that in *a*-Se some of the electrons and holes recombine or are trapped. That is, W_0 may be interpreted as the energy required to produce an electron-hole pair in the absence of recombination or trapping effects whereas $W_\pm$ is the measured quantity. Thus, to understand the x-ray sensitivity of *a*-Se, it is of interest to examine the recombination mechanisms which may be acting in *a*-Se.

B. Recombination

When electron-hole pairs are created in *a*-Se by x-rays, they may:

(1) recombine with the other half of the same pair before they are separated (*geminate recombination*),

(2) separate from the pair only to recombine with other electrons or holes in the same electron track (*columnar recombination*; so named because a column of ionization forms around the electron track).

(3) separate, escape from the track only to recombine in the bulk of the *a*-Se with electrons or holes from other tracks (*general recombination*),

(4) separate, escape from the track only to become trapped (*bulk trapping*) or

(5) separate, escape the track and avoid trapping to reach one of the surfaces of the *a*-Se layer. The last mechanism is the one which results in the maximum signal and is the desired one.

Fig. 2 illustrates the first four possible mechanisms that will increase $W_{\pm}$ in *a*-Se.

1. Extra-track loss mechanisms

Trapping of carriers in the bulk is illustrated in Fig. 2(a). The number and depth of traps depend upon the *a*-Se alloy composition, its preparation and history.[17] Since traps limit the carrier range in *a*-Se, their effect on the signal can be established using the optical time-of-flight method.[13,17] These measurements give the schubweg or mean range of carriers (e.g. $S_e = \mu_e \tau_e F$ where τ_e is the mean lifetime of an electron to deep trapping). For our *a*-Se samples, the electron and hole mobilities are $\mu_e = 3 \times 10^{-3}$ cm^2/(Vs) and $\mu_h = 0.12$ cm^2/(Vs) and the carrier lifetimes are $\tau_e = 300$ μs and $\tau_h = 95$ μs.[18] Over the range of fields used, $S_h >> d_{Se}$ so there is no loss of signal due to hole trapping. By comparing the energy dissipated through the displacement currents before trapping to the energy stored in the *a*-Se layer (modelled as a parallel plate capacitor), the fraction of the signal lost from electron trapping can be calculated.[19] If a sufficiently high F is used, then the probability of trapping over the layer thickness can be reduced to negligible proportions. We estimated that if the data for which $d_{Se} > S_e$ is excluded, ~18% of the signal is lost.

Fig. 2(b) illustrates general recombination. It is a bimolecular recombination process* in which separated electrons and holes drifting through the bulk of the *a*-Se collide with one another and

---

** Biomolecular* recombination refers to the situation in which the carriers that recombine are from different molecules (or atoms) whereas *monomolecular* recombination refers to recombination of carriers from the same molecule.

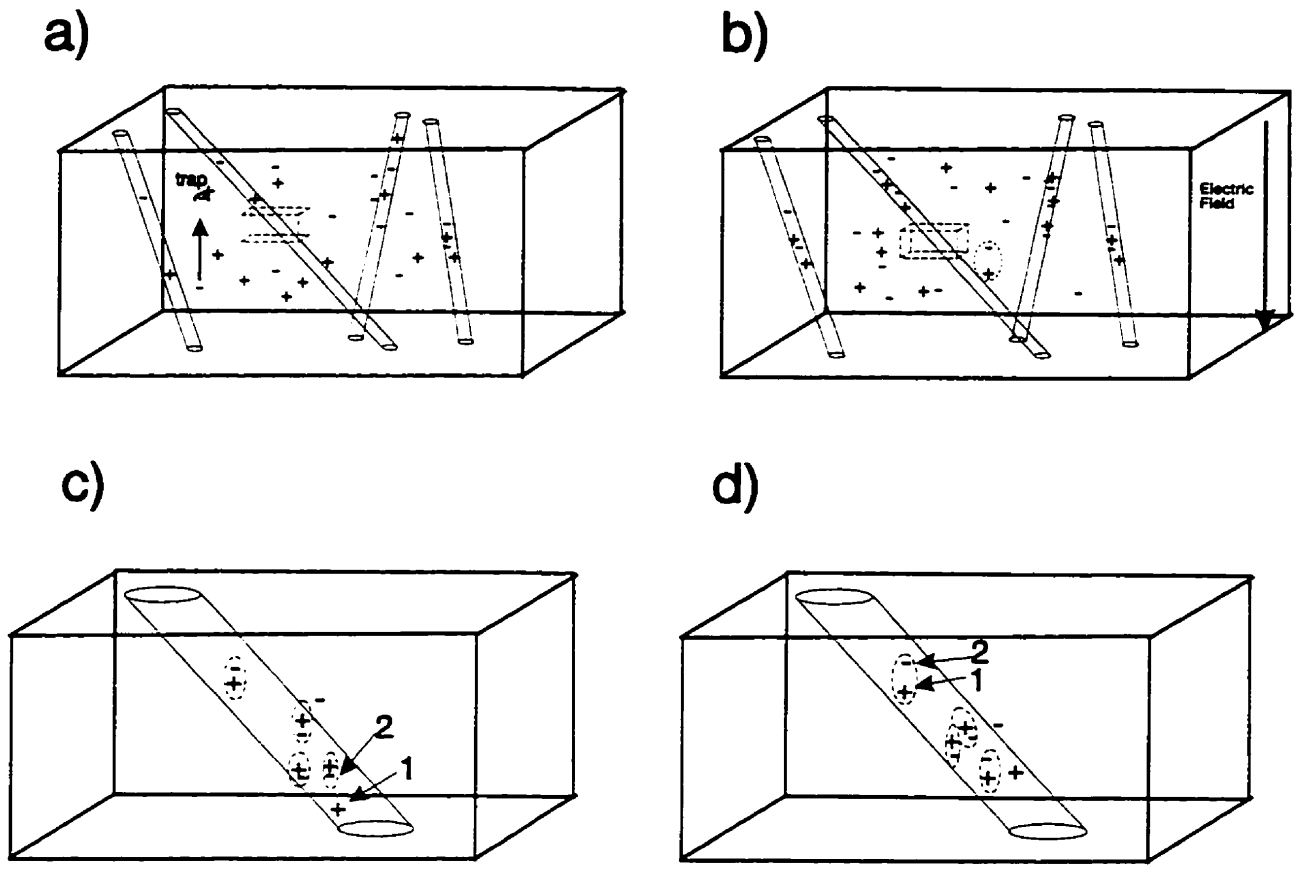

Fig. 2 Illustration of different types of recombination. The cylinders are electron tracks passing through part of the a-Se. a) Trapping: A drifting charge, usually an electron, gets trapped and does not reach the surface. b) General recombination: Electrons and holes drifting in the field away from the tracks, and usually from different tracks, recombine. Both c) and d) are magnified sections of a) and b) illustrated by the dashed boxes. The dotted lines indicate the electron and hole pairs and the numbers 1 and 2 refer to the charges that recombine according to the two different mechanisms. c) Columnar recombination: Electrons and holes from different pairs within the track recombine. d) Geminate recombination: the original electron and hole recombine.

recombine. The amount of general recombination in *a*-Se has been measured and shown[20] to be consistent with Langevin[21] recombination theory. For continuous irradiation, the fraction of charges lost to general recombination, f_r, may determined from the formula[22] for recombination of ions in a parallel plate ionization chamber

$$f_r = \frac{1}{6}\frac{\alpha \dot{\rho}_c d_{Se}^4}{e\mu_e\mu_h V_i^2}, \qquad [3]$$

where $\dot{\rho}_c$ is the rate of electron or hole formation per unit volume, V_i is the surface potential of the *a*-Se plate, e is the fundamental charge, and α is the Langevin recombination coefficient[20] given by $\alpha=e(\mu_e+\mu_h)/(\varepsilon_0\varepsilon_{Se})$ where ε_0 is the permittivity of free space, and ε_{Se} (=6.3) is the relative permittivity of *a*-Se. By estimating W_0 as 7 eV, and the energy absorbed in *a*-Se (see section III.A.1), the amount of general recombination for the x-ray beam qualities used in our measurements could be calculated. Eq. 3 indicates that the amount of general recombination increases linearly with dose rate. It was found that for 1% recombination to occur, the dose rate must exceed ~10^8 cGy/s in a megavoltage beam and ~10^6 cGy/s in a diagnostic beam. By keeping the dose rate well below these levels, the effect of general recombination was kept negligible.

Thus, by suitably choosing the dose rate, layer thickness, and electric field, carrier losses associated with trapping and general recombination can be avoided. However, columnar and geminate recombination occur almost immediately after the energy deposition and need to be explored in greater detail. To quantify the recombination probability from these mechanisms, the photogeneration efficiency, $\eta(F)$, is defined as the fraction of electron-hole pairs that do not recombine; i.e., $\eta(F)=W_0/W_{\pm}(F)$.

2. Intra-track loss mechanisms

Within the ionization column formed by an electron track, two mechanisms compete: columnar and geminate recombination. Geminate recombination as described by Onsager theory was until recently,[23] the undisputed explanation for the electric field and photon energy dependence of optical photogeneration in *a*-Se.[24] Que and Rowlands[30] reviewed existing experimental data and argued that over the diagnostic x-ray range, geminate recombination theory is consistent with existing measured data, but indicated that insufficient experimental evidence exists to completely confirm or refute geminate recombination as the dominant mechanism. Both geminate and columnar mechanisms have been modelled theoretically for x-ray irradiation, but both models have free parameters that are fitted to the experimental data. Thus, neither model is complete. In this section the different theoretical predictions of the two mechanisms are compared as a function of energy and electric field. Later, we will show that neither mechanism alone describes the measured data over the range of electric fields and energies used, but that a microdosimetric explanation based upon both mechanisms is in general agreement with the results.

a. LET dependence

Fig. 2(c) illustrates columnar recombination.[25,26,27] It is a recombination process which occurs within the ionization column as charges diffuse and drift under the influence of the applied electric field from their site of formation. As the linear energy transfer (LET) of the primary electron increases, the charge density within the track increases and thus we predict that the amount of columnar recombination will increase.

An electron and hole are produced when energy deposition results in a transition of an electron from the valence band to the conduction band. The recombination of the electron with its original hole is known as geminate recombination and is illustrated in Fig. 2(d). Since geminate recombination is a monomolecular process, the probability of an electron-hole pair separating is independent of the density of electrons and holes in the surrounding volume. Thus, unlike columnar recombination, geminate recombination is predicted to be independent of the LET of the primary electron.

The LET dependence of either geminate recombination or columnar recombination occurring alone are shown in Fig. 3(a). Examining the LET dependence of $W_{\pm}$ will help to determine which mechanism is dominant. If there is no LET dependence, geminate recombination is the dominant mechanism, but if there is an LET dependence, it would indicate that either columnar alone or a combination of columnar and geminate recombination are occurring.

In Fig. 4(a), the LET (i.e. restricted stopping power) of *a*-Se (Z=34) is plotted as a function of electron energy, E_e. LET varies[28] approximately with Z/A, where Z and A are the atomic number and atomic mass respectively. The LET of *a*-Se was obtained by scaling the published value for copper[28] (Z=29) by the ratio of $(Z/A)_{Se}/(Z/A)_{Cu} = 1.06$. The average LET, for the fluence spectrum of electrons, $(d\Phi_e/dE_e)_P$, generated by a photon spectrum, P, is given by:

$$\langle LET \rangle_P = \frac{\int_0^{\infty} LET(E_e) \left(\frac{d\Phi_e}{dE_e}\right)_P dE_e}{\int_0^{\infty} \left(\frac{d\Phi_e}{dE_e}\right)_P dE_e} . \qquad [4]$$

The Monte Carlo code CYLTRAN[31] was used to calculate $(d\Phi_e/dE_e)_P$ in a representative (50 μm thick) *a*-Se sample for the spectra and buildup materials listed in Table I. To confirm that the <LET> was

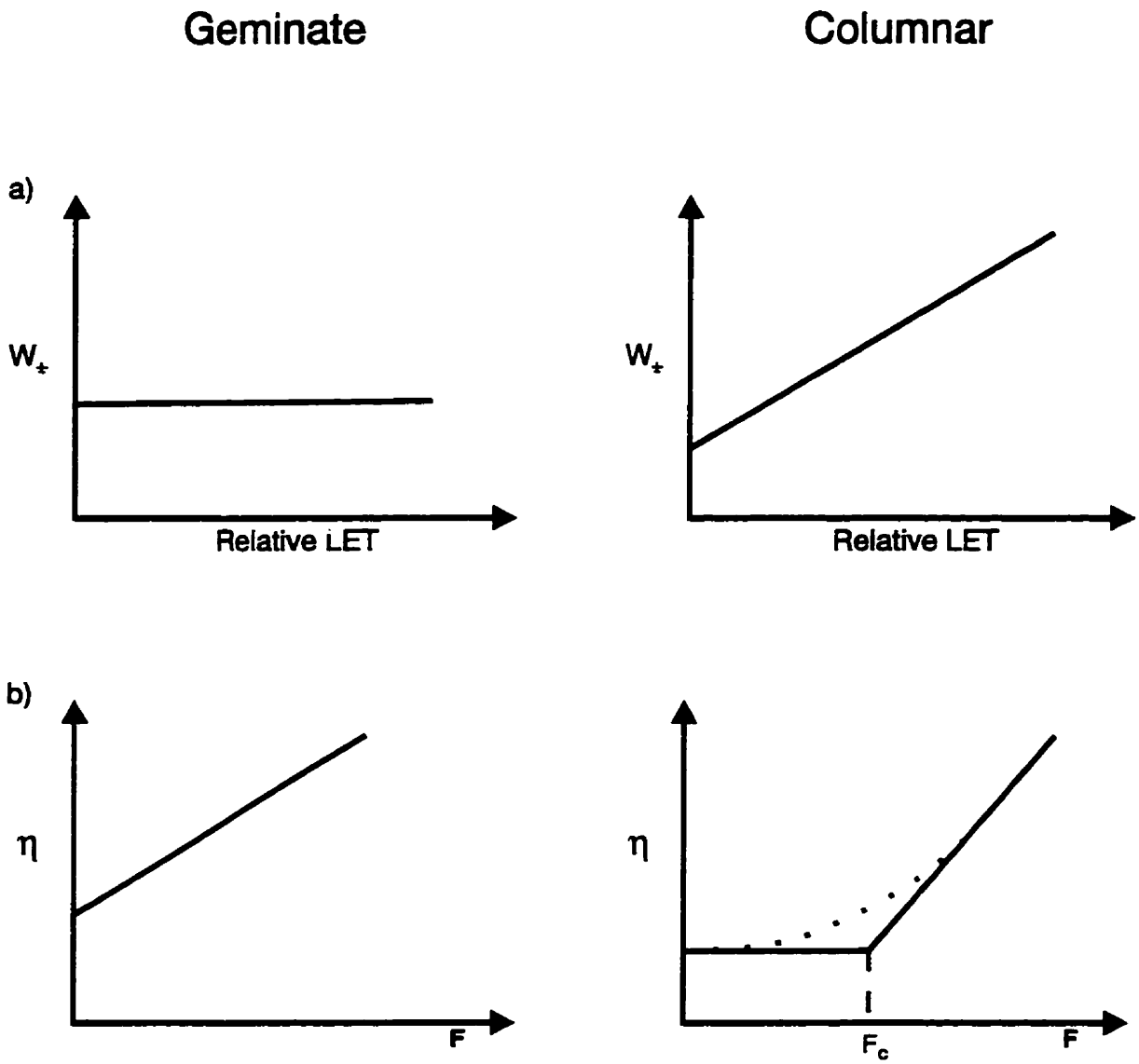

Fig.3 Schematic diagrams showing the differences between geminate and columnar recombination. In (a) W+/- is plotted as a function of LET. Onsager theory predicts no dependence between LET and W+/- while columnar theory predicts an increasing (shown as linear) relationship. In (b) the photogeneration efficiency is plotted as a function of electric field. Onsager theory predicts a linear relationship with a slope to y-intercept ratio of 0.17 um/V. Columnar theory has been calculated for two extremes, one in which the diffusion dominates at low fields and one in which drift is dominant at high fields. The kink in the figure at F_c is not physical, thus a dotted line was added to show a more realistic curve.

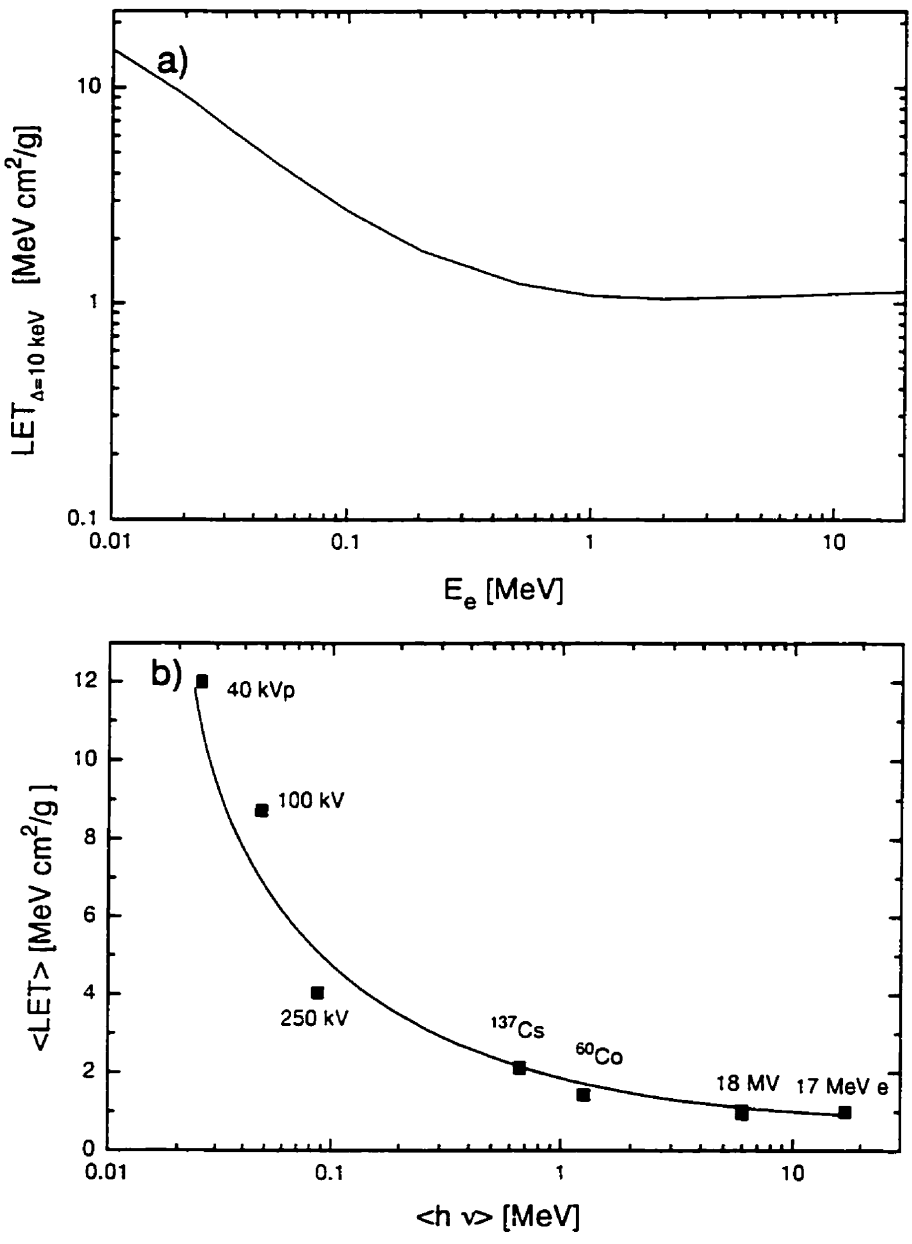

Fig. 4 (a) Linear energy transfer (restricted stopping power) of a-Se as a function of electron energy, E_e. (b) Average LET of the spectrum of electrons generated by x-ray spectra listed in Table I in a 50 μm a-Se layer as a function of the average photon energy of those spectra.

Table I

Beam	Filtration	Source	Buildup Material in addition to 1.1 mm glass	Reference for Spectrum	Reference for Fluence/exposure	Fluence/Exposure [mm^{-2} R]
40 kVp	2 mm Al(nominal)	AECL Therasim 750	-	Tucker[32]	Tucker[32]	$8.37x10^{7}$
70 kVp	2 mm Al(nominal)	AECL Therasim 750	-	HPA[31]	HPA[31]	$1.34x10^{8}$
100 kV	2 mm Al	Philips 100 Superficial Unit	-	HPA[31]	HPA[31]	$1.87x10^{8}$
250 kV	3 mm Cu	Philips 250 Superficial Unit	-	Tucker[32]	Tucker[32]	$2.24x10^{8}$
^{137}Cs	-	-	-	662 keV monoenergetic	Johns and Cunningham[22]	$2.78x10^{7}$
^{60}Co	-	Theratron 780	1.4 mm Glass	Rogers[33]	Johns and Cunningham[22]	$1.63x10^{7}$
18 MV	-	AECL Therac-20	10 mm Al	CYLTRAN	CYLTRAN	$1.26x10^{7}$
17 MeV electrons		AECL Therac 20	1.1 mm Glass + 9 mm Al	17 MeV monoenergetic	ICRU 37[26]	$2.57x10^{5}$

Table I List of x-ray beams, buildup material, filtration, sources, fluence per exposure and sources of data. Since exposure is not defined for photon energies greater than 3 MeV, for these energies the exposure was equated to the air collision kerma. The 18 MV spectrum was calculated at 100 cm from a 3 mm tungsten target in a 1 cm copper case struck by an 18 MeV electron beam and attenuated by a 3 cm lead flattening filter. Good agreement was found between measured and calculated depth dose curves based upon this spectrum.

essentially independent of d_{Se}, the $\langle LET \rangle_P$ of a megavoltage (^{60}Co) beam for d_{Se} of 10 and 300 μm was calculated. The <LET> at d_{Se} =10, 50, and 300 μm were within 10% of each other. Similar independence on d_{Se} was found for a diagnostic (100 kV) spectrum. In Fig. 4(b), the <LET> is plotted as a function of the average photon energy, <hν>, of the spectra listed in Table I. The <LET> and hence the charge density within a column (ρ_c) changes by more than an order of magnitude over the range of photon energies examined experimentally, permitting examination of the LET dependence of $W_{\pm}$ and hence examination of which recombination mechanism dominates.

b. Electric field dependence

Geminate recombination, as described by Onsager theory[29] asserts that the electron-hole pairs are formed in a state whose probability of escaping recombination is dependent upon the initial separation of the electron and hole, r_0. As shown in Fig. 3(b), for $0 \leq F \leq 10$ V/μm, the theory predicts that η increases approximately linearly with **F** and has a slope to ordinate-intercept ratio,[30] R_{SI} given by:

$$R_{SI} = \frac{e^3}{2k^2T^2\varepsilon_0\varepsilon_{Se}}, \qquad [5]$$

where k is the Boltzmann constant and T is the absolute temperature. At T=300 K, R_{SI} = 0.17 μm/V.

As shown in Fig. 3(b), the field dependence of columnar recombination is different from geminate and has been calculated for extreme values of **F**.[27] At low fields, (i.e. much below a critical field, F_c at which drift and diffusion contribute equally), thermal diffusion is the dominant process and consequently, η is independent of **F**. F_c is given by:

$$F_c \approx \frac{kT}{er}, \qquad [6]$$

where r is the radius of the column of ionization. Above F_c, drift of the charges in the field is the dominant process and η varies linearly with F. The value of r in *a*-Se has been estimated[30] to be less than 16 nm which implies that $F_c > 1.6$ V/μm. Thus, examination of the electric field dependence of $\eta(F)$ over the range of $0 \leq F \leq 10$ V/μm may help establish which recombination mechanism is occurring.

III. METHOD

A. Xeroradiographic Discharge- Theory

1. Dosimetry

To determine the dose to the *a*-Se, we measured the exposure and multiplied by the exposure to dose conversion factor which was determined using a Monte Carlo calculation for each beam and d_{Se} used. Table I lists the relevant data required to calculate the energy absorbed in the *a*-Se per incident photon fluence per exposure, E_{abs} as a function of d_{Se} for the different x-ray spectra and the electron beam. Data from the literature where available and the Monte Carlo code CYLTRAN[31] otherwise were used to obtain the photon fluence per exposure. From this, using CYLTRAN, E_{abs} as a function of d_{Se} with the buildup materials listed in Table I was calculated. Typically, one million histories were run to yield E_{abs} to within 3%. The validity of the CYLTRAN code, for thin materials (e.g. 0.1 g/cm^2) at high energies (e.g. 15 MeV), where interface effects are of concern,[32] has previously been established in

a variety of materials (e.g. Be, Au).[33] The resulting values of E_{abs} as a function of d_{Se} for the different x-ray spectra and the electron beam are shown in Fig. 5.

2. Calculation of $W_{\pm}$ from a discharge curve

The characteristic curve of an *a*-Se layer (often called a discharge curve) with a conductive substrate and a free surface can be modelled as a capacitor which is discharged by x-rays. Normally, the free surface is charged positively and when x-rays deposit energy in the bulk of the *a*-Se to form electron-hole pairs, the electrons move to the free surface and the holes to the substrate, both contributing equally to reducing the surface potential, V_i.

If an *a*-Se layer with an initial surface potential of V_0 is irradiated by an x-ray exposure ΔX, $\Delta\sigma_{Se}$ charges per unit area will be released reducing the surface potential to V_1. By measuring $\Delta V_{Se}=V_{i+1}-V_i$, the change in surface charge density $\Delta\sigma_{Se}$ can be obtained from the relation $\Delta\sigma_{Se}=C_{Se}\Delta V_{Se}$ where C_{Se} is the capacitance per unit area given by the parallel plate formula, $C_{Se}=\varepsilon_{Se}\varepsilon_0/d_{Se}$. Since $W_{\pm} = \Delta\sigma_{Se}/(E_{abs}\ \Delta X)$; if the discharge curve (V_i as a function of X) is approximated linearly between the *i*th and *(i+1)*th values of V_i, we obtain for $W_{\pm}$ at a field $F=(V_i+V_{i+1})/(2d_{Se})$ as

$$W_{\pm} = \frac{d_{Se}E_{abs}\Delta X}{\varepsilon_0\varepsilon_{Se}|\Delta V_{Se}|}. \qquad [7]$$

Thus, the value of $W_{\pm}$ can be determined from the slope of the measured discharge curve.

The measured parameters from the different discharge curves can be used to predict the discharge curves for a variety of different conditions. For a small ΔX, there is a small change in σ_{Se} given by

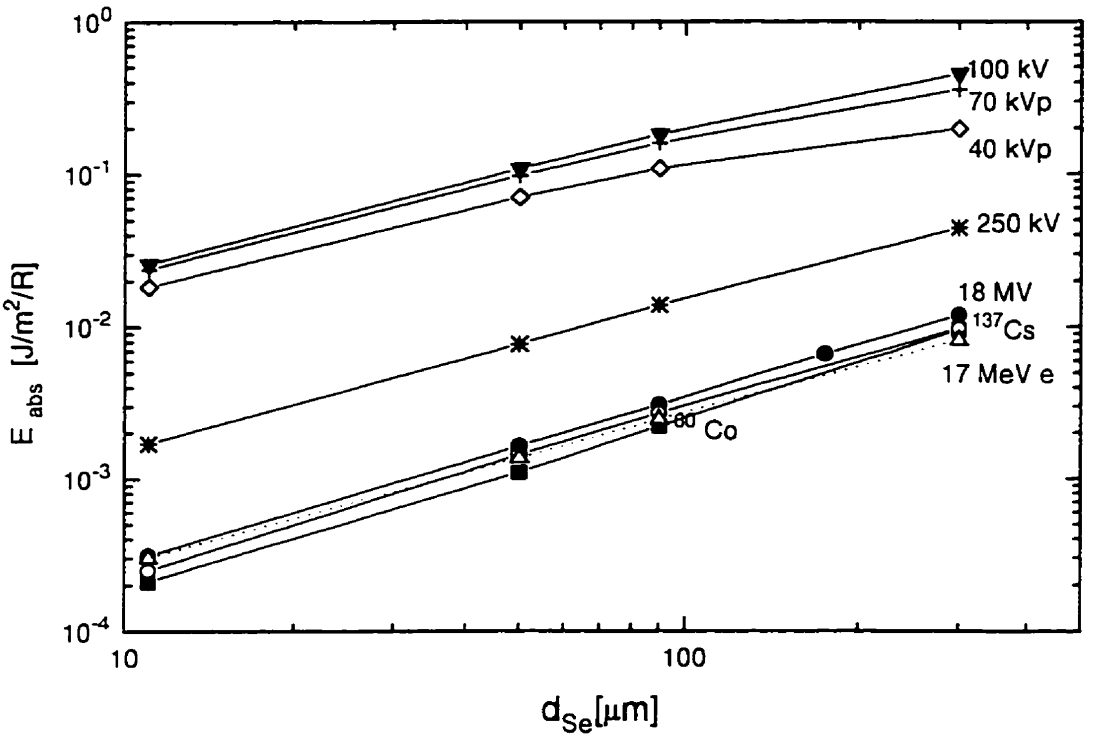

Fig. 5 Energy absorbed per exposure per area , E_{abs}, as a function of d_{Se} for different spectra calculated using the Monte Carlo code, CYLTRAN, for the apparatus shown in Fig. 5. For the 18 MV x-ray and the 17 MeV electron beams, an equivalent exposure was defined as the air kerma divided by W_{air}, the energy required to produce a unit charge in air. The non-linearity in E_{abs} for the diagnostic beams at large d_{Se} is due to attenuation in the a-Se.

the relation $\Delta\sigma_{Se}=(-E_{abs}\Delta Xe/W')\cdot(\sigma_{Se}/10e_0e_{Se})^b$. By integrating this relation, the shape of the discharge curve is obtained from[34]

$$\sigma_{Se}(X)=\left[\sigma_{Se}(0)^{1-b}-\frac{XE_{abs}e(1-b)}{W'(10e_0e_{Se})^b}\right]^{\frac{1}{1-b}}, \qquad [8]$$

where X is the incident exposure and the factor of 10 arises from the normalization field in V/μm for W′ (c.f. Eq. 1).

B. Xeroradiographic Discharge - Experiment

Fig. 6 shows a schematic of the apparatus used to measure the x-ray induced discharge curves of *a*-Se. Samples of *a*-Se (Se + 1-2% As and trace Cl) 5 cm square with thicknesses, d_{Se}, ranging from ~10 to ~300 μm evaporated onto 1.1 mm thick glass substrates coated with ~10 nm of indium tin oxide (ITO) were obtained. A single thin (10 μm) sample evaporated on an aluminum substrate was also used. An electric field was established in the *a*-Se layer by charging the free surface with positive ions from a corotron. The *a*-Se layer was then irradiated with the substrate facing the x-ray beam. This orientation was chosen to provide intimate contact between the *a*-Se layer and the substrate, which for high energy beams acted as the buildup material. It also permitted the vibrating reed electrostatic voltmeter probe[35] to be left in position during irradiation thus minimizing the time between irradiations and the effects of leakage current. For the highest energies, additional aluminum buildup material was added. The different beams are listed with their sources, buildup material and filtration in Table I. The radiation exposure incident upon the *a*-Se layer was measured using a 0.6 cm^3 Baldwin Farmer ionization chamber under full buildup conditions in RMI solid water[36] for high energy (P≥ 662 keV) beams and using a pancake ionization chamber[37] for the diagnostic beams. To compare the

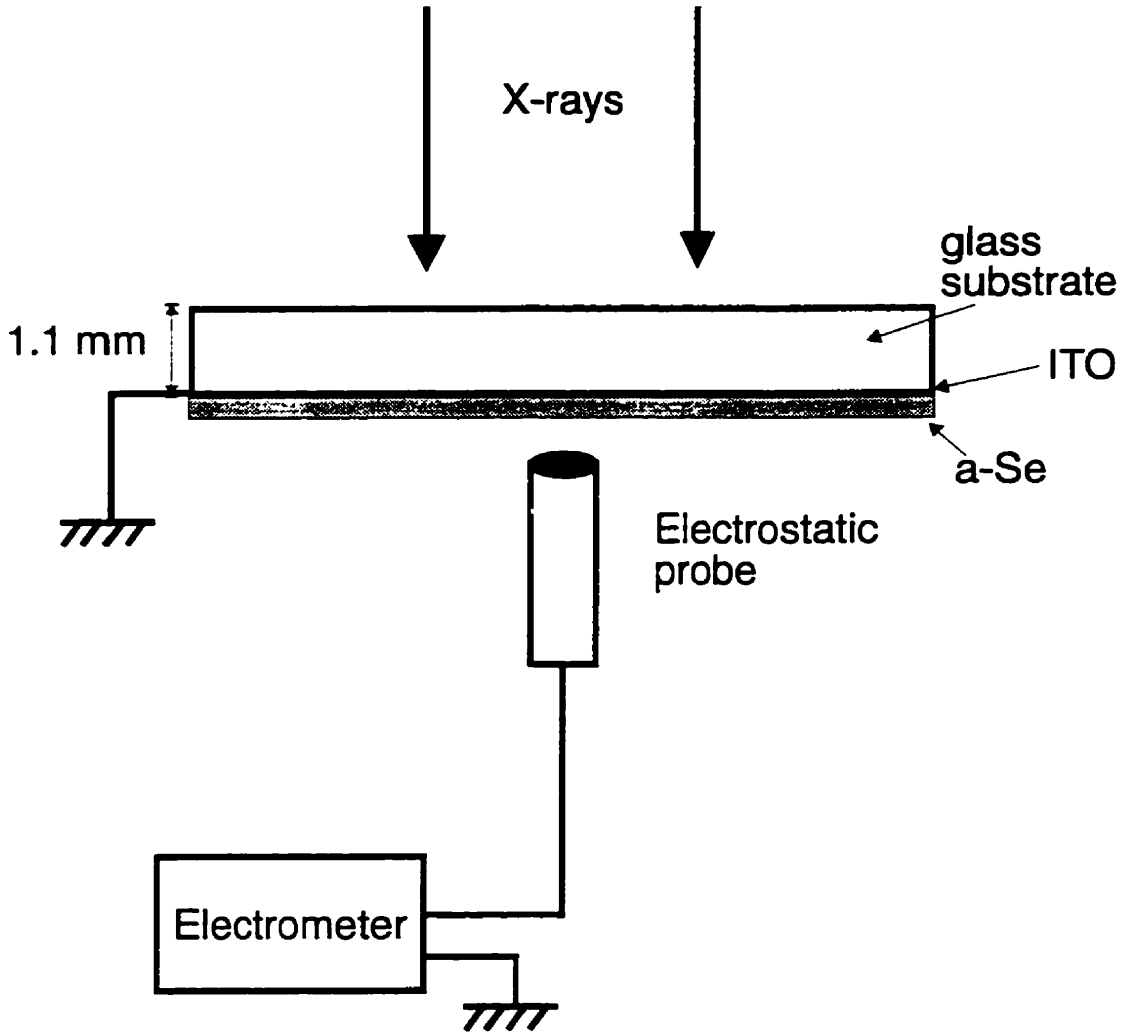

Fig. 6 System used for measuring discharge curve of amorphous selenium samples evaporated on a substrate. The substrate faces the beam and acts as a buildup layer.

dosimeters, we measured the output of the 100 kV tube with both dosimeters simultaneously and found agreement within 1%.

The procedure to obtain the discharge curve was to read the surface potential V_i of the *a*-Se plate with the electrostatic voltmeter, then to irradiate the plate with a small exposure, ΔX, and read the new potential, V_{i+1} from which $\Delta V=V_i-V_{i+1}$ was established. The change in V_i was monitored between radiation intervals to measure the leakage current. For $\mathbf{F} \sim 30$ V/μm, the reduction in V_i between irradiations was ~ 5% of ΔV and much smaller for lower **F**. Thus, the effect of leakage current was negligible. Usually, ΔX was chosen such that the plate was almost completely discharged in ~8 steps. The corresponding irradiation times, Δt, varied between 0.01-0.1 minutes depending upon the quality of the beam and d_{Se}. Typical values of ΔX and Δt are given in Table II.

The effects of three possible systematic errors were evaluated. These were: 1. backscattered radiation, 2. air ionization and 3. effect of radiation on the surface potential electrometer.

1. Backscatter effects

Since the probe was ~1-2 mm away from the free surface of the *a*-Se during irradiation, we investigated if backscattered radiation from the probe affected the readings. Initially, the probe was positioned over the *a*-Se to measure the surface potential. The *a*-Se was then moved away from the probe and irradiated with ΔX. Next, the sample was repositioned under the probe and the new potential was measured. This procedure was repeated to obtain a discharge curve which was compared with that obtained using the procedure previously described. No significant difference was

Table II

Beam	ΔX (R)	Δt(mins)	$E_{abs}(Jm^{-2}R^{-1})$
100 kV	0.03	0.02	0.108
^{60}Co	10	0.1	0.011

Table II Typical values of ΔX, E_{abs} and irradiation times Δt for *a*-Se discharge curves for ^{60}Co and 100 kV beams incident on 50 μm thick *a*-Se. The values of ΔX and ΔT are representative of the diagnostic and radiation therapy sources. For these values, the fraction of electron-hole pairs that escape general recombination f_{∞} is >0.999. The initial surface potential was ~ 1000 V and the range of ΔV was 20-100 V.

found either at 100 kV or ^{60}Co thus demonstrating that backscatter from the probe was not affecting our results.

2. Air ionization effects

We investigated the possibility that ions being formed in the air adjacent to the surface of the *a*-Se layer contributed to its discharge. A 1 mm thick aluminum plate was suspended ~ 1 mm above the 10 μm *a*-Se samples, and +1000 V was applied between the metal plate and the *a*-Se. (N.B. The ITO was grounded as shown in Fig. 6.) The procedure was repeated with the plate grounded and with −1000 V applied. At +1000 V on the plate, all the positive air ions formed would be forced into the positively charged *a*-Se, whereas at −1000 V, the negative air ions would be forced into the *a*-Se. No change was found in the discharge curve of the *a*-Se over this range of applied potentials and beams (i.e. 100 kV and ^{60}Co) demonstrating that ionization in the air did not affect any of the discharge curve measurements.

3. Effect of Radiation on Electrometer

There was some signal generated by direct interaction of radiation in the electrostatic voltmeter probe. However, after the irradiation ceased, the readings settled within seconds. Since the probe was not in the beam for the backscatter measurements described above, and since no difference was found in the discharge curves, waiting a few seconds after irradiation before each measurement avoided any effects that the radiation had on the electrometer.

IV. EXPERIMENTAL RESULTS

Discharge curves were obtained over the range of energies 40 kVp to 18 MV and for d_{Se} between 10 and 300 μm. For each d_{Se} and energy, several (1 to 3) discharge curves were obtained. Eq. 7 was used to calculate $W_{\pm}$ as a function of F for each curve. In Figs. 7 (a) and (b), $W_{\pm}$ is plotted as a function of F for 100 kV and ^{60}Co beams over a range of d_{Se} and for two different substrates. Straight lines were least squares fit to the each of the discharge curves and the resulting fitting parameters were averaged to obtain a representative line. Although there appears to be a thickness dependence in examining the ^{60}Co data of Fig. 7(b), further examination of all samples over the range of energies and d_{Se}, showed no monotonic dependence of $W_{\pm}$ on d_{Se}. There was no significant difference in the discharge of the *a*-Se between an aluminum substrate and a glass substrate indicating that light (e.g. from fluorescence or Čerenkov radiation) generated in the glass did not contribute significantly to the measured $W_{\pm}$.

There was a significant reduction in $W_{\pm}$ as the x-ray energy increased. At the normal operating field for *a*-Se (10 V/μm), the value of $W_{\pm}$ for a 100 kV beam is ~51 eV but decreased to ~17 eV for a ^{60}Co beam. In Fig. 7(c), the least squares fitted lines of all the different x-ray beams are shown. There are two distinct regions, one below 100 kV and one above 662 keV with a transition at 250 kV. A list of the fitting parameters for b and W′ in Eq. 1 for the different photon spectra is given in Table III.

Fig. 8 shows typical examples of $\eta=(W_{\pm}/W_0)$ over the range of $0 \le F \le 10$ V/μm along with linear fits and the predicted lines chosen by Que and Rowlands[30] from geminate (Onsager) theory for r_0=4 nm and r_0=2 nm where r_0 is a model parameter describing the initial separation of the electron and hole.

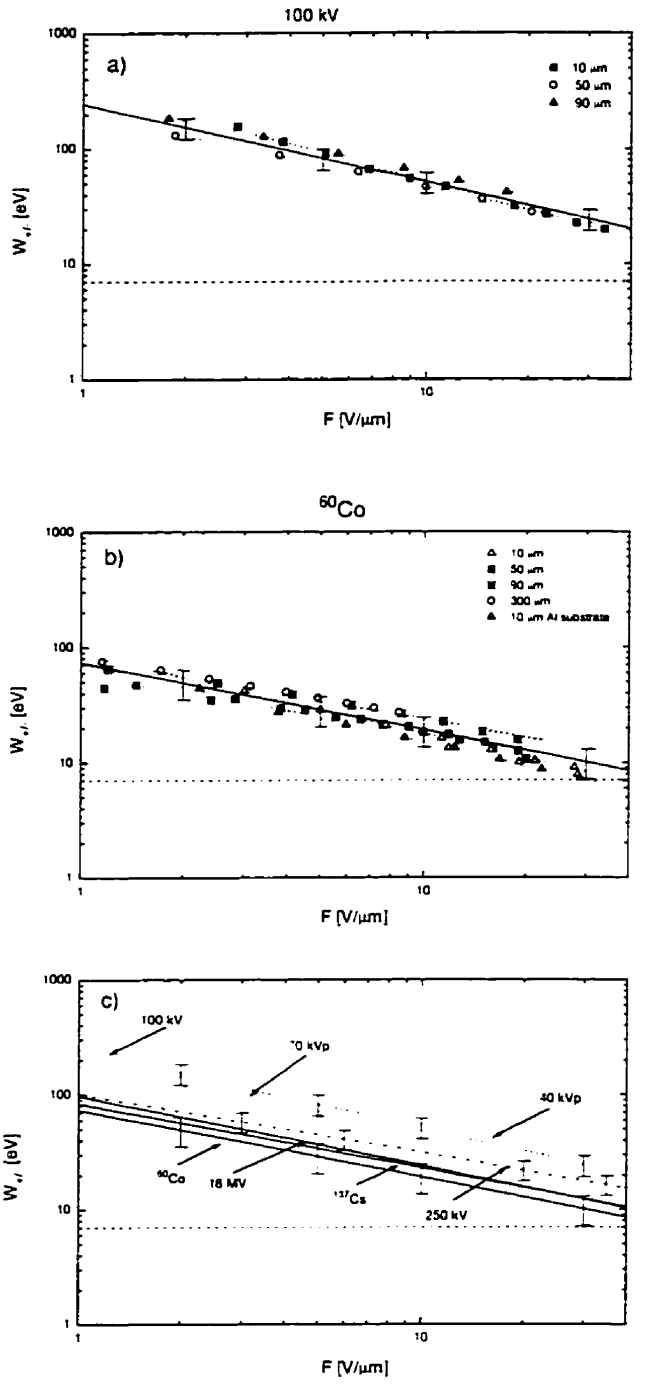

Fig. 7 Plot of energy required to produce an electron hole pair, $W_{+/-}$, as a function of electric field, **F**, for (a) a 100 kV beam and (b) a ^{60}Co beam. The individual data sets are fitted with straight dotted lines and these lines are averaged obtain the solid line. The error bars indicate the uncertainty for the solid lines at selected fields resulting from the variations in the fitting parameters of the individual dotted lines. (c) The averaged lines for all the beams listed in Table I. Also shown on all the graphs as a horizontal dotted line is W_0 as predicted by Klein's formula. The error bars are for 100 kVp, 250 kVp and ^{60}Co beams.

Table III

Beam	W′	b	R_{SI} (μm/V)
40 kVp	54.7±2.4	0.60±0.03	0.49±0.14
70 kVp	47.9±6.6	0.57±0.08	0.49±0.1
100 kV	51.2±5.3	0.68±0.05	0.47±0.2
250 kV	31.2±3.5	0.52±0.06	0.23±0.05
^{137}Cs	23.0±4.6	0.56±0.12	0.21±0.08
^{60}Co	18.6±2.2	0.57±0.08	0.22±0.1
18 MV	24.0±3.5	0.61±0.07	0.22±0.05
17 MeV e	23.9±7.1	0.57±0.07	-

Table III Fitting parameters for exponential fits for $W_{\pm}$ as a function of **F** (in V/μm). Example graphs are shown in Fig. 7. Also shown are the values of R_{SI} for each of the beams (example graphs in Fig. 8). The errors for were calculated by fitting a line to the data from individual discharge curves and averaging the fitted parameters. The errors are standard errors of the mean.

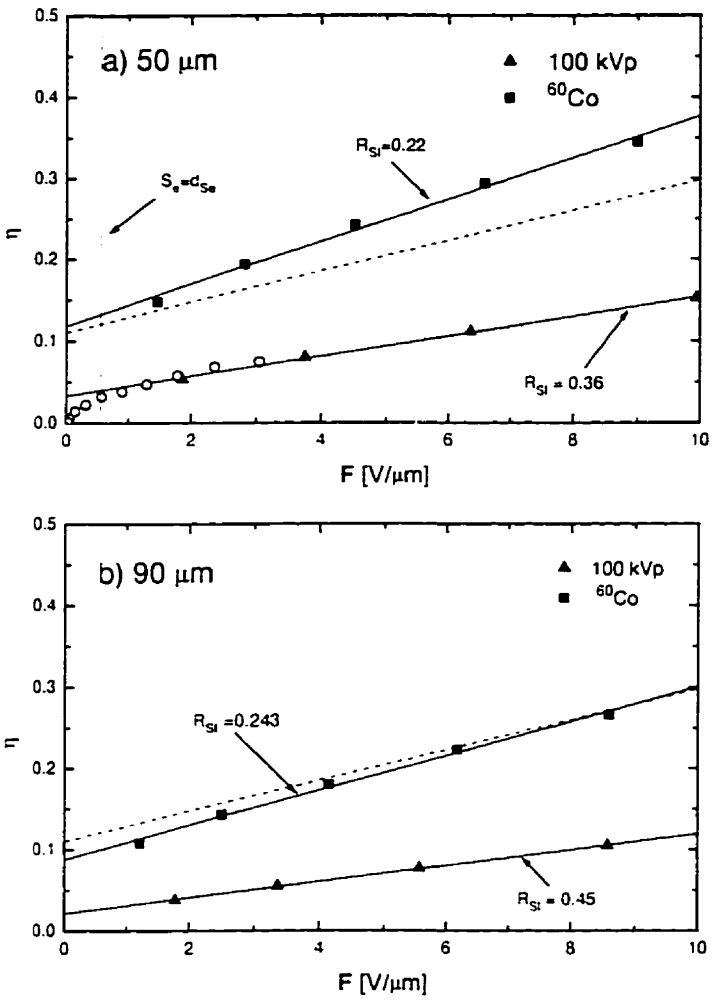

Fig. 8 Typical examples of photogeneration efficiency, η as a function of electric field, **F**, for two x-ray energies and a-Se samples of thickness (a) 50 μm and (b) 90 μm. In (a), the data from a more sensitive low potential probe (i.e. Trek model 320B) are also shown as open circles. The deviation from linearity occurs at approximately the point where $d_{Se} = S_e$, shown by the vertical line, indicating that the deviation from linearity is occuring due to trapping of electrons at lower fields. The dashed and dotted lines are the predicted values from Onsager theory for r_0 = 4 nm, and r_0=2 nm respectively at T = 300 K.

The data in Fig. 8 are the same as that shown in Fig. 7 for the d_{Se} indicated; however, the data points are from a single discharge curve. The R_{SI} was determined from each curve and the averaged values are summarized in Table III for all beams. Data were also obtained from the literature and replotted as $\eta(F)$ over the range $0 \leq F \leq 10$ V/μm. The curves were linear and the corresponding R_{SI} are listed in Table IV.

V. DISCUSSION

A. Columnar recombination

We found that $W_{\pm}$ has a weak energy dependence that is difficult to establish over a small energy range, such as the diagnostic range, but readily measurable over the larger energy range (40 kVp to 18 MV) used here. Table IV lists the values of W′ and b obtained by previous investigators who used beams with spectra (P) ≤ 100kVp. Our data falls within the range of that of previous investigators. Our data shows that $W_{\pm}$ decreases with increasing energy, consistent with the observations of Fiedler and Laugwitz[14] but our values of $W_{\pm}$ do not change as rapidly as theirs. Specifically, at F= 10 V/μm, they found that $1/W_{\pm}$ increased linearly as a function of average photon energy with a slope of 4.6×10^{-4}. By fitting our data in a similar fashion (over the range ~25 to 1000 keV) the slope was found to be $\sim 3 \times 10^{-5}$, more than an order of magnitude smaller. Part of the explanation for this discrepancy may be due to the fact that Fiedler and Laugwitz based their calculation of E_{abs} on an approximate method, an equivalent monoenergetic photon - rather than a complete spectrum. We attempted to recalculate $W_{\pm}$ by our method, but the differences between their slope and ours could not be accounted for by dosimetry alone, suggesting that other factors such as sample differences or experimental techniques may be contributing.

Table IV

Publication	Beam	W′	b	R_{SI}(μm/V)
Donovan[48] (photocurrent)	50-70 kVp	30	0.66	1.85
Donovan[48]	50-70 kVp	43	0.5	0.46
Borasi[49] (d_{Se}=48μm)	50-70 kVp	32	0.55	1.12
Borasi[49] (d_{Se}=157μm)	50-70 kVp	36	0.56	0.35
Rowlands[13] (pulse height)	k fluorescence	54	0.8	0.81
Fiedler[14]	43 keV	54	0.67	1.05
Fender[50]	30-120 kVp	51	-	-

Table IV Typical values of W′ and b from Eq. 1 from the literature for a variety of beam energies. Also shown is the R_{SI} obtained by replotting the data over the range of 0 to 10 V/μm. The variations between the data may be due to differences in selenium preparation and measurement techniques. The data for Fiedler was calculated at 43 keV (≈60 kVp) following Rowlands et al.[13] In addition, we only took the fitted data from the literature and not the raw data. This may also contribute a small error.

Fig. 7 shows that at the highest fields (~ 30 V/μm) and energies available to us, $W_{\pm}$ approaches the theoretical value of W_0 (~7 eV) suggesting that recombination has been completely eliminated. It would be of great interest to extend these measurements to even higher fields to confirm saturation. The difference in $W_{\pm}$ between high and low energies shows that there is an LET dependence, which indicates the presence of columnar recombination. This data suggests that a field of 30 V/μm is sufficient to eliminate geminate recombination, but that columnar recombination is important at diagnostic energies.

Fig. 9 shows the value of W′ as a function of <LET> obtained using the data listed in Fig. 4(b) and Table III. Although the data in Fig. 9 are at a field of 10 V/μm, they are representative of the results over the range of measured fields (cf. Fig. 7(c)). There is a monotonic increase in W′ with increasing <LET> indicating the presence of columnar recombination (cf. Fig. 3(b)).

B. Geminate Recombination

Comparing the measurement of η as a function of F (Fig. 8) with Fig. 3(a), the data is linear (i.e. there is no change in slope) which supports geminate rather than columnar recombination as the dominant mechanism. If columnar recombination was dominant, there would be a change in slope at F_c (N.B. F_c is estimated to range from 1.25 to 3.9 V/μm with mean of 2.5 V/μm in *a*-Se; see section V.A). The plots of η(F) are linear for our data. In general, the data of previous investigators also fit linearly, although occasionally, the slope of the curve decreased with increasing F (i.e. in the opposite direction predicted by columnar recombination and likely due to trapping; cf. Fig. 8). Onsager theory also predicts that R_{SI} = 0.17 μm/V and no LET dependence of $W_{\pm}$. Tables III and IV show that for high energies (i.e. P≥ 662 keV), R_{SI} ~0.2 μm/V in approximate agreement with Onsager theory, but

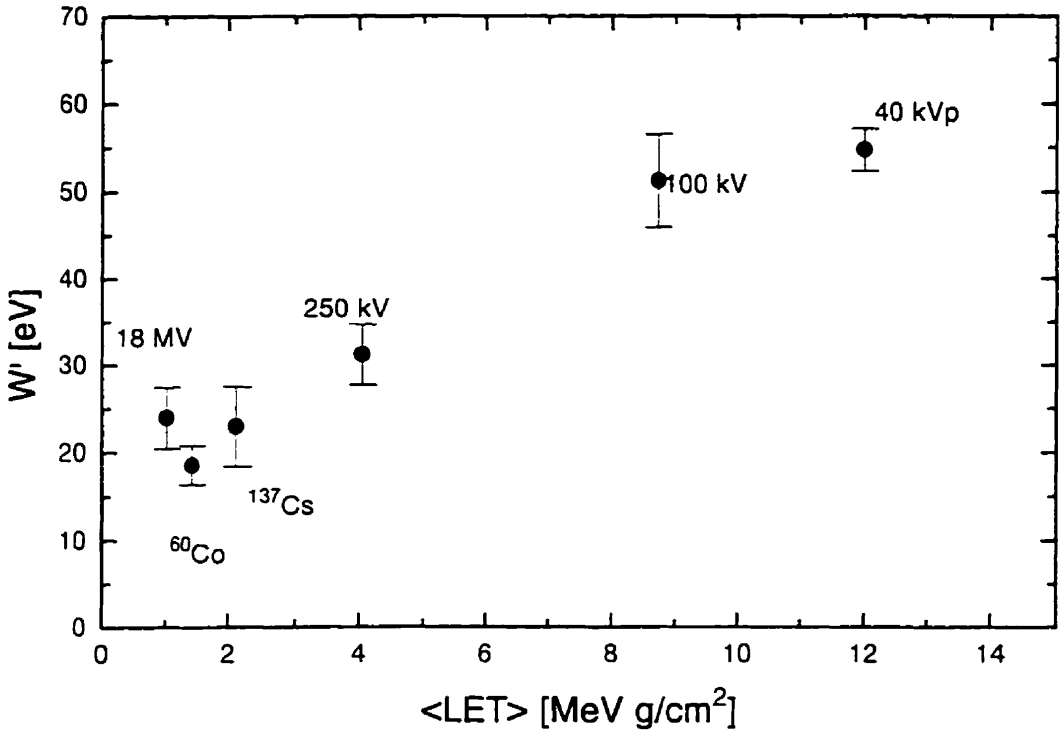

Fig. 9 W' as a function of <LET> for x-ray beams from 40 kVp to 18 MV at **F**=10 V/μm. The W' data was taken from Table III and the <LET> was calculated using CYLTRAN and Eq. 4.

for lower energies, R_{SI} is much greater than 0.17 μm/V. This result and the LET dependence of $W_{\pm}$ indicates geminate recombination is the dominant mechanism at high energies, but both mechanisms are present at low energies. We can further examine this interpretation of the data by considering a microdosimetric mechanism in which recombination changes as a function of LET.

C. Microdosimetric mechanism

On a microscopic level, electrons interact in discrete collisions resulting in distinct energy deposition events. A model which describes the size and energy dependence of such transfers has been developed in radiation chemistry. The basic concept[38,39] is shown in Fig. 10, where energy deposition events known as *spurs* are illustrated as *beads on a string*. Spur theory has been developed primarily for chemical reactions in water, but has also been used to describe recombination in *a*-Se.[25] Spurs are considered to be regions in which a few electron hole pairs are localized and result from glancing collisions between the high energy electrons and orbital electrons. In the simplest version of the model, spurs are assumed to have a fixed amount of energy, δ; be spherically shaped with radius r; and uniformly spaced by distance U. Since δ is fixed, as the LET increases, the spurs move closer together until they form a column and as they overlap, the additional bimolecular recombination between the electrons and holes from different spurs increases $W_{\pm}$. Thus by examining this model and using it to determine the <LET> at which columns form, a more quantitative, microscopically based test of our qualitative analysis of the <LET> dependence can be made.

A spur consists of a charge cloud which forms as a result of an energy deposition event. Estimates of the size of the spurs has only been studied in detail for the cause in which diffusion is dominant.

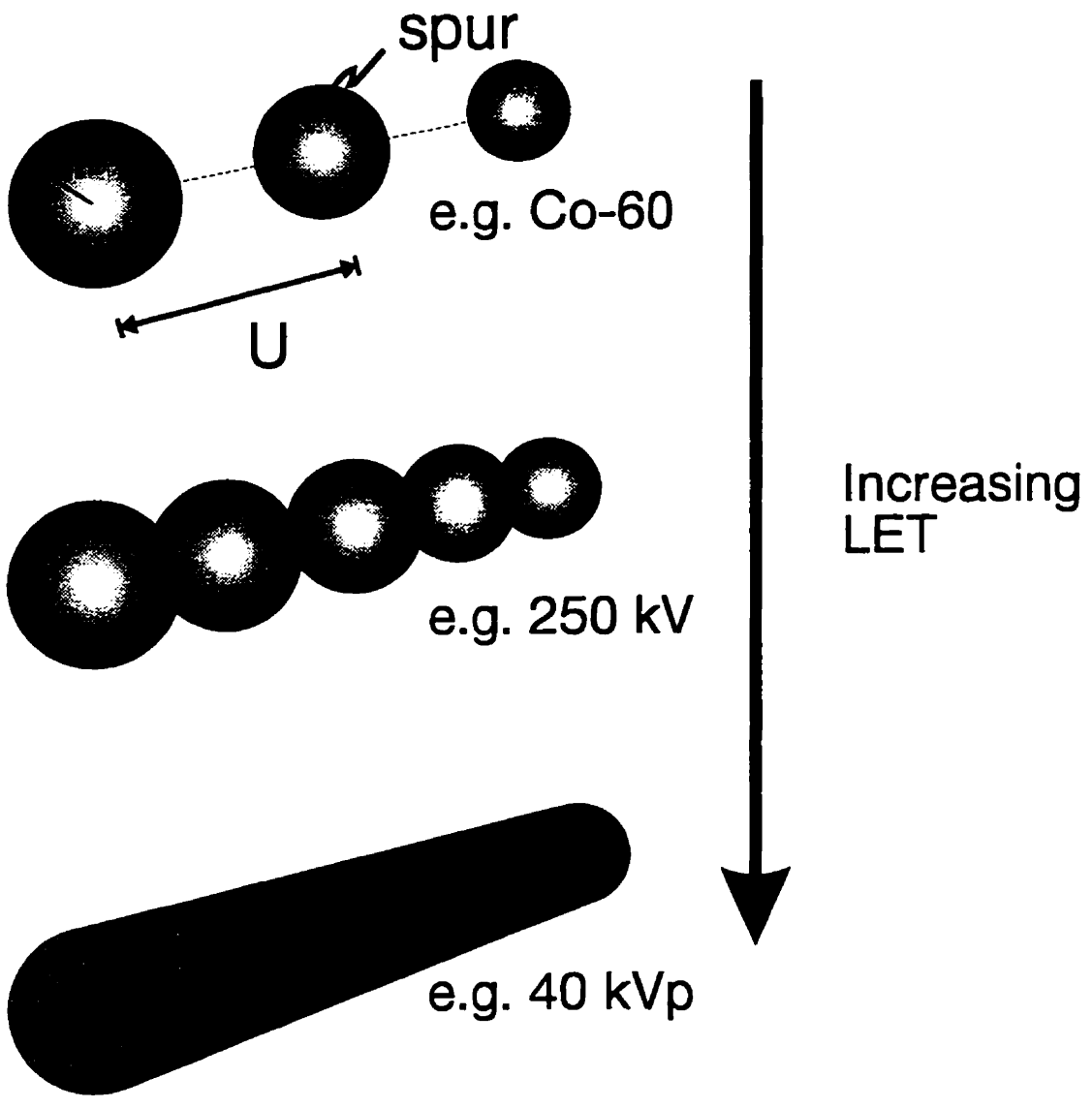

Fig. 10 Illustration of concept of a spur. Spurs have an energy δ, a radius, r and are separated by a distance, U. As the LET increases, the spurs come closer together until they overlap and form a column.

This model therefore describes the low field case. Since spurs result from the inelastic collision of a fast electron with an orbital electron, the largest cross sections for these interactions will occur at the resonance energies for the electron shells (< 100 eV). The average energy deposition per inelastic scattering event in *a*-Se has been estimated[40] to lie between 40 to 80 eV, depending upon the electron energy. Others[25] have estimated δ to be ~ 20 eV in *a*-Se. After the energy is deposited, the electrons and holes diffuse and drift outward. The spherical charge cloud resulting from the energy deposition is assumed to begin at a point and diffuse outward with a Gaussian profile of the form $\exp(-r^2/\sigma^2)$ where r is the spur radius and $\sigma^2 = 4Dt_s$. The diffusion constant is given by the relationship[41] $D=\mu kT/e$ where $\mu \approx \mu_h$ since $\mu_h >> \mu_e$. We assume the time for spur formation, t_s, is approximately 10^{-10} s following the estimates of others[42,43] but caution that values ranging from 10^{-11}s to 10^{-9} s have been proposed.[44,45] Based upon these estimates, the spur radius $r = (4Dt_s)^{1/2} \sim 11$ (range 4 to 31) nm.

The spur separation, U, can be obtained by fitting the values of U, r and δ to the LET. Specifically, since the LET is the density of the energy deposition, this implies (see Fig. 10) that $LET=\delta/U$ or

$$U(E_e) = \frac{\delta}{LET(E_e)} . \qquad [9]$$

The spurs will begin to overlap when U = 2r. Using Eq. 9 and the data in Fig. 4, assuming r=11 nm and δ=40 eV, the spurs will begin to overlap at an LET of ~ 4 MeV cm^2/g which approximately corresponds to the $\langle LET \rangle_{250kV}$ (N.B. density of *a*-Se = 4.26 g/cm^3). This suggests that $W_{\pm}$ is small at high energies (P≥662 keV) because the spurs are separated and no recombination occurs between them. This is further illustrated in Fig. 11 where the data of Fig. 9 are replotted in a more intuitive form of sensitivity as a function of photon energy. At high energies, the spur theory predicts that the sensitivity is approximately constant, in agreement with the Fig. 11. At low energies, the spurs form

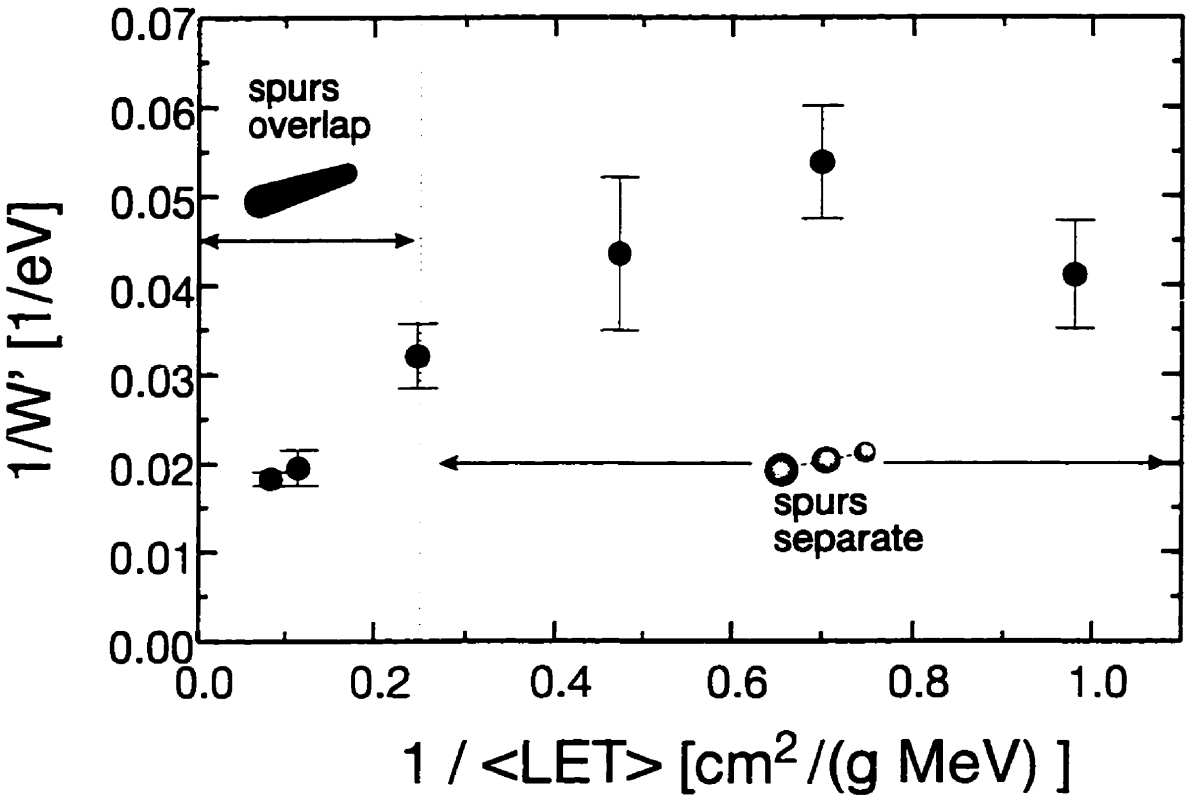

Fig. 11 Plot of sensitivity (1/W') as a function of increasing energy (1/<LET>). This data is the same as that shown in Fig. 9. The vertical line corresponds to the estimated energy at which the spurs begin to overlap.

a column, additional recombination occurs, raising $W_{\pm}$ in agreement with our observations. Therefore the energy dependence of $W_{\pm}$ is, to a first approximation, consistent with the spur mechanism.

To summarize, our results suggest that at high electron energies the spurs are separated and that the recombination within them is described by Onsager theory. As the electron energy decreases, and the spurs overlap, the additional recombination between the spurs increases $W_{\pm}$ in a way not described by either theory alone. This additional recombination also changes the values of R_{SI} at lower energies. Clearly, the proposed mechanism is only a first order approximation. In particular, the uncertainties in t_s and δ give a large range of possible spur sizes and spacing which could readily vary by a factor of two. Additional measurements of $W_{\pm}$ at very high LET over a range of fields and further theoretical development of a model are desirable.

D. Dynamic Range Implications for Portal Imaging

What are the implications of these results for portal imaging ? We can make some specific comments about the signal size, dynamic range requirements and implications of different readout approaches. There are two types of readout approaches: (i) those that have a surface electrode which maintains a constant electric field across the *a*-Se (e.g. an active matrix readout[4,5]) and (ii) those that can only be used once per daily treatment fraction in which there is a free surface which is discharged by the x-rays (e.g. using a scanning electrometer readout[46]). In both types of readout, the minimum exposure required to produce a quantum noise limited system is determined by the system noise. The maximum exposure for both systems depends upon the pixel capacitance. For the electroded system, this capacitance can be augmented as necessary. On the other hand, for free surface readout systems, only the inherent capacitance of the *a*-Se is present and may well limit dynamic range. Fortunately, the

signal and capacitance depend differently on the *a*-Se layer thickness (d_{Se}) and thus can be adjusted to modify the dynamic range.

The dynamic range of a free surface readout system can be calculated from our data. An *a*-Se based portal imaging system should be able to produce both (i) localization images in which the detector is exposed to a small fraction (e.g. 1%) of the daily radiation fraction (~200 cGy) and (ii) verification images in which the imager is irradiated throughout the total treatment. Thus, the air kerma incident on a patient to produce an image could be ~1-200 cGy. Assuming a 50% attenuation in the patient, the appropriate incident air kerma range that the detector should operate over is 0.5-100 cGy. In Fig. 12, the charge signal, $\Delta\sigma_{Se}$ and the voltage signal, ΔV_{Se} are shown for the same initial field of 20 V/μm, the maximum field for the thinner samples. The curves in Fig. 12 were calculated using Eq. 8. The values of b and E_{abs} were taken from Table III and Fig. 5 respectively. For either of the two possible signals to be read out: charge or surface potential, Figs. 12(a) and (b) indicate d_{Se} should be between 5 and 20 μm to cover the exposure range of interest. Thicker *a*-Se may also be used, but only for localization images. Thus for free surface readouts, *a*-Se detectors may be used like film, with different *a*-Se layer thicknesses being used for localization and verification images.

VI. CONCLUSIONS

The xeroradiographic discharge method has been used to measure the sensitivity of *a*-Se to x-rays ranging in energy between 40 kVp and 18 MV and for samples thicknesses between 10 and 300 μm. Provided the electric field was sufficiently high to collect all the released electrons and holes, the average energy required to release an electron-hole pair, $W_{\pm}$, was found to be essentially independent of the *a*-Se thickness. However, although the energy dependence was weak, over a large photon

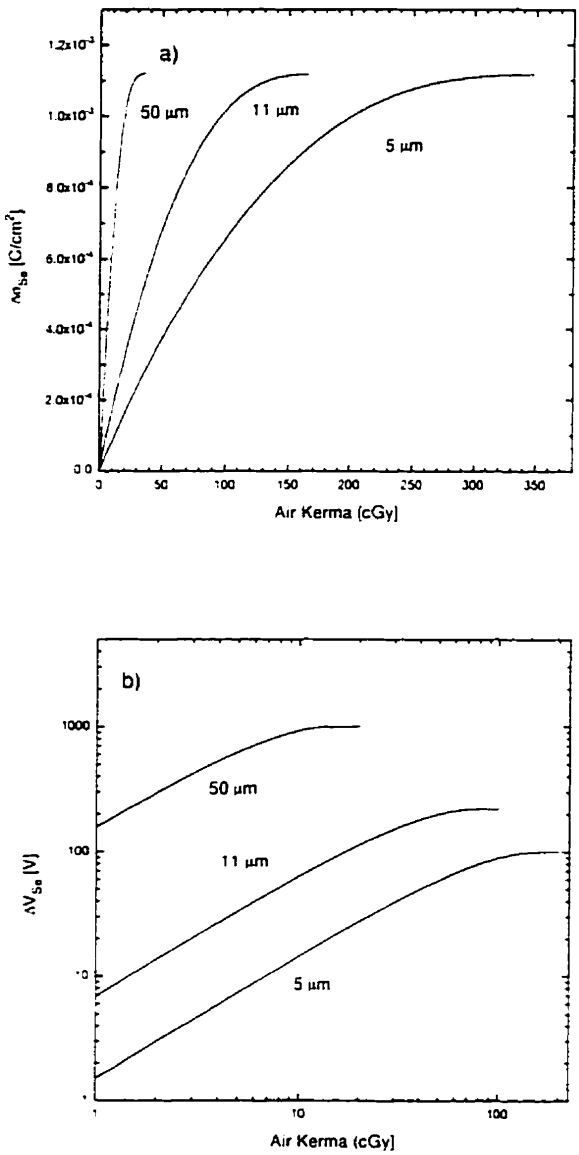

Fig. 12 Signal size for a-Se plates discharged by a ^{60}Co beam for different values of d_{Se}. A constant initial field of 20 V/µm is assumed. The data apply to full buildup of glass. In (a) the charge signal is shown and in (b) the voltage signal is shown.

energy range (40 kVp to 18 MV), $W_{\pm}$ decreased by a factor of nearly three. At megavoltage energies and at the highest fields (~30 V/μm), $W_{\pm}$ approached 7 eV, the limit predicted by Klein's empirical relationship, implying that all recombination was eliminated. Further investigation at higher fields is warranted to confirm saturation.

We compared our measurements to theoretical prediction to distinguish between geminate and columnar recombination. Since the recombination was found to be LET dependent, this implied that over the measured energy range, columnar recombination made a contribution. However, the field dependence of the recombination at high energies (low LET) was consistent with the predictions of Onsager theory suggesting that at low LET, geminate recombination is dominant. A microdosimetric model showed indicated that it was reasonable to believe that geminate recombination occurs within the discrete energy deposition events (spurs) but as the LET decreases, these spurs move closer together and the columnar recombination contributes.

Finally, we used our data to show that for readout systems that for a free surface, a 5-20 μm layer of *a*-Se is required to produce a verification image, but thicker layers may be used if localization images are required.

REFERENCES

1. J.W. Boag, "Xeroradiography." *Phys. Med. Biol.*, **18**, 3-37 (1973).

2. W. Hillen, S. Rupp, U. Schiebel, and T. Zaengel, "Imaging performance of a selenium-based detector for high-resolution radiography," *Proc. SPIE*, **1090**, 296-305 (1989).

3. J.A. Rowlands, D. M. Hunter and N. Araj, "X-ray imaging using amorphous selenium: A photoinduced discharge readout method for digital mammography," *Med. Phys.* **18**, 421-431 (1991).

4. D.L. Lee, L.K. Cheung, and L.S. Jeromin, "A new digital detector for projection radiography," *Proc. SPIE*, **2432**, 237-249 (1995).

5. W. Zhao and J.A. Rowlands, " X-ray imaging using amorphous selenium: Feasibility of a flat panel self-scanned detector for digital radiology," *Med. Phys.*, **22**, 1595-1605 (1995).

6. R.J. Roth, "Megavoltage portal radiography using film and Xerox techniques," *Radiologic Technology*, **36**, 65-69 (1964).

7. J.N. Wolfe, L. Kalisher, and B. Considine, "Cobalt 60 treatment field verification by xeroradiography," *Am. J. Roentgen.*, **119**, 916-918 (1973).

8. A.I. Kampinskas, Y.A. Zimbutz, and R.S. Karchyauskas, "Radiation sensitivity and fatigue of electroradiographic plates to high energy ionizing radiation," *J. Sci. Appl. Photo. Cinema.* **32**, 244-255 (1990).

9. Y.A. Borisov and A.I. Kaminskas, "Xeroradiography in flaw detection based on high energy penetrating radiation," *Russian J. Nondestructive Testing*, **29**, 61-65 (1993).

10 A.L. Boyer, L. Antonuk, A. Fenster, M. Van Herk, H. Meertens, P. Munro, L.E. Reinstein, and J. Wong, "A review of electronic portal imaging devices (EPIDs)," *Med. Phys.*, **19**, 1-16 (1992).

11. Y. Zhu, X.Q. Ziang, and J. Van Dyk, "Portal dosimetry using a liquid ion chamber matrix: dose response studies, " *Med. Phys.*, **22**, 1101-1106 (1995).

12. B.J.M. Heijmen, K.L. Pasma, M. Kroonwijk, V.G.M. Althof, J.C.J. de Boer, A.G. Visser, and H. Huizenga, "Portal dose measurement in radiotherapy using an electron portal imaging device," *Phys. Med. Biol.*, **40**, 1943-1955 (1995).

13. J.A. Rowlands, G. DeCrescenzo, and N. Araj, "X-ray imaging using amorphous selenium: Determination of x-ray sensitivity by pulse height spectroscopy," *Med. Phys.*, **19**, 1065-1070 (1992) and references therein.

14. H. Fiedler and F. Laugwitz, "Zur Quantenausbeute elektroradiographischer Selenschichten," *J. Signal AM*, **9**, 229-235 (1981).

15. C.A. Klein, "Bandgap dependence and related features of radiation ionization energies in semiconductors, "*J. Appl. Phys.*, **39**, 2029-2038 (1968).

16. R. C. Alig and S. Bloom, "Secondary-electron-escape probabilities," *J. Appl. Phys.*, **49**, 3476-3480 (1978).

17. S.O. Kasap, "Photoreceptors: The Selenium Alloys" in *Handbook of Imaging Materials* edited by A.S. Diamond, (Marcel Dekker Inc., New York, 1991) pp. 329-377.

18. B. Polischuk, Noranda Advanced Materials (private communication).

19. D. Hunt (Sunnybrook Health Sciences Centre, Toronto, private communication, 1996).

20. C. Haugen and S.O. Kasap, "Langevin recombination of drifting electrons and holes in stabilized a-Se (Cl-doped a-Se:0.3% As) ," *Phil. Mag. B*, **71**, 91-96 (1995).

21. P. Langevin,"Recombinaison et mobilites des ions dans les gaz," *Ann. Chim. Phys.*, **28**, 287-433 (1903).

22. H.E. Johns and J.R. Cunningham, *The Physics of Radiology*, 4th ed. (Thomas, Springfield, 1983) pp. 296-297, pp. 291-293.

23. D. Moses, "Mechanism of carrier photogeneration in amorphous selenium: Fast transient photoconductivity," *Phys. Rev. B.*, **53**, 4462-4470 (1996).

24. D.M. Pai and R.C. Enck, "Onsager mechanism of photogeneration in amorphous selenium," *Phys. Rev. B.*, **11**, 5163-5174 (1975).

25. J. Hirsch and H. Jahankhani, "The carrier yield in a-Se under electron bombardment, " *J. Phys.: Condens. Matter*, **1**, 8789-8798 (1989).

26. H.A. Kramers, "On a modification of Jaffe's theory of column ionization," *Physica*, **18**, 665-675 (1952).

27. M. Schott, "Yield of carrier generation in organic solids under electron bombardment II," *Mol. Cryst. Liq. Cryst.*, **10**, 399-409 (1970).

28. *ICRU Report 37 "Stopping powers for electrons and positrons"* (International Commission on Radiation Units and Measurements, Bethesda, MD, U.S.A., 1984).

29. L. Onsager, "Initial recombination of ions," *Phys. Rev.*, **54**, 544 (1938).

30. W. Que and J.A. Rowlands, "X-ray photogeneration in amorphous selenium: Geminate versus columnar recombination," *Phys. Rev. B.*, **51**, 10500-10507 (1995).

31. J. Halbleib, "Structure and Operation of the ITS Code System," in *Monte Carlo Transport of Electrons and Photons*, edited by T.M. Jenkins, W.R. Nelson, and A. Rindi, (Plenum Press, New York, 1988) pp. 249-262.

32. A.E. Nahum, "Simulation of dosimeter response and interface effects," in *Monte Carlo Transport of Electrons and Photons*, edited by T.M. Jenkins, W.R. Nelson, and A. Rindi (Plenum Press, New York, 1988) pp. 523-547.

33. M.J. Berger, "ETRAN - Experimental benchmarks," in *Monte Carlo Transport of Electrons and Photons*," edited by T.M. Jenkins, W.R. Nelson, and A. Rindi (Plenum Press, New York, 1988) pp. 183-219.

34. A generalized version of this equation can be obtained from J.A. Rowlands and D.M. Hunter, "X-ray imaging using amorphous selenium: Photoinduced discharge (PID) readout for digital general radiography," *Med. Phys.*, **22**, 1983-1996 (1995).

35. Trek Models 344 and 320B Electrostatic Voltmeters, Trek Industries, Medina, New York. The latter probe was used to measure low (<100 V) potentials only.

36. RMI Gammex, Middleton, Wisconsin, U.S.A.

37. Keithley Model 35065 Digital Dosimeter, Keithley, Cleveland, Ohio.

38. *CRC Handbook of Radiation Chemistry*, edited by Y. Tabata, (CRC, Boca Raton, 1991).

39. A. Chatterjee, "Interaction of ionizing radiation with matter," in *Radiation Chemistry: Principles and Applications*, edited by Fahataziz and M.A.J. Rodgers, (VCH, New York, 1987) pp. 9-28.

40. M. Inokuti, J.L. Dehmer, T. Baer, and D.J.D. Hanson,"Oscillator-strength moments, stopping powers and total inelastic-scattering cross sections of all atoms through strontium," *Phys. Rev. A.*, **23**, 95-109 (1981).

41. S.M. Sze, *Physics of Semiconductor Devices*, (Wiley, New York, 1981).

42. A. Mozumder, "Charged particle tracks and their structure," in *Advances in Radiation Chemistry*, vol. 1, edited by M. Burton and J.L. Magee, (Wiley, New York, 1969) pp. 18-21.

43. A.K. Ganguly and J.L. Magee, "Theory of radiation chemistry III: Radical reaction mechanism in the tracks of ionizing radiations," *J. Chem. Phys.* **25**, 129-134 (1956).

44. R.A. Street, "Recombination in amorphous semiconductors," *Phys. Rev. B.*, **17**, 3984-3995 (1978).

45. J.L. Magee, K. Funabashi, and A. Mozumder, "Theory of basic processes in radiation chemistry," in *Proceedings of the 6th Conference on Radioisotopes*, 1964 pp. 755-66.

46. U. Schiebel, W. Hillen, and T. Zaengel, "Image quality in selenium-based digital radiography,"*SPIE Medicine XIV/ PACS IV*, **626**, 176-184 (1986).

47. E. Montrimas and J. Rakasuskas, "The discharge mechanism of Se electroradiographic layers irradiated by x-rays," in *Current Problems in Electrophotography*, edited by W.F. Berg and K. Hauffe, (Walter de Gruyter and Co., Berlin, 1972) pp. 39-47.

48. J.L. Donovan, "X-ray sensitivity of selenium," *J. Appl. Phys.*, **50**, 6500-6504 (1979).

49. G. Borasi and R. Cubeddu, "Some remarks on selenium plates for xeroradiography," *J. Appl. Phys.*, **48**, 1375 (1977).

50. W.D. Fender, "Quantification of the xeroradiographic discharge curve," *SPIE*, **70**, 364-371 (1975).

51. R. Birch, M. Marshall, and G.M. Ardran, *Catalog of spectral data for diagnostic x-rays*, (Hospital Physicists Association, London, 1979).

52. D.M. Tucker, G.T. Barnes, and D.P. Chakraborty, "Semiempirical model for generating tungsten target x-ray spectra," *Med. Phys.*, **18**, 211-218 (1991).

53. D.W.O. Rogers, G.M. Ewart, A.F. Bielajew and G. Van Dyk, "Calculation of electron beam contamination in a ^{60}Co therapy beam," in *"Proceedings of the IAEA International Symposium on Dosimetry in Radiotherapy"* vol. 1, (IAEA, Vienna, 1988) pp. 303-312.

Chapter 4

Portal Imaging using Amorphous Selenium: Detective Quantum Efficiency

"Science clears the fields on which technology can build."

- Werner Heisenberg 1901-1976

A version of this chapter has been submitted to Medical Physics (1997).

I. INTRODUCTION

Although electronic portal imaging devices are widely available, a disappointing fraction are used clinically on a routine basis.[1] Part of the reason for this may be due to the poor image quality of these systems. For digital imaging systems, image quality may be measured by the detective quantum efficiency (DQE) which describes how efficiently the detector uses the information in the incident x-rays. Both types of commercially available systems, the liquid ion chamber array and the fluoroscopic portal imager, have low DQE. Signal-to-noise analyses[2,3,4] and measurements[5] have determined that fluoroscopic systems have a low DQE (~0.1%) in part due to the poor optical coupling between the primary x-ray detector (metal plate + phosphor screen) and in part due to the video camera which converts the optical image into an electrical (voltage) signal. To improve the image quality over that of fluoroscopic systems, a better approach would be to directly couple the primary detector to the charge conversion stage by bonding the detector element directly to the primary x-ray detector.

The liquid ion chamber array has image quality comparable to that of the fluoroscopic system. It consists of 256 x 256 chambers which are read out by applying high voltage to one row at a time, so only 1/256th of the detector is actively detecting x-rays. This is augmented to some extent by charge trapping in the unbiased part of the insulating liquid resulting in some additional charge signal.[6] If all the freed charge was accumulated until the image is read out, the DQE could be improved. One way of overcoming the weakness of both systems is to use a photoconductor know as amorphous selenium (*a*-Se).[7] It can be bonded directly to the metal plate eliminating the coupling problem in the fluoroscopic detector and because it has a very low leakage current, charges are

retained on its surface for a long time before they are read out eliminating the charge loss problem in the liquid ionization chamber array.

One promising approach for the readout of *a*-Se is to couple it to a flat panel.[8,9] Alternative approaches using phosphors have already been investigated and show promise.[10] There are a variety of advantages to using *a*-Se in flat panels over phosphors including simplification of the design of the flat panel readout and improved resolution. It is our goal to provide information for the design of an optimal *a*-Se based detector for this, or other readout methods,[11,12] and for comparison with phosphor based systems. To do so requires an understanding of the signal and noise properties of image formation in *a*-Se when irradiated by megavoltage photons. In Chapter 3, we examined the signal properties of *a*-Se.[13] In this chapter, the spatial frequency dependent signal-to-noise ratio, or more specifically, the DQE(f), is examined.

The primary sensor for portal imaging consists of a buildup metal plate of thickness d_{plate} followed by an x-ray to signal transducer. The principal interaction of megavoltage x-rays is Compton scattering producing ionizing secondary electrons. These interactions occur both in the metal plate and transducer. The secondary electrons reaching the transducer deposit energy, resulting in an image signal. Radiographic film, phosphor screens, and insulating liquid layers are currently being used clinically as transducers. However, as indicated previously, these detectors suffer from added noise and signal loss associated with their readout. Therefore we hypothesized that with an optimized *a*-Se sensor taking advantage of recent advances in its readout, improvements in the image quality over existing approaches can be obtained. Wang *et al.*[14] have performed Monte Carlo simulations of the expected latent image quality. Here, we produce a similar model, but with experimental measurements to verify our results.

Fig. 1 illustrates how an image can be produced using *a*-Se. Initially, the *a*-Se layer has a uniform charge distribution resulting in a uniform electric field throughout the bulk. Energy deposition in the *a*-Se produces electron-hole pairs which separate and drift to opposite surfaces under the influence of the electric field changing the surface charge distribution. Thus a distribution of x-rays incident on the detector will result in a charge image.

To compare *a*-Se detectors with existing systems, it is necessary to determine the signal-to-noise properties of this latent image; specifically, the spatial frequency dependent detective quantum efficiency, DQE(f), of a quantum noise limited *a*-Se detector. Our approach was to use a Monte Carlo calculation to model the zero spatial frequency detective quantum efficiency, DQE(0), of a metal plate + *a*-Se detector which has previously been done in phosphors.[15,16] We estimate the shape of the DQE(f) by considering the mechanisms of image formation and normalize it at zero spatial frequency using the Monte Carlo calculation. These theoretical estimates are compared with measurements made on the *a*-Se target of a video tube (Saticon) with a glass faceplate used as the buildup layer. Good agreement between theory and experiment validated the model at megavoltage energies. Finally, we used the model to determine the DQE(f) of an ideal portal imager using amorphous selenium.

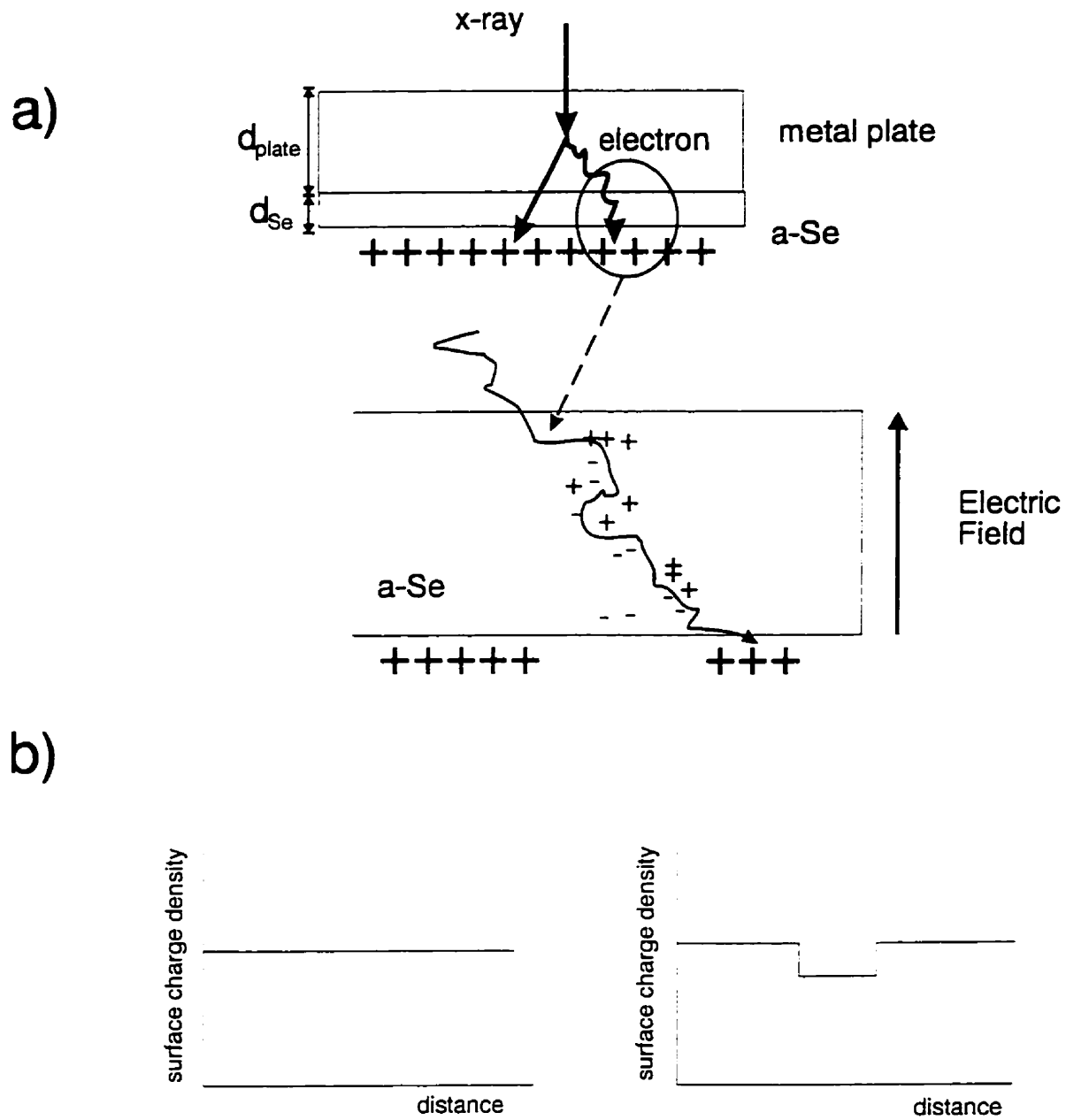

Fig.1 Formation of a charge image in a photoconductor. a) The x-ray interacts in the buildup plate and scatters incoherently. The secondary electron may emerge from the metal buildup plate and deposit energy in the a-Se. As the electron passes through the a-Se, it deposits energy that creates electron hole pairs which travel to the surface of the a-Se under the influence of the electric field to neutralize surface charges thus forming a charge image as illustrated in (b).

II. DQE(f) MODEL

A. Definition of DQE

The zero spatial frequency detective quantum efficiency, DQE(0), is defined as:[17]

$$DQE(0) = \frac{SNR_{out}^2(0)}{SNR_{in}^2(0)}, \qquad [1]$$

where $SNR_{out}^2(0)$ is the zero spatial frequency signal-to-noise ratio at the output of the system and $SNR_{in}^2(0)$ equals the number of x-rays incident on a pixel of the detector. The spatial frequency dependent DQE(f) may be calculated using:[17]

$$DQE(f) = \frac{DQE(0)MTF^2(f)}{NPS_0(f)}, \qquad [2]$$

where $NPS_0(f)$ is the noise power spectrum of the system normalized to unity as f approaches 0, and MTF(f) is the modulation transfer function of the system.

B. Pulse Height Spectrum

The noise of an x-ray quantum limited detector may be described by the counting statistics associated with the detection and conversion of an incident x-ray into a charge signal. For each x-ray that is detected, electron-hole pairs are produced. We consider three sources of variation or noise in an *a*-Se detector. These are variations in the: (i) number of x-rays detected, (ii) amount of energy deposited per detected x-ray, and (iii) gain (number of electron-hole pairs formed per unit energy absorbed) of the *a*-Se layer. All these sources of noise will reduce SNR_{out}^2 and hence DQE(0). For phosphors,

Swank showed[18] that the DQE(0) determined from a pulse height spectrum, PHS, a histogram of the probability that an event of a given size will occur as a function of the size of the event, will correctly include all these factors. Theoretical analyses and calculations based upon this approach have been performed on *a*-Se at mammographic energies[19] and using Monte Carlo calculations on phosphors at megavoltage energies.[16,7] Here we will employ Monte Carlo calculations for *a*-Se at megavoltage energies.

We define two pulse height spectra: PHS(E), in which the number of energy deposition events are binned as a function of the energy, E, deposited per incident x-ray, and PHS(Q) which is binned in terms of the charge signal, Q, in the *a*-Se per incident x-ray. The former may be obtained directly from the Monte Carlo code, but it is the latter that is the actual measured quantity. The two are related by

$$Q_i = \frac{E_i}{W_\pm}, \qquad [3]$$

where E_i is the *i*th energy bin, Q_i is the *i*th charge bin and $W_\pm$ is the energy required to produce an electron-hole pair which has previously been shown to be both energy and field dependent.[13] The latter can be controlled by maintaining a constant field during irradiation either by using an amount of radiation small enough so that the *a*-Se layer is not significantly discharged or by applying a constant operating field across the *a*-Se, using for instance, an electrode. We ignore the negligible effect of shot noise arising from stochastic variations in the number of charges formed from an energy deposition E_i since the gain ($= E_i / W_\pm$) is large.[18]

1. Relationship of PHS to DQE(0)

The PHS(E) is generated by counting and binning by size the energy deposition events arising from x-ray interactions in the detector and normalizing to the number of incident x-rays. The ratio of the total number of pulses to the number of incident x-rays is the quantum efficiency of the detector, A_q. If all the pulses were the same size, the DQE(0) equals A_q, but because there is variation in the size of the pulses, this introduces a second source of noise which reduces the DQE(0) by the Swank factor,[18] A_s. Thus, the DQE(0) is given by:

$$DQE(0) = A_q A_s \ . \qquad [4]$$

The PHS and hence the DQE(0) of the detector depends upon the thickness of the buildup plate d_{plate} and the thickness of the *a*-Se layer, d_{Se}. It has been shown[15] that increasing d_{plate} increases A_q, but only to the full buildup thickness (d_{max}). Thus we set the mass thickness $d_{plate}=d_{max}$. An upper practical limit to d_{Se} is determined by the carrier range and the maximum field that can be applied. The former depends upon the preparation of the *a*-Se[20] and the latter is usually limited by the leakage current. Currently, the typical thickness of d_{Se} is ~ 500 μm (~ 200 mg/cm^2). Assuming that the dominant carrier loss mechanism is electron trapping,[20] and using the range parameters from Chapter 3 (i.e. electron lifetime = 300 μs and electron mobility =3x10^{-3} cm^2/(Vs)),[13] the fraction of charge lost to trapping may be obtained by modelling the *a*-Se layer as a capacitor which is discharged by x-rays. By calculating the energy dissipated through the displacement current resulting from the movement of charge carriers through the bulk of the *a*-Se before trapping, the fraction of the signal lost due to trapping can be calculated.[21] Neglecting any attenuation of the beam in the *a*-Se, at 500 μm, ~90% of the signal is collected at the usual operating field of ~10 V/μm. Increasing the *a*-Se thickness to 1 mm (426 mg/cm^2) would result in slightly reduced (85%) signal collection and even at 2 mm, most (77%) of the charge is collected. Therefore a conservative range of *a*-Se layer thicknesses ranging

from nearly 0 to 1000 μm are considered.

We used the Monte Carlo code, CYLTRAN[22] to model the PHS(E) for *a*-Se detectors with glass or copper buildup materials irradiated by ^{60}Co and 6 MV pencil beams whose spectra were obtained from the literature.[23,24] The cutoff energies for photon and electron transport were set to 1 keV and 2.4 keV respectively. The default step size for electron transport is calculated from the CSDA range of the electron. A new smaller step is calculated after an ~8% reduction in energy.

First, the PHS(E) in cylindrical detectors consisting of a 20 cm (effectively infinite) diameter 1 mm thick copper plate + *a*-Se layers between 5 and 1000 μm thick were simulated. One million photon histories were run for each d_{Se}. Second, a 2.5 cm diameter video tube with a 2.45 mm glass faceplate over a 5 μm *a*-Se target (Saticon) was modelled to compare to experiment (see section III). To simulate backscattering from the glass walls of the vidicon, a hollow 15 cm long glass cylinder with a 2.5 cm outside diameter with 2 mm thick walls was added to the glass + *a*-Se target. To obtain a better estimate for comparison to experiment, ten million photon histories were run to obtain the PHS(E) in the Saticon. The ratio of the total number of pulses in the PHS(E) to the number of incident photons gave A_q. The Swank factor was obtained from[18]

$$A_s = \frac{M_1^2}{M_0 M_2}, \qquad [5]$$

where $M_j = \Sigma_i (N_i E_i^j)$ is the *j*th moment of the PHS(E) given in terms of N_i, the number of pulses per incident photon in the *i*th bin of energy, E_i. Eq. 5 was used to calculate the zero spatial frequency DQE from the PHS(E), to obtain the $DQE_E(0)$ of the *a*-Se layer + copper buildup plate.

2. Evaluation of DQE(0)

To verify our model, we compared the $DQE_E(0)$ of a 1 mm copper plate with a 400 mg/cm^2 Gd_2O_2S:Tb (mean density = 3.5 g/cm^3) screen irradiated by a 6 MV beam[24] with those of previous investigators.[15,16] The value of $DQE_E(0)$ was 1.8×10^{-2} (A_s=0.52, A_q= 3.45×10^{-2}), in reasonable agreement with Jaffray *et al.*[16] (1.7×10^{-2}) and Radcliffe *et al.*[15] (1.8×10^{-2} for 500 mg/cm^2). Thus, our model is in agreement with theirs, which was experimentally tested.

Fig. 2 shows the PHS(E) from CYLTRAN for a metal plate with a 5 μm *a*-Se layer irradiated by a 6 MV beam, and a Saticon (2.45 mm glass + 5 μm *a*-Se; see section III.C) irradiated by a ^{60}Co beam. For both spectra, the majority of the energy deposition events lie between 2 and 3 keV. To verify that this peak was not an artifact resulting from the termination of low energy electron histories in the *a*-Se at the cutoff energy (2.4 keV), the cutoff energy was increased to 10 keV, but no difference in the PHS(E) was found. Rather, the peak results from many high energy electrons (several hundred keV) passing straight through the *a*-Se. To confirm that the position of the peak was consistent with this mechanism, an analytical calculation was performed. The average energy[25] transferred by a Compton scattering event from a 2 MeV photon in the copper buildup plate is ~1 MeV. A forward directed electron of this energy passing perpendicularly through 5 μm of *a*-Se deposits, on average, an amount of energy, $E_i=S_e d_{Se}$ = 2.6 keV where S_e is the collisional stopping power[26] of the *a*-Se to the 1 MeV electron (1.23 MeV cm^2/g). Further evidence for this mechanism is that the position of the peak shifts approximately linearly with d_{Se} for smaller d_{Se} (i.e. at least up to 50 μm). Thus our proposed mechanism is in agreement with the energy of the peak.

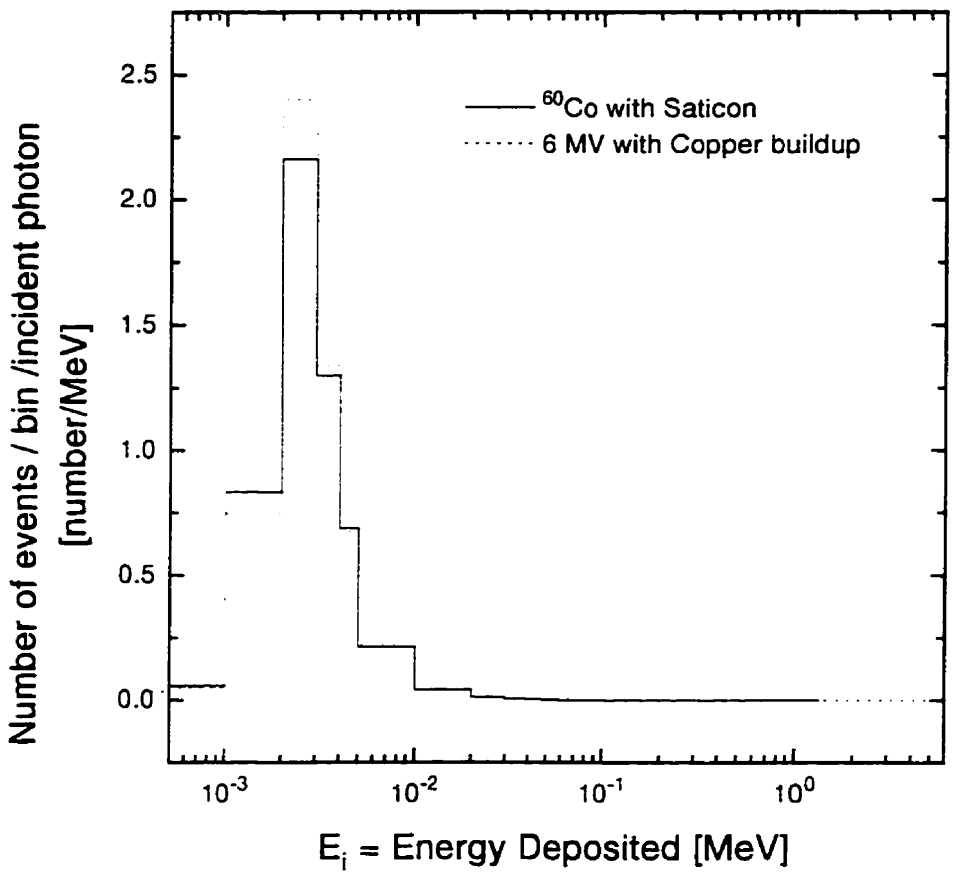

Fig. 2 Pulse height spectrum as a function of energy deposited in 5 μm a-Se calculated from CYLTRAN for two different buildup materials and spectra. The PHS(E) is the number of incident photons giving rise to energy depositions between E_i and E_{i+1} divided by $E_{i+1} - E_i$.

Although the vast majority of the energy deposition events occur from the transit of a high energy electron through the *a*-Se, for some cases, significantly more energy is deposited as shown by the high energy tail of the PHS(E). Even though these events are very rare, they reduce A_s significantly. To determine the nature of the energy deposition mechanism giving rise to the high energy (E_i>10 keV) tail of the PHS(E), we added[27] a tracking mechanism to the CYLTRAN code. Each time a large energy deposition event occurred, the random number from which it was generated was recorded. The code was then run over with only these histories, but this time the energy of the secondary electrons in the *a*-Se were also tracked. We examined a total of 20 events. It was found that the large energy deposition events were caused by low energy electrons (i.e. electron energy, $E_e \lesssim$ 50 keV). These electrons are more readily scattered in the *a*-Se, so they have a greater path length and hence deposit more energy.

As indicated in Eq. 3, the electron energy affects the conversion of the PHS(E) to PHS(Q) since the x-ray sensitivity of *a*-Se (i.e. the amount of charge produced per energy deposited) is a function of x-ray energy.[13] We ascribed the energy dependence to additional recombination of electron-hole pairs for low energy or high linear energy transfer (LET) electrons. Specifically, for high LET electrons, the energy required to produce an electron-hole pair, $W_{\pm}$, increases by a factor of ~3 compared to a low LET electron. Because of the LET dependence of $W_{\pm}$, the deposition of energy from high LET electrons though greater due to their longer path length in the *a*-Se, would produce proportionally less charge per unit energy deposited than low LET electrons which pass straight through. For the energy deposition events we examined in which the energy pulse size E_i > 50 keV, all were produced by high LET electrons, and for E_i between 10 and 50 keV, approximately half of the events resulted from high LET electrons, but for E_i below ~10 keV, none were from high LET electrons. Therefore we took a weighted average of the value of $W_{\pm}$ depending upon the value of E_i and the probability

that it was produced by a high or low energy electron. Specifically, the PHS(Q) was estimated by assuming that each pulse in the PHS(E) of height N_i and energy E_i produced a charge pulse of height $N_iE_i/W_\pm$ where $W_\pm$ is given by

$$W_\pm = \begin{cases} 20\ eV & if\ E_i<10keV \\ 40\ eV & if\ 10keV<E_i<50keV \\ 60\ eV & if\ E_i>50keV \end{cases}. \qquad [6]$$

The effect of the LET dependence of $W_\pm$ on the PHS is shown in Fig. 3. The PHS(Q) calculated using the value of $W_\pm$ given in Eq. 6, and the PHS(Q) obtained using $W_\pm$ = 20 eV (i.e. assuming there was no LET dependence of $W_\pm$) are plotted. The LET dependence resulted in a re-binning of the high energy bins into proportionally lower charge bins, thus reducing the length of the high charge tail of the distribution. Since the PHS(E) of a 5 μm *a*-Se layer on copper buildup and glass buildup were very similar (see Fig. 2) the value of $W_\pm$ given by Eq. 6 was also used to calculate the predicted DQE, $DQE_p(0)$ for the Saticon.

Fig. 4 shows the PHS(E) for a 500 μm *a*-Se layer irradiated by a 6 MV beam. The PHS(E) is much broader due to increased number of direct photon interactions in the photoconductor and the increased path length of secondary electrons within the sensor (*a*-Se) as described by Jaffary *et al.*,[16] thus the PHS(E) does not have a high energy tail. Consequently, A_s is larger and less sensitive to large energy deposition events. Additionally, the LET dependent gain has a much smaller effect on the shape of the PHS(Q) in thicker layers since most of the large energy deposition events result from the full absorption of a high energy electron and the LET effect only occurs in the final small fraction of the energy deposition.

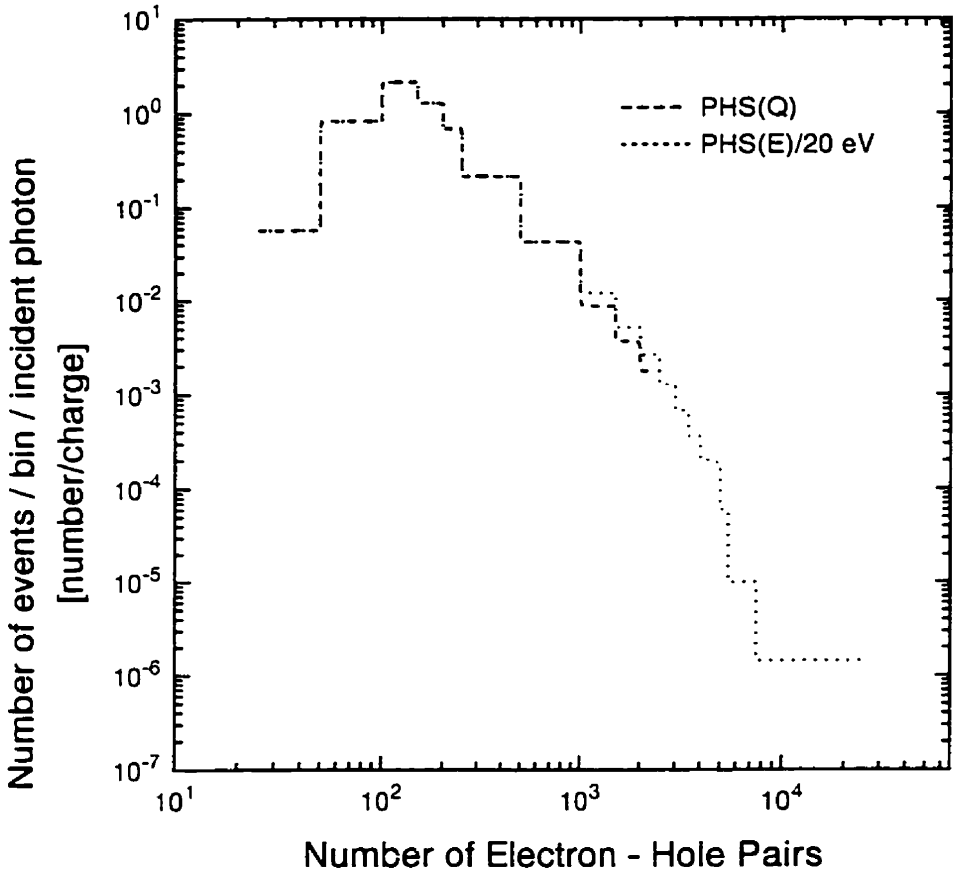

Fig. 3 Pulse height spectrum as a function of number of electron-hole pairs for a 6 MV beam irradiating a copper plate + 5 μm a-Se layer. The dotted line (·····) is the data from Fig. 2, but is converted to electron hole pairs assuming $W_{+/-} = 20$ eV. The dashed line (‾‾‾) is the PHS(Q) with $W_{+/-}$ given by Eq. 6. The data are plotted in log-log format to show the differences in the high energy tail.

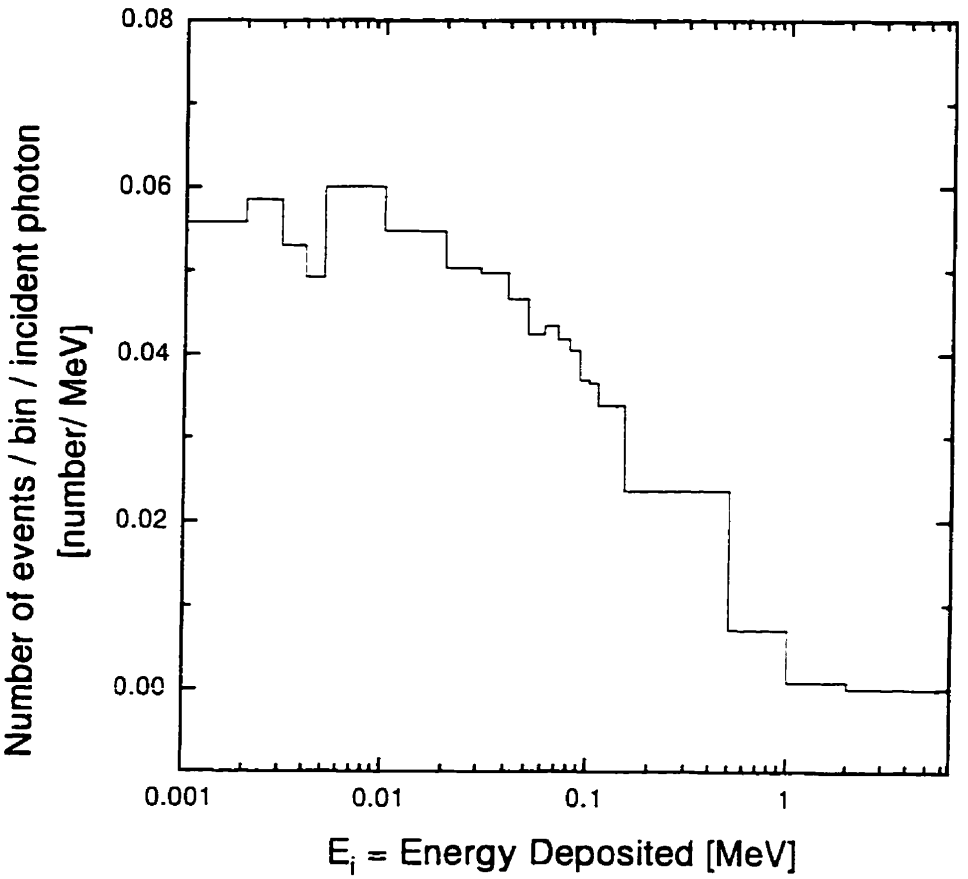

Fig. 4 Pulse height spectrum as a function of energy deposited in 500 μm a-Se irradiated by a 6 MV beam with a copper buildup plate. The PHS(E) was calculated from CYLTRAN.

This concept is illustrated in greater detail in Fig. 5. Two types of energy deposition are shown for two different layer thickness. X-rays A and B interact in thinner *a*-Se and C and D interact in thicker *a*-Se. Events A and C are more likely than events B and D, hence their pulse heights are larger on the PHS(E) shown below. X-ray A differs from B in that its secondary electron is of higher energy and goes straight through the *a*-Se while the secondary electron from B has a high LET component shown by the dotted line. The same holds for x-rays C and D. The energy difference arising from the higher LET part gives rise to a difference in the energy deposition which is shown as ΔE_{LET} in the PHS(E). Since it is only the lower energy electron that separates the pulse pairs from one another, the spacing between A and B is equal to that between C and D. However, since the energy deposited in C is greater than that in A, the relative energy separation between the pulse pairs (which influences the value of A_s by altering the skewness of the distribution) is much larger, hence the effect of the LET dependent gain on A_s is much larger for thin *a*-Se than thick.

3. Evaluation of DQE(f)

To calculate the DQE(f) using Eq. 2, the $NPS_0(f)$ and the MTF(f) are required. In many phosphors, for an x-ray quantum noise limited system, the $NPS_0(f)$ is approximately[28] the same shape as the $MTF^2(f)$. As shown in Fig. 6, this is because the large gain and scattering of light cause the line spread function (LSF) of one x-ray photon to be nearly the same as for many x-ray photons (i.e. optical blur is greater than the x-ray blur). However, for *a*-Se, this is not the case since the very high resolution[29] of *a*-Se results in a burst of electron-hole pairs from an individual x-ray photon which is very narrow. Hence the signal produced looks like a δ function and the NPS(f) is independent of f (spectrally white). The δ function is an excellent approximation because although there must be some spread of the electron hole pairs as they drift through the *a*-Se, this effect is negligible as

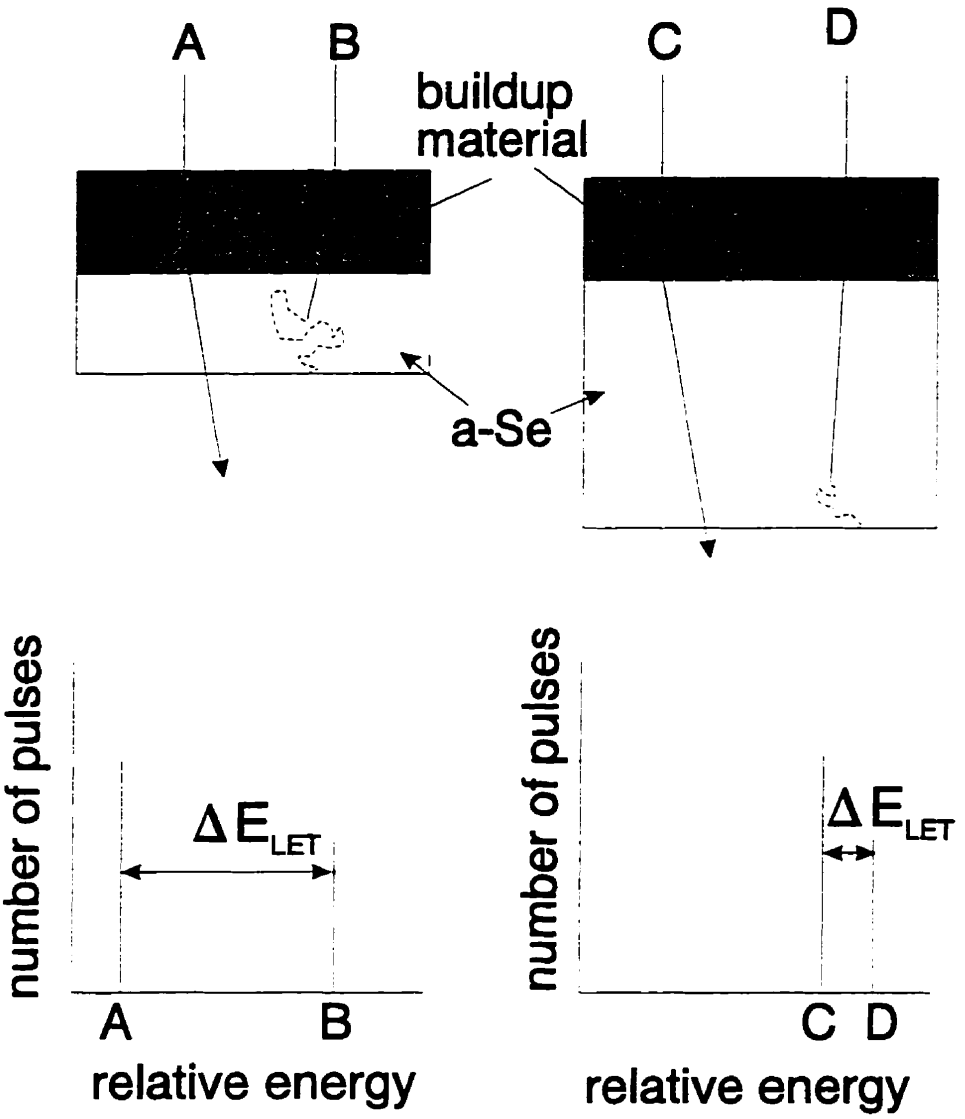

Fig. 5 Illustration of effect of selenium thickness on pulse size. Four different x-rays marked A, B, C and D produce pulses of different sizes. X-rays A and B are incident upon a thin layer of a-Se. X-ray A produces an electron which goes straight through while B produces a low energy or high LET electron (shown by dotted line) which has a longer path length and thus a larger pulse. X-rays C and D are incident upon a thicker layer of a-Se, hence the pulses are of higher energy than those of A and B. Since the difference between the different pulse pairs is due only to the different contribution from the high and low LET electrons, the energy spacing between A and B is the same as between C and D. But since the energy of A and B is much lower than the energy of C and D, the relative spacing is much larger. Events of type A and C are much more likely than events B and D, hence the height of A and C in the PHS(E) are greater than B and D.

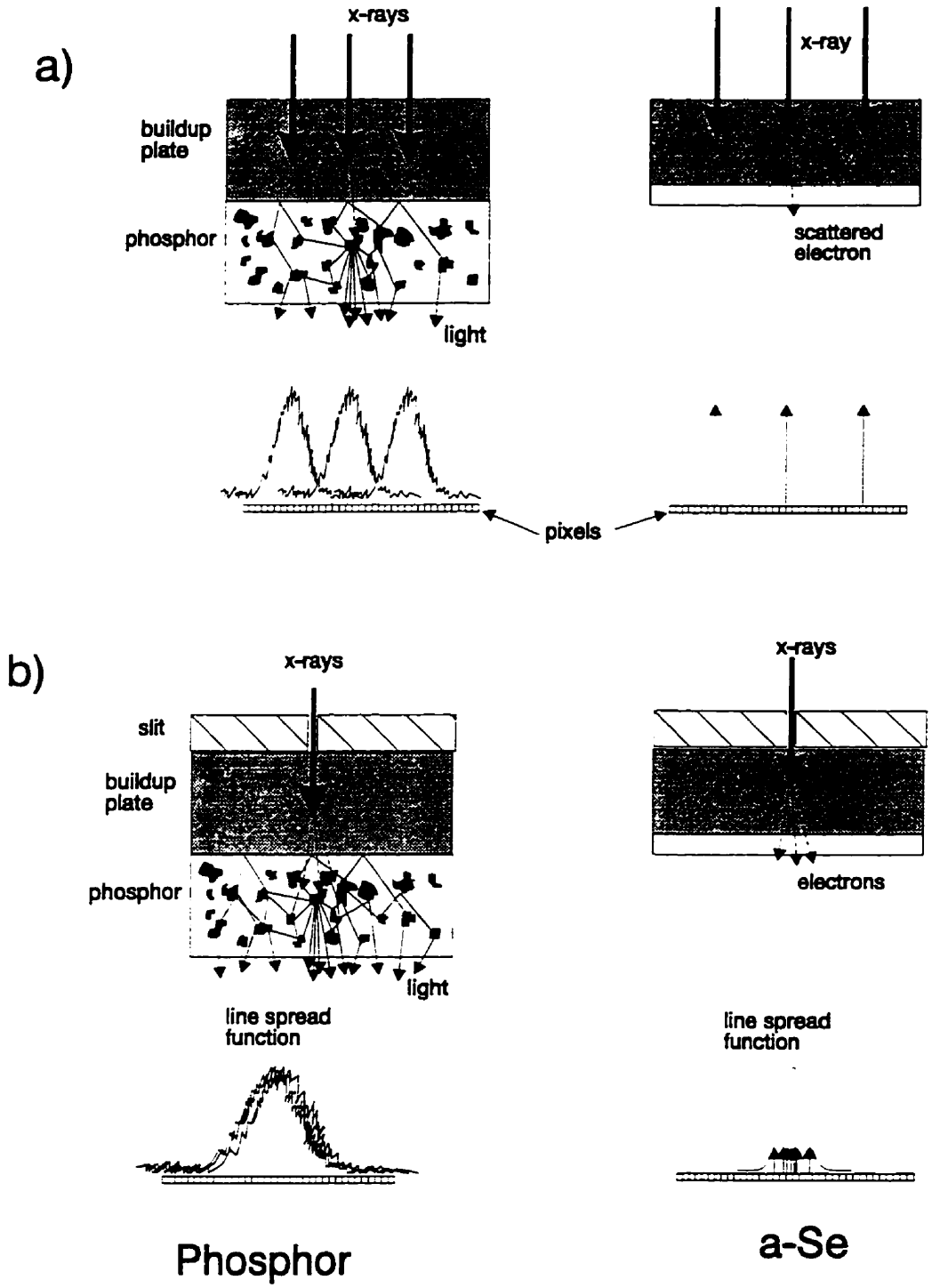

Fig. 6 Differences between response of a-Se and a phosphor to (a) noise and (b) resolution (MTF) measurements. In (a) multiple photons produce bursts of light from the phosphor and bursts of electron hole pairs from the a-Se. Since there is no spreading of signal in the a-Se, the response is a delta function. In (b) the line spread functions are shown to consist of these bursts of light or charge.

optical and x-ray images with resolutions up to 500 lp/mm have been reported.[7-30] Despite the high resolution for individual x-ray energy deposition events, the MTF(f) is not white because the measured LSF results from the average spread of *many* photons and electrons scattering in the buildup material, thus it is much broader than the spreading of an individual x-ray.

Therefore, to estimate the DQE(f), the $NPS_0(f)$ for *a*-Se detectors may be taken to be unity for all f. However, an estimate for the MTF(f) is also required. If $d_{Se} << d_{plate}$, the spread of electrons in the *a*-Se is negligible compared to the spread in the buildup plate and the MTF(f) of the latent image is entirely determined by the buildup plate. As d_{Se} increases to 500 μm, the MTF(f) will be reduced due to the additional spread of electrons in the *a*-Se. However, this change is relatively small (< 20%) according to Monte Carlo calculations as d_{Se} increases from 300 to 500 μm.[31] Measurements[4] of the x-ray spread in a metal plate + phosphor screen of similar average density (3.5 g/cm^3) and thickness to a 1000 μm *a*-Se (4.26 g/cm^3) layer indicate that the MTF(f) resulting from x-ray spread in the metal plate + phosphor is comparable to that of the optical spread alone. However, these LSF measurements were performed with film. In film, the LSF is the sum of the delta functions that result when Compton electrons exit the sensor. In *a*-Se, as the electron track passes through the layer, charges are produced over its entire length, and not just at the end.. Approximating the tracks as linear, and averaging the charge formation along the track, the LSF from *a*-Se will be narrower by approximately two. Using the experimental data,[4] this implies that the MTF(f) of a metal plate + *a*-Se layer compared to a metal plate alone is 0 at f=0, ~15% at f=0.5 mm^{-1}, and ~30% at f=1 mm^{-1}.

Thus we can obtain a good estimate of the MTF(f) for the *a*-Se detector by using published MTF(f)s for metal plates.[32] Therefore, for reasonable *a*-Se thicknesses, we can model the DQE(f) as

$$DQE(f) = DQE(0)MTF_b^2(f) , \quad [7]$$

where the $MTF_b(f)$ is the MTF(f) of the buildup material and DQE(0) is obtained as outlined in section II.B.1.

III. EXPERIMENTAL MEASUREMENT OF DQE(f) OF *a*-Se

To verify the model we required an imaging system. We chose to use a Saticon, a vidicon with a 5 μm *a*-Se target designed and used as an optical sensor. It is useful for our purposes because: (i) It is an established, well understood and characterized imaging system. (ii) The Saticon has a glass faceplate which can act as the buildup material in front of the *a*-Se.

The Saticon was directly irradiated with 1.25 MeV γ-rays from a Theratronics Theratron 780 ^{60}Co unit. ^{60}Co was chosen because its effectively monoenergetic spectrum made comparison with our Monte Carlo model (see sections IIB-C) more accurate than the bremsstrahlung spectrum from a linear accelerator.

A. Camera Characteristics

A conventional medical fluoroscopic camera (Machlett model SS600) which produced a standard video signal (NTSC interlaced image, 480 active lines) with an overscanned circle[33] was used. The camera was modified to integrate frames by turning off the scanning electron beam to permit image charge buildup on the target. After a preset delay of K frames, the scanning was reactivated and the accumulated charge from K+1 frames read off. All measurements, unless otherwise specified, were

made on the first active field of the resulting video signal. The linearity of the response of the camera to light has been established in Chapter 2. The dark current of the camera was negligible[5] compared to typical signals of ~ 200 mV that were used in our noise measurements. Linearity of the camera to ^{60}Co γ-ray irradiation was established by changing K over the range of K+1= 9 to 65 producing signals ranging from ~50 to 400 mV, spanning the range of K and signal used in our measurements.

The diameter of the active area of the vidicon was measured by selecting a line at the centre of the circle and measuring its width on an oscilloscope. To convert from time on the oscilloscope to distance across the face of the vidicon, a transparent ruler was imaged using a set of 1:1 relay lenses and the time between dips corresponding to the ruler graticule were measured. The conversion factor between time on the oscilloscope and distance across the face of the vidicon, H was 2.7 μs/mm, which yielded an active target diameter of 1.5 cm.

B. Measurement of Modulation Transfer Function

The modulation transfer function of the Saticon directly irradiated by γ-rays, $MTF_d(f)$, was determined as the Fourier transform of the line spread function (LSF) which was the image of a narrow slit. The slit was formed by a pair of 10 cm thick steel blocks clamped together upon a pair of narrow 250 μm shims and was oriented perpendicular to the scan direction of the electron beam. The blur from the large (1 cm) source was minimized by using a large (150 cm) source to detector distance. To align the slit, it was placed ~2 cm from the glass faceplate of the camera tube (N.B. the lens was removed) and illuminated with the field light of the ^{60}Co unit. The resulting signal, measured on the oscilloscope, was maximized by rotating the slit in small increments. The slit was then

irradiated and 128 lines were averaged to obtain an essentially noise free image of the 128 point LSF which was digitized by the oscilloscope at 40 ns (i.e. 15 μm) intervals. A background correction was performed in which the slit was closed by removing the shims, and the signal resulting from transmission of radiation through the blocks, was subtracted from the one obtained with the slit to obtain the LSF. The LSFs were fast Fourier transformed to get the $MTF_d(f)$.

To separate the loss of resolution in the glass faceplate resulting from the spread of Compton scattered electrons within the glass from any spreading in the *a*-Se, the MTF(f) of the glass faceplate, $MTF_g(f)$, was established by placing the slit on top of a ~2 mm piece of glass and a single emulsion film (Kodak Ortho M) in an evacuated cassette. The LSF measurement was identical with that from the Saticon except for the alignment procedure. Because film is not a real time imaging system, it was not practical to iteratively change the slit position. Instead, the slit was aligned using the field light and cross wires of the ^{60}Co unit and by using a spirit level to ensure that both the top surface of the slit and ^{60}Co unit were parallel to one another. The film was exposed using ^{60}Co, developed and digitized into 125 μm pixels using a photodiode array film digitizer. Five profiles of the LSF were then obtained, linearized using the dose response curve of the film,* averaged, and Fourier transformed to obtain the $MTF_g(f)$.

The width of the slit was measured radiographically using a 50 kVp beam and a single emulsion film (Kodak Min-R) in an evacuated mammography cassette to produce a blur free image of the slit. The slit image was then measured using a microscope with a graticule in its eyepiece and confirmed to

* The dose response curve was obtained by irradiating the film in full buildup conditions in a tissue equivalent phantom with ^{60}Co.

be 250 μm ± 10%. A correction for the width of the slit was performed by dividing the measured MTF(f) by the sinc with its first zero at 4 mm^{-1}.

C. Measurement of Noise Power Spectra

The noise power spectrum, NPS, was measured from the output of a directly irradiated Saticon. The lens was removed from the camera and the radiation field was collimated to the face of the video tube to avoid unnecessary irradiation of the camera electronics. To obtain a ~ 200 mV signal, the camera was blanked for 33 frames. A similar Saticon was dismantled and the glass faceplate was measured to be 2.45 mm thick. The *a*-Se target was taken to be 5 μm thick.[34] The target potential was 47 V, resulting in a field of ~10 V/μm.

The method of measuring the NPS from this video camera has been described previously.[5,35] Briefly, a video line near the center of the image was passed through a 5 MHz anti-aliasing low pass filter into a digital oscilloscope which digitized it into 256 points at 40 ns intervals. Two hundred and fifty video lines were collected at ~ 3 second intervals and sequential lines were subtracted from one another to remove structural noise. The subtracted video lines were then Fourier transformed and the resulting spectra averaged to obtain the NPS with an uncertainty[17] of ~9%. The NPS_X resulting from direct irradiation of the camera includes the x-ray quantum noise power spectrum, NPS_q, the camera noise power spectrum, NPS_V, (dominated by noise in the amplifier) and the electron shot noise power spectrum, NPS_e. To extract the x-ray quantum noise, the camera was illuminated with an incandescent light source to produce the same signal (~200 mV) as with the gamma rays. The resulting spectrum, NPS_L consists of NPS_V and NPS_e, thus subtracting NPS_L from NPS_X yields NPS_q.

To ensure that the measured signal used to obtain $NPS_q(f)$ was due to x-ray generated energy deposition events in the *a*-Se alone, several experiments were performed to exclude spurious effects. We first investigated whether light formed by high energy secondary electrons in the glass contributed to the measured signal. Since it was not possible to remove the glass faceplate from the Saticon, its effect was determined by adding further transparent material and extrapolating to zero thickness of faceplate. It has been shown[36] that in glass, most of the light produced by high energy x-rays is from Čerenokov radiation. Since Čerenokov production only depends upon one material dependent parameter,[37] the index of refraction, n, and for glass, n ranges from 1.45 to 1.55 while n for plexiglass[38] is 1.48-1.50, the production of light in plexiglass is essentially identical to that for glass. Light produced at the front face of the tube was increased by placing clear polished plexiglass cylinders (up to 6 cm thick) on the surface of the glass and irradiating the camera. The signal was measured both with the plexiglass in optical contract with the glass faceplate and subsequently with a piece of opaque material between the glass faceplate and the plexiglass. As shown in Fig. 7, the signals with and without the opaque material were then subtracted to yield the signal from Čerenokov as a function of plexiglass thickness. The signal due to Čerenokov, obtained from the slope of the line multiplied by the mass thickness of the glass, d_{glass}, accounts for ~7 mV ± 10% or ~5 % of the total signal of 190 ± 6 mV.

Second, we investigated whether irradiation of the glass in the tube behind the target produced light by irradiating the tube from the side, while ensuring that the target was shielded from the beam. Any extra signal produced in the tube would be due to light or scattered radiation, however no signal was observed within the rms noise of the video camera (± 2 mV).

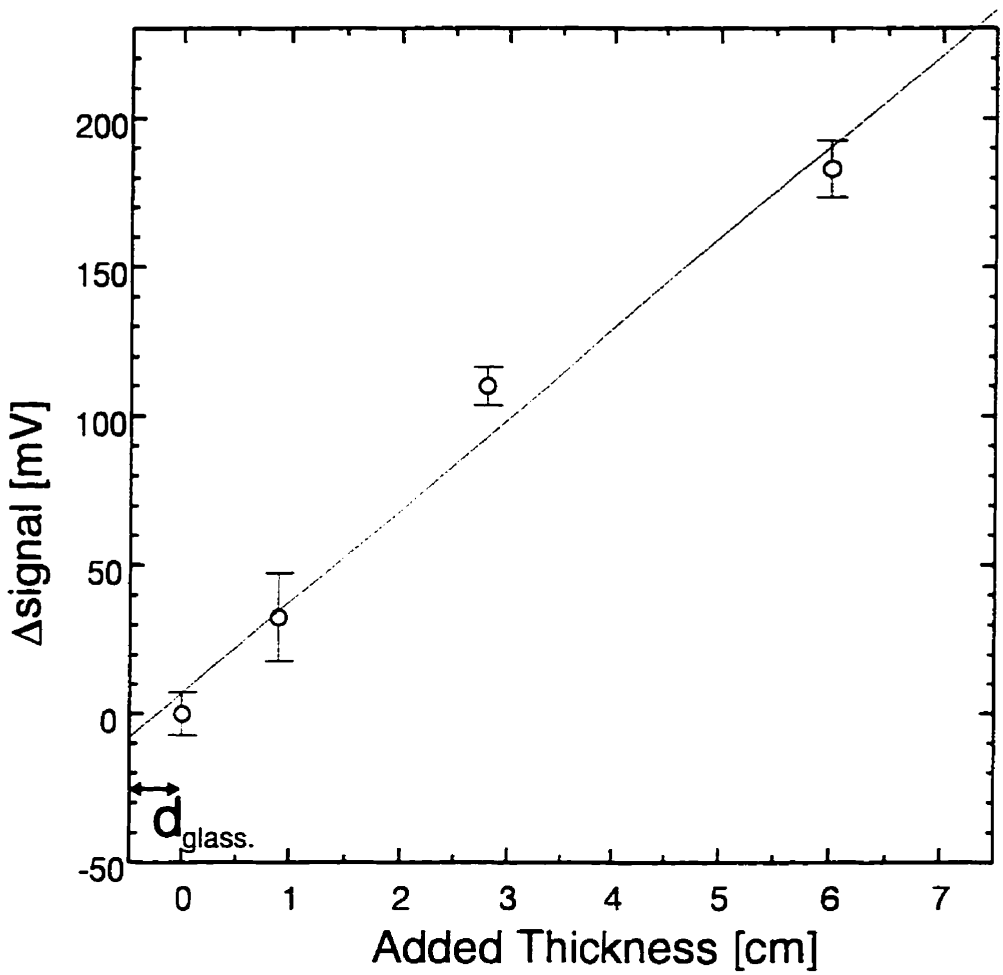

Fig. 7 Cerenkov light signal generated by ^{60}Co beam as a function of added thickness of clear plexiglas. The symbol d_{glass} refers to the equivalent mass thickness of the glass faceplate assuming a density of 2.5 g/cm^3 and Δsignal at this thickness gives a measure of the amount of signal produced by light in the glass faceplate.

Third, we checked if irradiation of the camera electronics was contributing additional signal by disconnecting the camera tube target and irradiating the camera, but again no significant (i.e. within ±2 mV) signal was observed.

D. Determination of $DQE_{M(0)}$

The DQE(0) from our measurements, DQEM(0) was calculated using Eq. 1. The SNRout was obtained from the ratio of the signal (200 mV) to the rms noise, given by the square root of the integral of the $NPS_q(f)$ (8.5 mV). The SNR^2_{in} equals the number of x-rays incident on a pixel. The exposure was measured using a Baldwin Farmer 0.6 cm^3 cylindrical ionization chamber with a Delrin ^{60}Co buildup cap and the fluence was calculated using the published conversion factor[39] for 1.25 MeV photons ($1.63x10^9$ photons cm^{-2} R^{-1}). The pixel area was determined as the product of the aperture response of the camera and the height of a line. The aperture response is the Fourier transform of the 5 MHz anti-aliasing filter. Approximating the 5 MHz filter by a rectangular function of width W_f, centred on f=0, where $W_f/2$=5 MHz, the aperture function is a sinc function with its first zero at $1/W_f$. Squaring this function, gives the aperture response to noise power. The pixel is the equivalent constant response function that will pass the same noise power (i.e. has the same integral). This rectangular aperture has a width $1/W_f$. Thus, the width of a pixel, $w_p = 1/(HW_f) = 3.7x10^{-2}$ mm. The height of the pixel, $3.1x10^{-2}$ mm, was obtained as the ratio of the diameter of the active area being scanned (see section A) to the 483 active lines in the image.

Two corrections were applied to the $DQE_M(0)$ calculation, both of which had the effect of reducing the DQE. These were: (i) the different response of the two video fields and (ii) the effect of light produced in the glass. Using a set of green LEDs and an integrating sphere as a uniform light

source,[40] the relative size of the first, second, and third fields after 32 frames of blanking were measured using an oscilloscope. The third and fourth fields were approximately at the signal level corresponding to that of continuous readout, implying that there was virtually no third field lag. The ratio of the signal size of the first field to the second field, equal to the effective relative pixel sizes of the two fields was ~ 1.5. The different pixel sizes between the two fields result from the Gaussian shape of the scanning electron spot, thus some of the second field is read off by the tails of the first field. This implies that proportionally more γ-rays were being detected in the first field than the second field. Since the ratio of first to second field is 3:2, the first field read off 3/5 of the total charge. If two fields were the same size, the first field would have read off half the charge. Thus, a factor equal to the ratio of these two fractions, 1/1.2±10%, is required to correct the $DQE_M(0)$.

Čerenkov light photons coming from an individual Compton electron in the glass faceplate will be correlated with one another and may be expected to contribute to the total x-ray noise. For each x-ray that Compton scatters in the glass faceplate, there are two possibilities: (i) The Compton electron does not reach the *a*-Se but the Čerenkov does. In this case, the correlation between the Čerenkov photons will produce additional x-ray noise, however, this noise is small compared to the x-ray noise resulting from electrons passing through the *a*-Se from the following argument. The fraction of x-rays that interact in the glass, given by $1-\exp(-\mu_{glass}d_{glass})$ where μ_{glass} is the attenuation coefficient of glass to 1.25 MeV x-rays (0.057 cm^2/g), is 0.034. Since $A_q = 6.7\times10^{-3}$ (from the Monte Carlo calculation), this implies that only ~20% of the x-ray interactions in the glass produce electrons that reach the *a*-Se. Only ~5% of the x-ray signal is from Čerenkov light, and because five times as many x-rays are required to produce this light, on average, the size of the charge pulse in the a-Se resulting from correlated Čerenkov light is ~1% the size of those resulting from the passage of a high energy electron through the *a*-Se and negligible. (ii) The Compton electron reaches the *a*-Se and contributes to x-ray

noise. In this case, the Čerenkov light simply acts as a weak gain mechanism (~1%) and its effect is also negligible. Thus, Čerenkov generates virtually no additional noise, but 5% additional signal consequently, the measured SNR^2_{out} is 1.05^2 times larger than it would be if there were no Čerenkov. Hence there is a second correction factor of $1/(1.1\pm14\%)$ to the measured $DQE_M(0)$. Applying Eq. 1 and the two correction factors above yielded $DQE_M(0)= 3.3x10^{-3}\pm17\%$.

IV. RESULTS AND DISCUSSION

A. Experimental Results

In Fig. 8, the $MTF_g(f)$ of the glass and $MTF_d(f)$ of the camera, which is actually the product of the MTF(f) of the camera readout and the spread of electrons in the glass, are shown. The two measured MTF(f) curves are essentially identical, implying the only significant loss of resolution in the camera results from the spread of Compton scattered electrons within the glass buildup layer in the Saticon. Also shown is the MTF(f) of the 250 μm slit which was corrected for in the $MTF_g(f)$ and the $MTF_d(f)$. No correction for the Saticon readout was necessary since the MTF(f) of a Saticon is essentially unity[41] out to 10 mm^{-1}.

Fig. 9 shows the noise power spectrum of the Saticon irradiated by ^{60}Co γ-rays at a dose rate of 5.75 R/s along with that of the camera illuminated by light ($NPS_L(f)$). The level of illumination was adjusted so that integration for K+1=33 frames resulted in a signal of 200 mV. The values of $NPS_X(f) >> NPS_L(f)$ for f between 0 and 15 mm^{-1}, indicating that the system is x-ray quantum noise limited over this range. The $NPS_X(f) \approx NPS_q(x)$ is compared to the shape of the response function of the 5 MHz anti-aliasing filter determined using a waveform generator and oscilloscope. Since the two

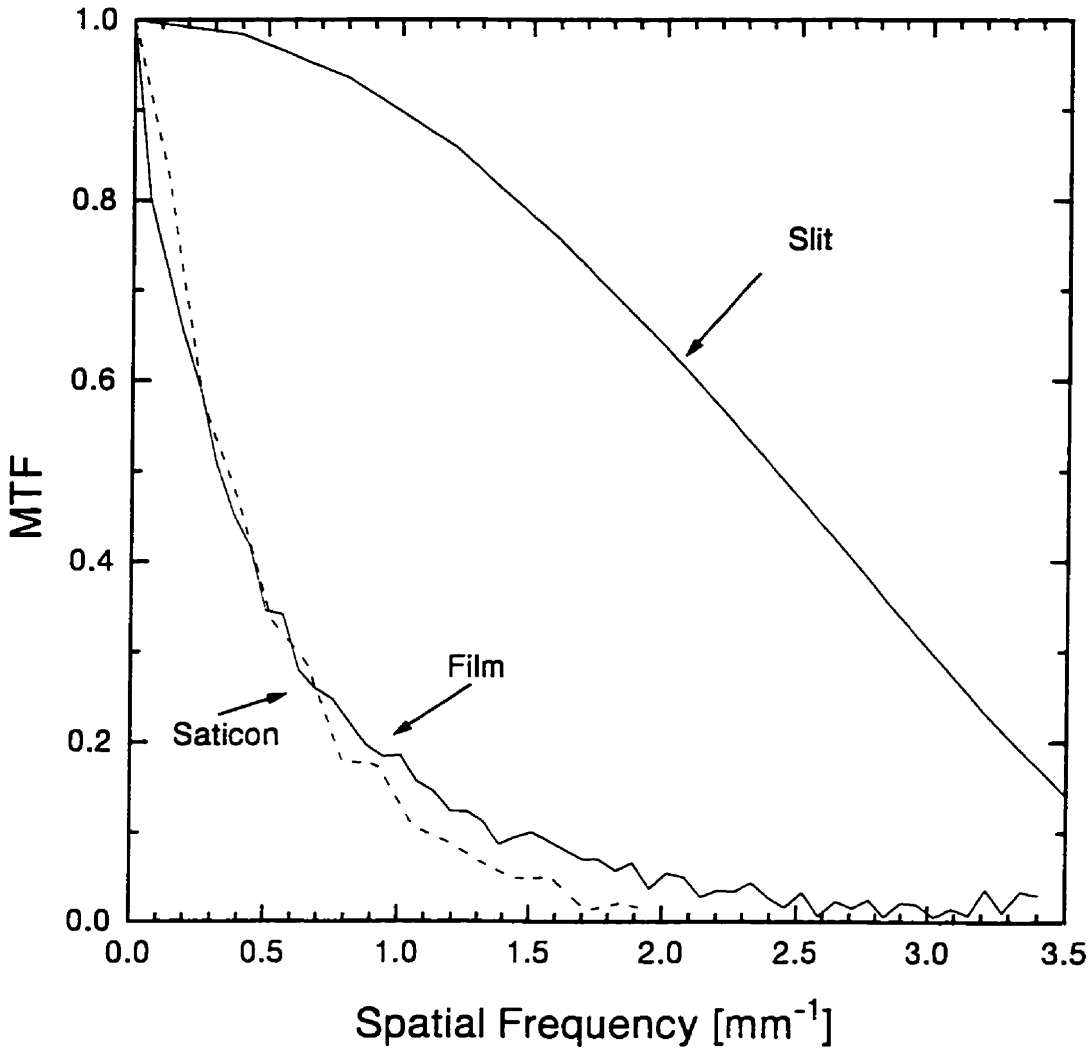

Fig. 8 $MTF_g(f)$ of 2 mm of glass measured with single emulsion film, compared to $MTF_d(f)$ of Saticon with 2.45 mm of glass. The Saticon and film data were corrected for the MTF of the 250 μm slit which is also shown.

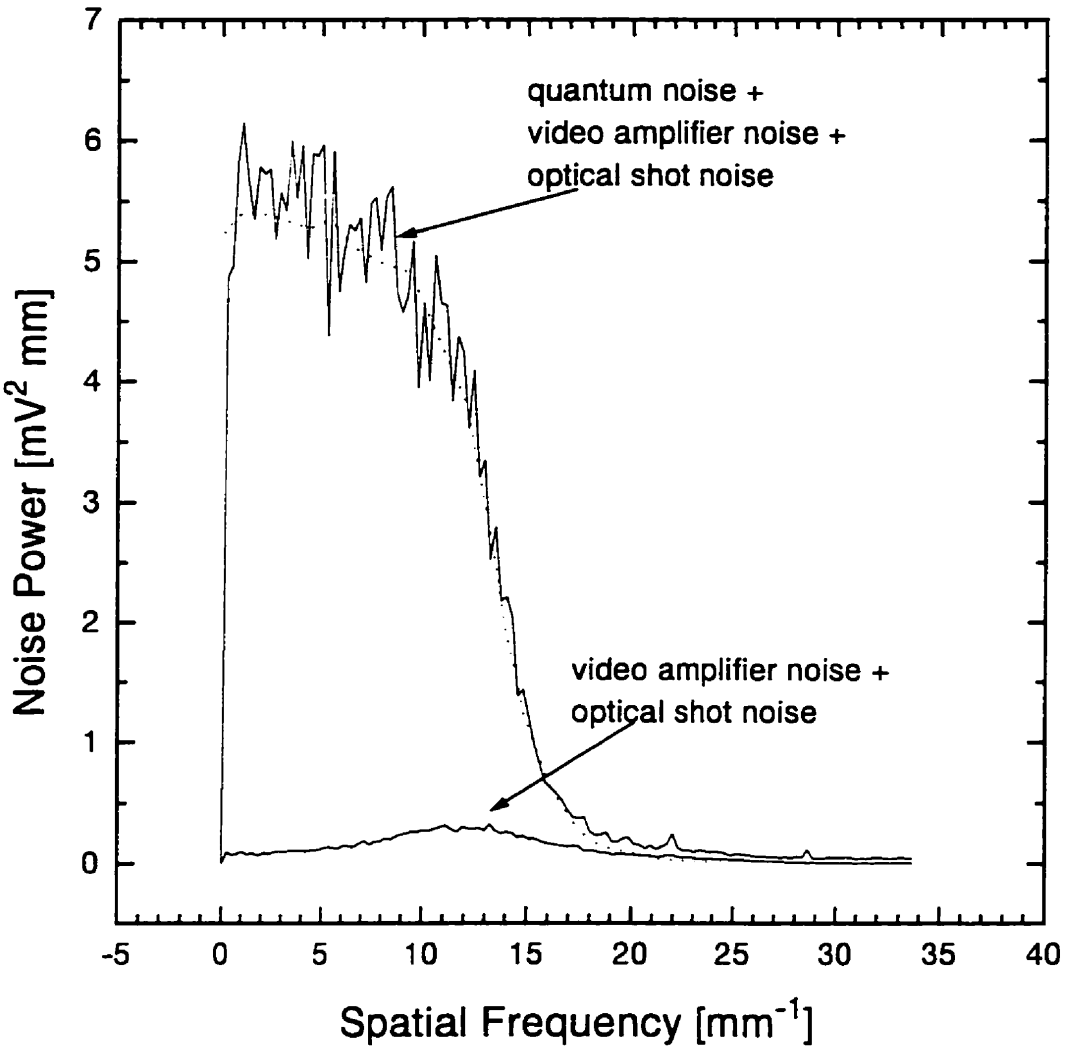

Fig. 9 Measured noise power spectrum for Saticon irradiated with ^{60}Co γ-rays and illuminated with light plotted as a function of spatial frequency. The camera was set to integrate for K+1=33 frames at an exposure rate of 5.75 R/s to yield a signal of 200 mV. Also shown as a dotted line is the response of the 5 MHz anti-aliasing filter (squared).

curves are essentially identical, this demonstrates that the measured $NPS_q(f)$ is shaped by the filter function and the underlying $NPS_q(f)$ is actually constant with f (white) out to at least the maximum frequency measured (5 MHz or ~15 mm-1) and likely beyond, as indicated in section II.C.

B. Verification of Model

The rationale for our experimental measurements was to test the model. The calculated values of the Swank factor (A_s) and the quantum efficiency (A_q) obtained from the PHS(Q) are 0.49 and 6.7×10^{-3} respectively, which lead to a predicted $DQE_p(0) = 3.3 \times 10^{-3} \pm 3\%$. In comparison, the measured zero spatial frequency $DQE_M(0)$, was $3.3 \times 10^{-3} \pm 17\%$.

To extend the measured data as a function of spatial frequency, Eq. 2 was used the obtain the shapes of the curves. The frequency dependence of DQE was obtained directly from the measured data in Figs. 8 and 9. The shape of $DQE_p(f)$ was obtained by equating $MTF_b(f)$ in Eq. 7 to the MTF(f) the glass faceplate alone, $MTF_g(f)$. Fig. 10 shows that the $DQE_p(f)$ and $DQE_M(f)$ are essentially identical.

There would have been a significant discrepancy between measurement and calculation if we neglected to correct for the LET dependent gain ($1/W_\pm$). Specifically, if $W_\pm$ were set to 20 eV instead of using Eq. 6, the DQE(0) would be $DQE_E(0)=2.4 \times 10^{-3}$ instead of the $DQE_p(0)=3.3 \times 10^{-3}$. This is because A_s decreases as the shape of the PHS becomes more skewed. Therefore the correction for the energy dependence of $W_\pm$ on the DQE of an *a*-Se detector is important to ensure that experiment is in agreement with theoretical calculations.

In Fig. 10, the predicted value of DQE, $DQE_p(f)$, is plotted with the measured DQE, $DQE_M(f)$, for the Saticon over the spatial frequency range 0-1 mm^{-1}. There is good agreement between measurement and prediction indicating that the DQE model is accurate. In the next section, we use the DQE model to assess the properties of an *a*-Se based portal imaging system for different system parameters - specifically *a*-Se thickness.

C. Layer thickness considerations

The optimal detector layer thickness will depend upon the specific readout mechanism. There are two types of readouts. The first, in which the *a*-Se layer has only one electrode, the substrate, are called free surface readouts. These systems can only be used for radiography (e.g. laser beam,[42] scanning electrometer probe[43] readouts). Other approaches in which the *a*-Se is sandwiched between two electrodes are called counter electrode readouts and can be used fluoroscopically (e.g. flat panels[8,9]). In this section, the effect of the selenium layer thickness over the range d_{Se} = 5-1000 μm is considered and the effect on the resolution, dynamic range, signal, and DQE(0) determined.

1. Resolution

Recall from section II that as d_{Se} increases, the MTF(f) decreases slightly due to the additional spread of high energy electrons in the *a*-Se. Thus to maximize resolution, d_{Se} should be as thin as possible and the metal plate should be as dense as possible.[32]

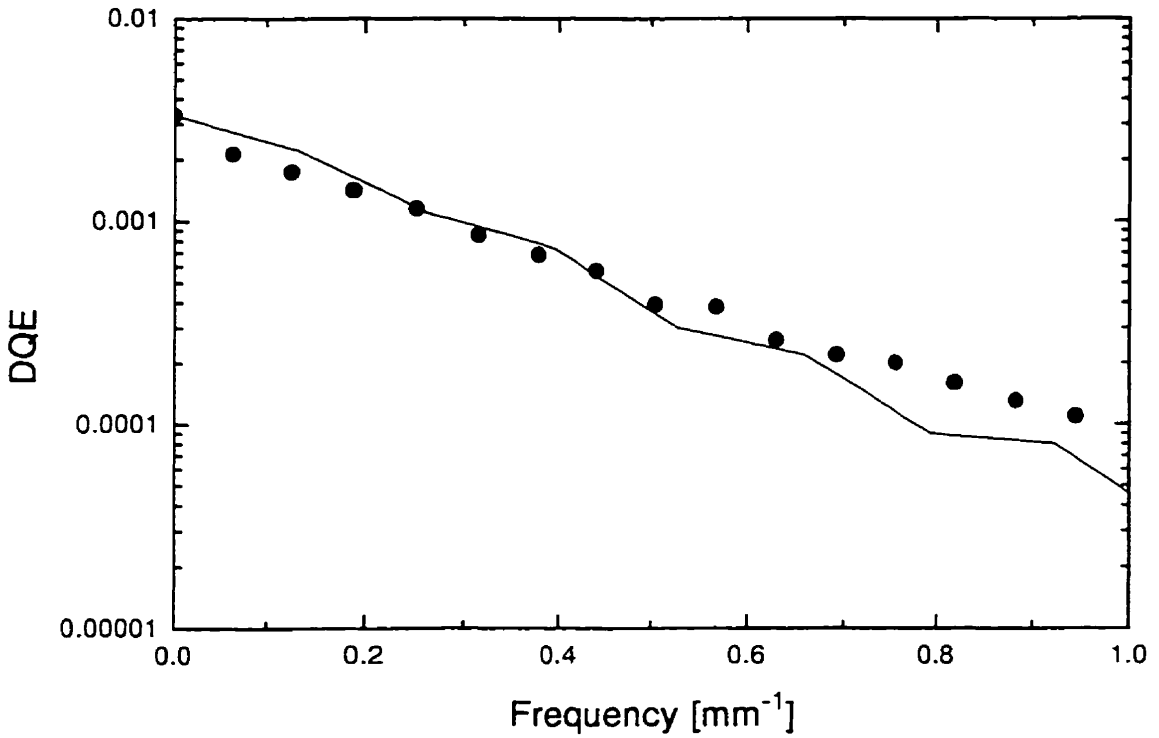

Fig. 10 Comparison of the measured DQE ($DQE_M(f)$), shown as points, and and the calculated DQE ($DQE_p(f)$), shown by the line, of a Saticon irradiated by ^{60}Co γ-rays.

2. Dynamic range

We have previously[13] considered the effect of d_{Se} on the dynamic range of an *a*-Se detector for portal imaging. Briefly, the discharge curves of *a*-Se irradiated by megavoltage x-rays were measured and modelled. For a detector with a free surface, d_{Se} should be ~5-20 μm to produce verification images (~ 100 R) but may be made thicker for localization images (~1 R). This limitation does not exist in readout approaches which employ a counter electrode.

3. Signal

Depending upon the readout method, there are two types of signal which can be measured. These are changes in surface potential, ΔV_{Se}, such as with an electrometer readout[43] and changes in surface charge density, $\Delta\sigma_{Se}$, such as with a laser readout.[42] An *a*-Se layer may be modelled as a parallel plate capacitor which is discharged by x-rays. If d_{plate} is sufficient to produce electronic equilibrium in the *a*-Se, then to a first approximation, ΔV_{Se} should increase quadratically with d_{Se}. On the other hand, if the imaging device reads out $\Delta\sigma_{Se}$, then the signal will increase linearly with d_{Se}. For a 10 μm layer of *a*-Se, the signal[13] is ~ 10^{-5} C cm^{-2} R^{-1} or ~ 1 V/R, both of which are sufficiently large to be accurately measured.

4. Detective quantum efficiency

The DQE model was used to estimate the approximate dependence of the DQE(0) as a function of d_{Se}. We calculated the DQE(0) based upon the PHS(E) only, $DQE_E(0)$. It was compared to the predicted $DQE_p(0)$, which takes into account all LET dependent gain at selected layer thicknesses:

5, 50 and 500 μm. We found that the shapes of the PHS(Q) at 50 and 500 μm were nearly identical to those of the PHS(E) for the reasons outlined in section II.A.2. Fig. 11 shows the A_q, A_s, $DQE_E(0)$ and $DQE_p(0)$ as a function of d_{Se}. The major difference between the DQE_p and DQE_E occurs at small d_{Se} as a result of differences in A_s.

Fig. 12 shows the $DQE_E(0)$ for metal buildup plate + *a*-Se and for a metal buildup plate + phosphor screen irradiated by a 6 MV beam. There is little difference between the transducers since the Compton effect is only weakly dependent on atomic number (due to binding effects).[39] To maximize DQE(0), d_{Se} should be made as large as possible. As the *a*-Se is made thicker, DQE(0) will increase approximately linearly. In a phosphor, the light output falls off due to absorption of light within the thick phosphor[15] and departs from linearity at ~ 500 mg/cm^2. In an analogous way, for a constant field, as the *a*-Se is made thicker, there will be a loss of signal due to charge trapping in the bulk of the *a*-Se. Indeed, for a field of 10 V/μm, the fraction of signal loss with mass thickness of an *a*-Se layer is comparable to that of Gd_2O_2S:Tb phosphor screen.

The applicability of the DQE(f) curves to real imaging systems will also depend upon the gain of the detectors since the signal and quantum noise must be greater than the readout noise of the system. Here we assume that the entire signal (light photons emitted from the screen or charge from the *a*-Se) is collected. We will calculate the energy required to per light photon emitted from the front of the screen, W_p and compare it to the energy required to produce an electron hole pair in *a*-Se, $W_{\pm}$. The intrinsic efficiency[44] (i.e. the fraction of absorbed energy converted to light) of Gd_2O_2S:Tb is ~18%, and the average energy of a green photons is ~ 2.3 eV, thus ~ 13 eV is required to produce an optical photon. However, only ~20% of these photons will be emitted from the screen,[15] thus, W_p~65 eV. In

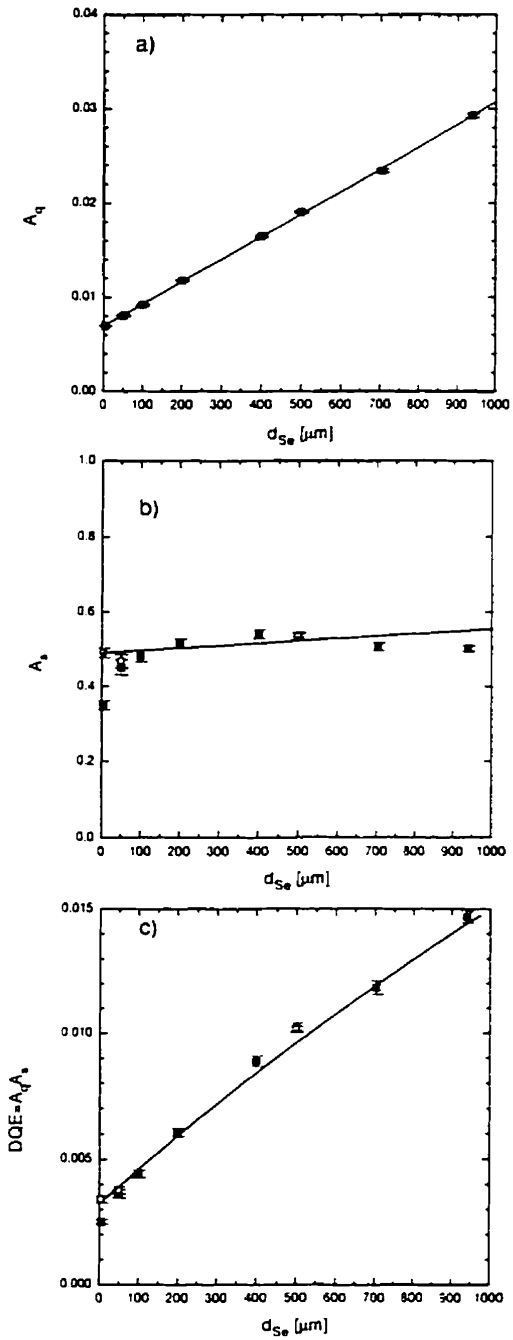

Fig. 11 Calculated image quality parameters at 6 MV for a-Se + 1 mm copper buildup plate as a function of a-Se thickness, d_{Se}. a) Quantum efficiency, A_q b) Swank factor, A_s and c) zero spatial frequency detective quantum efficiency, $DQE_p(0)$) calculated from the CYLTRAN generated PHS(E) are shown as solid squares. In addition, the values from the PHS(c) for 5, 50 and 500 μm a-Se layers are shown as open circles.

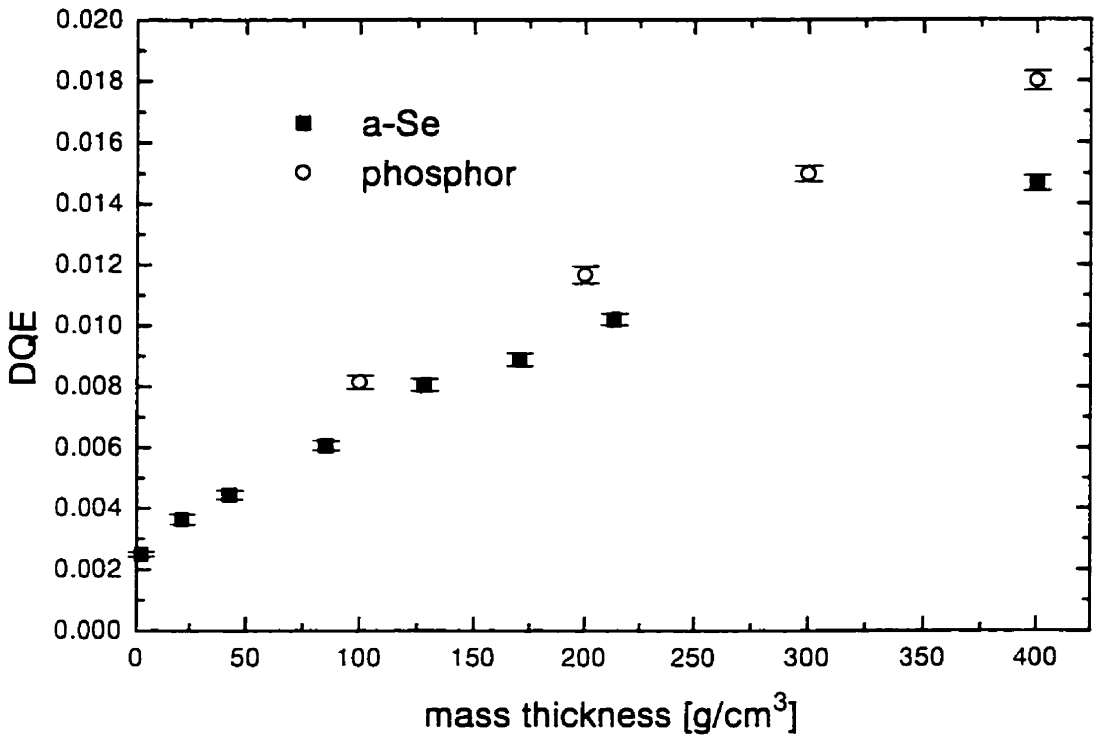

Fig. 12 Calculated values of $DQE_E(0)$ for 1 mm metal plate + a-Se and 1 mm copper plate + phosphor as a function of mass thickness.

comparison, for *a*-Se at 10 V/μm $W_{\pm}$~20 eV. To achieve such a field in a 400 mg/cm^2 *a*-Se layer, ~10 000 V is required which may cause concerns about breakdown of the air. However, by reducing the field to 5 V/μm, would result in a collection efficiency of ~ 77%[21] or an effective $W_{\pm}$ ~ 30 eV. The size of the signal for a practical potential of 5000 V applied across a 1 mm *a*-Se layer is comparable to a phosphor of the same thickness and with better resolution characterstics.

The DQE model was also used to estimate the DQE(f) of a more realistic portal imager. The glass faceplate of the Saticon is not the optimum buildup material because the lateral spread of electrons in it is greater than in higher density materials,[32] resulting in poorer resolution. We therefore modelled the PHS(E) of a 1 mm copper plate + *a*-Se layer irradiated by a 6 MV beam to simulate a more realistic portal imager. Using previously measured[32] MTF(f)s for the copper plate, Eq. 7 and the predicted DQE(f) based upon the PHS(Q), $DQE_p(f)$ was obtained.

In Fig. 13, the $DQE_p(f)$ of two copper + *a*-Se detectors are compared with the measured[32] DQE(f) of the primary metal plate/phosphor detector (400 mg/cm^2 of Gd_2O_2S:Tb), extrapolated to low spatial frequencies using a Monte Carlo calculation, and the measured DQE(f) of a fluoroscopic detector. At low spatial frequencies, the metal plate + phosphor screen has a comparable quantum efficiency to the plate + 400 mg/cm^2 (≈ 1000 μm) *a*-Se layer as expected. The phosphor screen is superior to the 5 μm *a*-Se detector at all spatial frequencies.

Thus, $DQE_E(0)$ and signal size strongly favour thicker *a*-Se, resolution weakly favours thinner *a*-Se and dynamic range strongly favours thin *a*-Se for free surface readouts only. Therefore, for a free surface readout, only if verification images are deemed necessary should thin *a*-Se be considered.

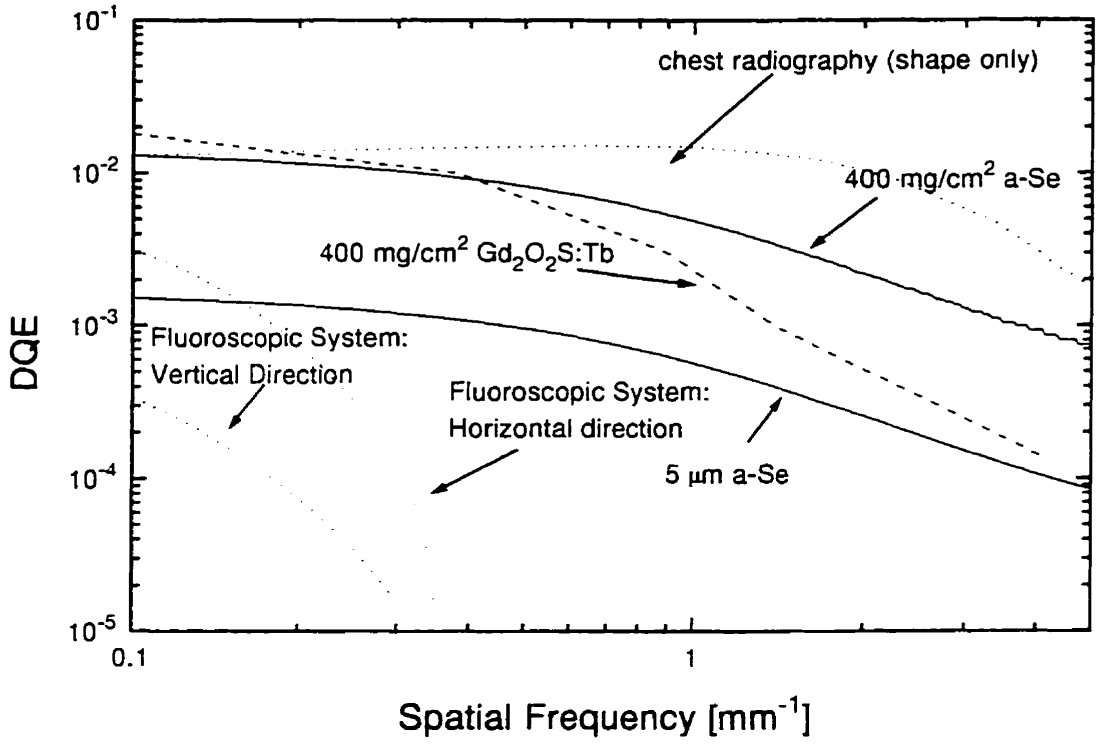

Fig. 13 Comparison of $DQE_p(f)$ to a 6 MV beam of two hypothetical copper plate + a-Se detectors with a 400 mg/cm^2 Gd_2O_2S:Tb detector and with DQE(f) measurements of a fluoroscopic system.[2] The labels horizontal and vertical refer to the direction of the DQE on system with horizontal scanning lines. In addition, the shape of the DQE for a radiographic screen for chest radiography, arbitrarily normalized to be the same as the DQE of the 400 mg/cm^2 a-Se detector at f=0, has been added for comparison.[43]

E. Portal Imaging Implications

Included in Fig. 13 is the shape of a film + screen system for chest radiography.[45] Since the resolution requirements of diagnostic radiography are greater than those of portal imaging, (e.g. visualization of trabeculae in bone may be required in radiography), Fig. 13 shows that the resolution of an *a*-Se sensor does not exceed that of chest radiography but is better than that of metal plate + phosphor screen. In Chapter 1, (section III) we estimated that the required resolution based upon the ability to reproducibly set up a patient is ~ 1 mm. For spatial frequencies between 0 and 1 mm^{-1} the DQE(f) of *a*-Se is comparable to that of a phosphor. Thus, if only 1 mm resolution is required, the choice of which sensor to use will be due to factors other than image quality (e.g. readout method). However, in Chapter 1, we also indicate that greater resolution may permit the detection of edges that will allow unambiguous detection of a landmark. In the future, conformal therapy will require in smaller fields with fewer or smaller landmarks.[46] The better transfer of high spatial frequency information in an *a*-Se detector may permit these landmarks to be detected.[47] This characteristic of an *a*-Se system may prove to be more important in the future as conformal therapy develops. Fig. 13 also shows that the $DQE_p(f)$ of a metal plate + 5 μm detector is less than the DQE(f) of a metal plate + phosphor detector, which implies that a free surface readout cannot produce verification images of comparable quality to those that can be obtained from a thicker phosphor being read out in an optimal fashion. Thus ideally, a free surface readout should be limited to only producing localization images.

V. CONCLUSIONS

In this chapter, we modelled, using a Monte Carlo simulation of a pulse height spectrum as a function of energy deposited, the DQE(0) of an *a*-Se based portal imaging system using a 1 mm copper buildup plate and a range of thicknesses of *a*-Se. The DQE model was validated by measurement on a vidicon with a 5 μm *a*-Se layer irradiated with 1.25 MeV gamma rays. After taking into account the non-linear gain associated with high energy deposition events in the charge scored pulse height spectrum, good agreement was found between the measured and calculated DQE(f). The hypothetical DQE(f) of an *a*-Se detector was then compared with existing metal plate + phosphor detectors and fluoroscopic systems. It was found that a metal plate + *a*-Se layer is capable of producing portal images superior to existing systems and at least comparable to systems that employ a metal plate + equivalent mass thickness of phosphor as the primary x-ray detector.

REFERENCES

1. M.G. Herman, R.A. Abrams, and R.R. Mayer, "Reply to editorial by Dr. Shalev," *Int. J. Radiat. Oncol. Biol. Phys.*, **28**, 1047 (1994).

2. P. Munro, J.A. Rawlinson, and A. Fenster, "Therapy imaging: A signal-to-noise analysis of a fluoroscopic imaging system for radiotherapy verification," *Med. Phys.*, **17**, 763-772 (1990).

3. W. Swindell, "The lens coupling efficiency in megavoltage imaging," *Med. Phys.*, **18**, 1152-1153 (1991).

4. J.-P. Bissonnette, I.A. Cunningham, D.A. Jaffray, A. Fenster and P. Munro, " A quantum accounting and detective quantum efficiency analysis for video-based portal imaging" (in Press, *Med. Phys.* 1996)

5. D.W. Mah, J.A. Rowlands, and J.A. Rawlinson, "Measurement of quantum noise in fluoroscopic systems for portal imaging," *Med. Phys.*, **23**, 231-238 (1996).

6. M. Van Herk, "Physical aspects of a liquid-filled ionization chamber with pulsed polarizing voltage," *Med. Phys.*, **18**, 692-702 (1991).

7. J.W. Boag, "Xeroradiography," *Phys. Med. Biol.*, **18**, 3-37 (1973).

8. W. Zhao and J.A. Rowlands, "X-ray imaging using amorphous selenium: Feasibility of a flat panel self-scanned detector for digital radiology," *Med. Phys.*, **22**, 1595-1605 (1995).

9. D.L. Lee, L.K. Cheung, and L.S. Jeromin, "A new digital detector for projection radiography," *Proc. SPIE*, **2432**, 237-249 (1995).

10. L.E. Antonuk, J. Yorkston, W. Huang, H. Sandler, J.H. Siewerdsen and Y. El-Mohri, "Megavoltage imaging with a large-area, flat panel, amorphous silicon imager," *Int. J. Radiat. Oncol. Biol. Phys.*, **36**, 661-672 (1996).

11. D.M. Korn, S.P. Johnson, O.L. Nelson, and J. Ziegler, "A method of electronic readout of electrophotographic and electroradiographic images," *J. Appl. Photo. Eng.*, **4**, 178-182 (1978).

12. U. Schiebel, W. Hillen, and T. Zaengel, "Image quality in selenium-based digital radiography,"*SPIE Medicine XIV/ PACS IV*, **626**, 176-184 (1986).

13. D. Mah, J.A. Rowlands, and J. A. Rawlinson, "Portal imaging using amorphous selenium: Sensitivity to x-rays from 40 kVp to 18 MV" (submitted to Medical Physics 1997)

14. H. Wang, B.G. Fallone, and T. Falco, "Monte Carlo simulations of a metal/a-Se portal detector," *Radiotherapy and Oncology*, **30**, 291-297 (1996).

15. T. Radcliffe, G. Barnea, B. Wowk, R. Rajapakshe, and S. Shalev, "Monte Carlo optimization of metal/phosphor screens at megavoltage energies," *Med. Phys.*, **20**, 1161-1169 (1993).

16. D.A. Jaffray, J.J. Battista, A. Fenster, and P. Munro, "Monte Carlo studies of x-ray energy absorption and quantum noise in megavoltage transmission radiography," *Med. Phys.*, **22**, 1077-1088 (1995).

17. J.C. Dainty and R. Shaw, *Image Science*, (Academic Press, New York, 1974).

18. R.K. Swank, "Absorption and noise in x-ray phosphors," *J. Appl. Phys.*, **44**, 4199-4203 (1973).

19. R. Fahrig, J.A. Rowlands and M.J. Yaffe, "X-ray imaging with amorphous selenium: Detective quantum efficiency of photoconductive receptors for digital mammography," *Med. Phys.*, **22**, 153-160 (1995).

20. S.O. Kasap, "Photoreceptors: The selenium alloys" in *Handbook of Imaging Materials* edited by A.S. Diamond, (Marcel Dekker Inc., New York, 1991) pp. 329-377.

21. I. Blevis, D. Hunt, and J.A. Rowlands, "Measurement of x-ray photogeneration gain and fluctuations in amorphous selenium," (to be submitted, 1997).

22. J. Halbleib, "Structure and operation of the ITS code system," in *Monte Carlo Transport of Electrons and Photons*, edited by T. Jenkins, W.R. Nelson and A. Rindi (Plenum Press, New York, 1988) pp. 249-262.

23. D.W.O. Rogers, G.M. Ewart, A.F. Bielajew and G. Van Dyk, "Calculation of electron beam contamination in a ^{60}Co therapy beam," in *"Proceedings of the IAEA International Symposium on Dosimetry in Radiotherapy"* vol. 1, (IAEA, Vienna, 1988) pp. 303-312.

24. R. Mohan and C. Chui, "Energy and angular distributions of photons from medical linear accelerators," *Med. Phys.*, **12**, 592-597 (1985).

25. H.E. Johns and J.R. Cunningham, *The Physics of Radiology*, 4th ed. (Thomas, Springfield, 1983) p. 734

26. *ICRU Report 37 "Stopping powers for electrons and positrons,"* (International Commission on Radiation Units and Measurements, Bethesda, MD, U.S.A., 1984).

27. J. Halblieb, Sandia National Laboratories, New Mexico, U.S.A. (private communication).

28. G. Lubberts, "Random noise produced by x-ray fluorescent screens," *J. Opt. Soc. Am.*, **58**, 1475-1483 (1968).

29. W. Que and J.A. Rowlands, "X-ray imaging using amorphous selenium: Inherent spatial resolution," *Med. Phys.*, **22**, 365-374 (1995).

30. T. Oguro, I. Kashima, M. Kanno, T. Higashi, T. Uehara, and B.T. Williams, "Ultra high resolution digital xeroradiography for x-ray microscopic detector." *Med. Imag. Technol.* **7**, 279-280 (1989).

31. H. Wang, T. Falco, and B.G. Fallone, " A metal screen-amorphous selenium based image receptor in megavoltage portal imaging (abstract)," *Med. Phys.*, **23**, 1130 (1996).

32. P. Munro, J.A. Rawlinson, and A. Fenster, " Therapy Imaging: A signal-to-noise analysis of metal plate/film detectors," *Med. Phys.*, **14**, 975-984 (1987).

33. J.A. Rowlands, "Television camera design and specification," in *Specification, Acceptance Testing, and Quality Control of Diagnostic X-ray Imaging Equipment*, edited by J.S. Seibert, G.T. Barnes, and R.G. Gould, (American Institute of Physics, Woodbury, New York, 1994) pp. 461-482.

34. N. Goto, Y. Isozaki, K. Shidara, E. Maruyama, T. Hirai, and T. Fujita, "Saticon: a new photoconductive camera tube with Se-As-Te target," *IEEE Trans. Electron. Dev.*, **21**, 662-666 (1974).

35. J.A. Rowlands and G. DeCrescenzo, "Wiener noise power spectra of radiological television systems using a digital oscilloscope," *Med. Phys.*, **17**, 58-64 (1990).

36. S.F. deBoer, A.S. Beddar, and J.A. Rawlinson, "Optical filtering and spectral measurements of radiation-induced light in plastic scintillation dosimetry," *Phys. Med. Biol.*, **38**, 945-958 (1993).

37. M. Danos, "Cerenkov radiation," in *Encyclopedia of Physics*, 2nd ed., edited by R.G. Lerner and G.L. Trigg, (VCH, New York, 1991) pp. 130-131.

38. *CRC handbook of tables for applied engineering science*, second ed., edited by R.E. Bolz and G.E. Tuve, (CRC Press, Boca Raton, 1973).

39. H.E. Johns and J.R. Cunningham, *The Physics of Radiology* (Thomas, Springfield, 1983) p.722, pp. 181-183

40. J.A. Rowlands, K.S. Schulenburg, and G. DeCrescenzo, "A light source for testing radiological television cameras," *Med. Phys.*, **16**, 1-6 (1989).

41. H. Rougeot, "Direct x-ray photoconversion processes," in *AAPM Medical Physics Monograph Number 11: Digital Imaging*, edited by W.R. Hendee and J. H. Trueblood, (Medical Physics Publishing, Madison, 1993) pp. 49-96.

42. D. Mah, J.A. Rowlands and J.A. Rawlinson, "Portal imaging using amorphous selenium: Demonstration of image quality using a photo-induced discharge approach (abstract)" *Med. Phys.* **23**, 1491-1492 (1996).

43. H. Wang, T. Falco, and B.G. Fallone, " A metal screen-amorphous selenium based image receptor for megavoltage portal imaging (abstract)" *Med. Phys.*, **23**, 1130 (1996).

44. T.S. Curry, J.E. Dowdey, and R.C. Murry, *Christensen's Physics of Diagnostic Radiology*, 4th ed. (Lea and Febiger, Philadelphia, 1990) p.125.

45. P.C. Bunch, R. Shaw, and R.L. Van Metter, "Signal-to-noise measurements for a screen-film system," *Proc. SPIE*, **454**, 154-163 (1984).

46. J.M. Balter, K.L. Lam, H.M. Sandler, J.F. Littles, R.L. Bree and R.K. Ten Haken, "Automated localization of the prostate at the time of treatment using implanted radiopaque markers: technical feasibility," *Int. J. Radiat. Oncol. Biol. Phys.*, **33**, 1281-1286 (1995).

47. D.E. Pearson, *Transmission and Display of Pictorial Information* (Pentech, London, 1975).

Chapter 5

Portal Imaging with Amorphous Selenium: Demonstration of Image Quality using a Photoinduced Discharge Method

"One picture is worth a thousand words"

- Royal Baking Powder Street Car Advertisement, 1927

Part of this chapter was presented as a "Works in Progress" at the 1996 Annual AAPM meeting.

I. INTRODUCTION

In this chapter, a method called the photoinduced discharge method is used to read out the latent charge image on the surface of an *a*-Se layer irradiated by megavoltage photons. Images of contrast-detail phantoms, anthropomorphic phantoms and patients are presented.

II. METHOD

A. PID Readout

We used a megavoltage beam to produce a latent image and read it on a large area scanner (~ 20 cm x 20 cm) using the air gap photoinduced discharge (PID) method, which has been described in detail elsewhere.[1,2,3] This readout approach has previously been used for mammography but this is the first application to portal imaging. In addition, in this chapter, the only clinical (i.e. patient) images ever produced with such a scanner are presented.

A corotron charged 150 μm *a*-Se sample was irradiated using a 6 MV beam through its 2 mm aluminum substrate with an additional 1 mm copper buildup plate in a xeroradiographic cassette. As shown in Fig. 1, to readout the charge image, a transparent probe was brought very close (~ 150 μm) to the free surface. The proximity of the positive charges on the free surface of the *a*-Se to the probe attracted negative charges to the surface of the probe until there was equilibrium between the probe, substrate and *a*-Se (i.e. $\sigma_{Se}=\sigma_{Al}+\sigma_{probe}$ where σ refers to charge density). Next, a pulsed blue laser beam was scanned across the probe and the *a*-Se plate. Since the blue laser light causes the *a*-Se to conduct, the surface charges beneath the laser spot flowed through the bulk of the *a*-Se and out

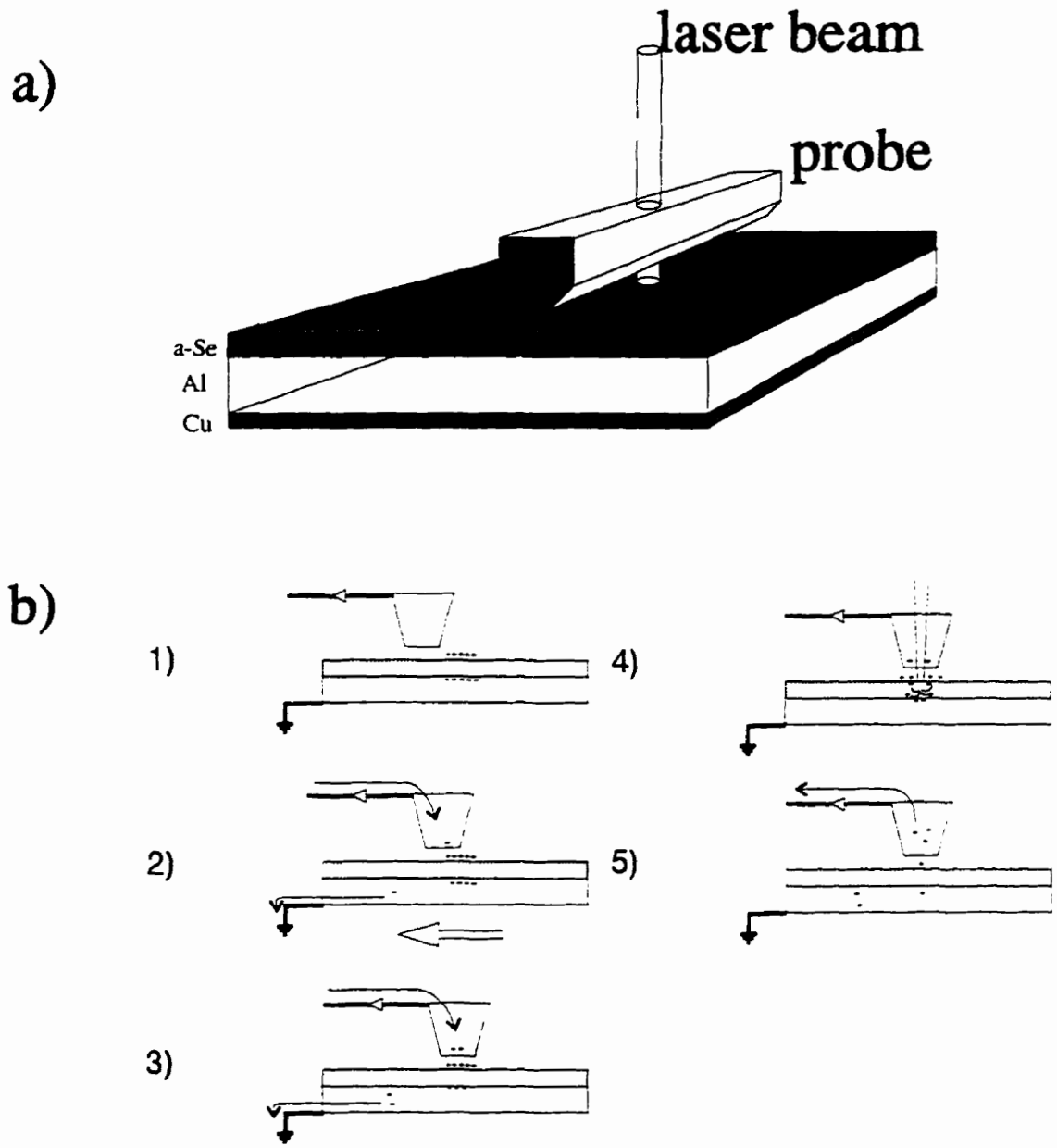

Fig. 1 Illustration of how the PID readout functions. (a) A transparent probe is brought close to the free surface and capactively coupled to the a-Se. A scanning blue laser beam reads out the image pixel by pixel. (b) In (1-3) the probe is brought over the charged a-Se surface. As the a-Se moves under the probe, there is a redistribution of charges as electrons flow into the grounded probe and out of the substrate until an equilibrium is reached. In (4) a laser discharges the a-Se resulting in a charge flow (signal) out of the probe as shown in (5).

through the substrate. Consequently, the individual counter charges on the surface of the probe flowed out and were collected by a preamplifier. The next laser pulse was set to be incident on the neighbouring position and the process was repeated until a line was read out. The plate was then translated relative to the probe so that the laser raster scanned the entire charge image. Note that the PID readout is a "free surface" readout as described in Chapters 3 and 4. Thus, this approach is limited in terms of dynamic range and only suitable for producing localization images.

B. Image subjects

A contrast-detail phantom can be used determine limiting contrast at a certain object size (detail) which are indicative of signal-to-noise ratio and resolution. We chose to use the Las Vegas phantom, a standard tool for assessing portal image quality. The phantom consists of a 2 cm thick aluminum block with holes of differing diameters and depths such that they form 5 columns and 6 rows. The hole diameters and depths are listed in Table I. Operationally, the phantom is used to determine both how shallow (contrast) and narrow (detail) a hole can be detected. Ideally, a portal imager should permit the detection of all the holes with as little dose as possible.

A head phantom was also imaged. This anthropomorphic phantom consists of a half skull imbedded in tissue-mimicking plastic. The mouth of the phantom had a screw in it to fasten the jaw to the skull. In addition, images of the head and neck of a patient undergoing treatment using a lateral parallel-opposed pair of beams were acquired using both film and *a*-Se.

Table I

Hole Diameter [mm]	Hole Depth [mm]
1	0.51
2	1
4	2
7	3.2
10	4.8
15	

Table I Description of Las Vegas contrast detail phantom. The holes are drilled in a block of aluminum 2 cm thick and 15 cm square.

For both sets of phantom images, the phantom was placed in contact with the detector. For the clinical images, the detector was ~ 15 cm from the patient and oriented normal to the beam.

C. Image Processing

Some limited image processing was performed to reduce the effect of the artifacts on the images. First, vertical lines artifacts resulted when a speck of dust which absorbed some of the laser light on the probe and traced out a line as the plate was translated beneath the probe. These artifacts were removed by taking a uniform horizontal strip at the edge of the image and dividing all pixel values along each column by the average of the pixel values of each column in the strip. Second, because the probe was not perfectly parallel to the surface of the probe, the coupling between a uniformly charged plate and the probe resulted changed across the length of the probe. This resulted in a small change in the gain of the image from left to right. A linear interpolation across the image was used to "flatten" out the image. This second correction was only applied to the contrast detail images.

III. RESULTS

In Fig. 2, images of the contrast detail phantom exposed using a 6 MV beam from a Siemens Mevatron linear accelerator are shown. Figs. 2(a) and (b) show images from the existing clinical modalities. Fig. 2(a) is a high quality film image taken using commercial metal plate cassettes* irradiated to ~2 cGy.** The radiograph was digitized to ~ 100 μm pixels and processed by altering

---

* EG-1 film in a localization cassette developed in a X-omat multiloader 300 film processor (all are Kodak products)

**Here dose refers to dose to water for a 10 cm x 10 cm field size at a depth of 1 cm.

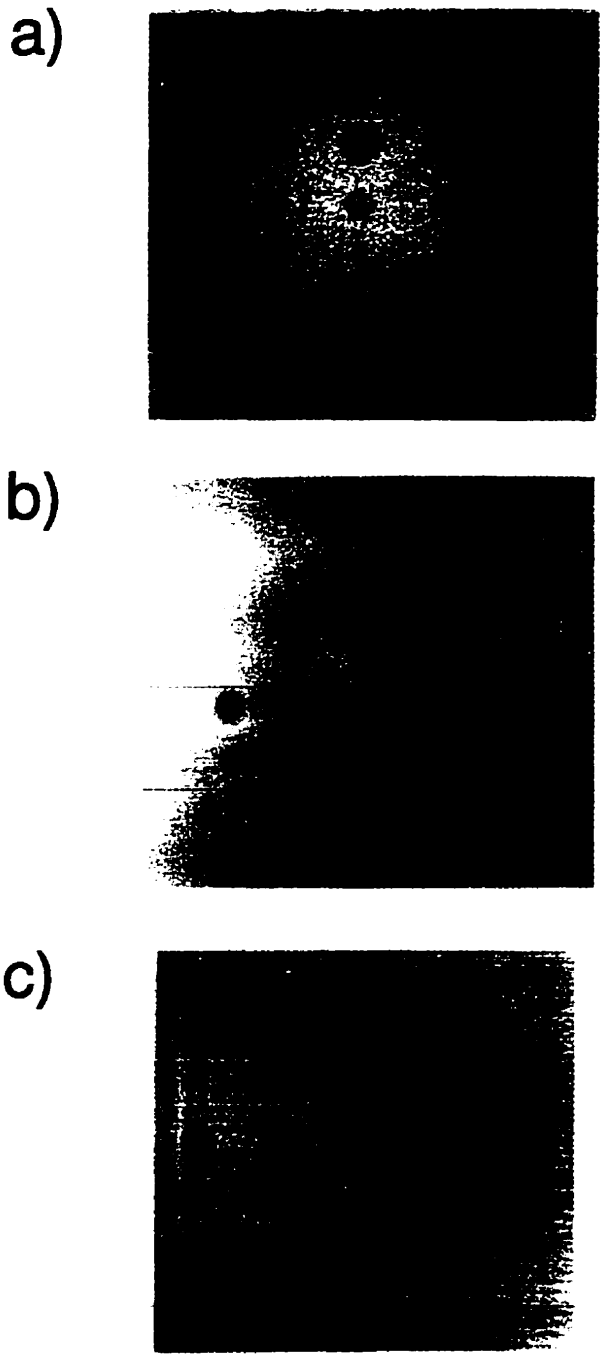

Fig. 2 Images of "Las Vegas" contrast detail phantom. All images were made using a 6 MV beam. (a) A portal film produced using ~2 cGy (to water) digitized using a Konica film digitizer (~100 micron pixels). (b) A "verification" image from a fluoroscopic portal imaging system (~ 30 cGy). The distortion of the circles occured as a result of printing the 4 to 3 aspect ratio of the frame grabbed image to square pixels. (c) An a-Se image produced using ~5 cGy and read out using the PID system (100 micron pixels).

contrast and brightness (window and level) to enhance its display. The image quality of the digitized radiograph compares favourably to the image from a Siemens Beamview Plus fluoroscopic system shown in Fig. 2(b) produced using ~ 30 cGy. The smallest, highest contrast holes in the film image are visible, that is those in the sixth row on the left most column, but they are not visible in the image from the fluoroscopic system. Thus, the image quality from film is superior to that from this clinical fluoroscopic system.[4] Fig. 2(c) shows an image from the PID readout of an *a*-Se plate irradiated to ~5 cGy by a 6 MV beam. Clearly, more holes can be seen in the PID image than those produced using either of the other imaging modalities. Indeed, it is possible to see nearly all the holes in the phantom. (Only the shallowest hole with the smallest diameter remained undetectable). This is true despite the fact that the imaging sensor is not optimized in terms of *a*-Se thickness, the buildup material composition is not optimal and the readout process still has scanning artifacts that could be reduced. Moreover, the edges of the holes remain very sharp indicating that there is little blurring. In contrast, the image from the fluoroscopic system is not as sharp due to blurring in the metal plate, phosphor, lens and camera as described in Chapter 2.

In part because the PID readout system is still undergoing development, there are a variety of different artifacts on the image in Fig. 2(c). The dark band on the bottom of the image results from additional transmission through a thinner part of the treatment couch and the dark rectangular area on the left side results from the cassette which has a thinner plastic portion. The horizontal line artifacts are possibly due to imperfect stage translation, system or structural noise and should be removable with further work. The dominant structure of the noise artifacts implies the images are not yet quantum limited. Thus, Fig. 2(c) shows the promise of *a*-Se for portal imaging, but it does not represent the ultimate limit of its performance.

Fig. 3(a) shows an image of the head phantom taken using film and digitized and processed in the same manner. Fig. 3(b) shows the corresponding image taken using the PID system. The *a*-Se image is raw and a block of lead is visible on the bottom of the image. Figs. 4(a) and (b) show the same image of the lateral head and neck of a patient. All images were produced using doses of less than 5 cGy to the patient.

IV. DISCUSSION

Although the images of the contrast detail phantom show a dramatic improvement in quality, measured in terms of the number of circles detectable, the images produced of the anthropomorphic objects (i.e. the head and neck) are more difficult to interpret and do not appear dramatically better. This is due to two effects. First, because they are images of the head, the large amount of bone (and its relatively high contrast) makes it relatively easy to identify all the landmarks. In the image of the contrast-detail phantom, the contrast is very low and improvements in the signal to noise ratio are readily seen. Second, the circles in the contrast detail phantom are simple and follow a pattern whereas the image of the skull is far more complex. The noise produced by the image artifacts on the PID image will disrupt the interpretation of these complex images much more than the image of the contrast-detail phantom.

If the PID system were made quantum noise limited, one intriguing possible application is to determine what resolution is required for portal images from an image quality perspective (as opposed to a radiobiological perspective). Previously, electronic portal imagers have had a fixed pixel size and the requirements for pixel size in portal imaging were essentially "guesstimates" and led by engineering. However, with this readout system, the pixel size can easily be changed by altering the

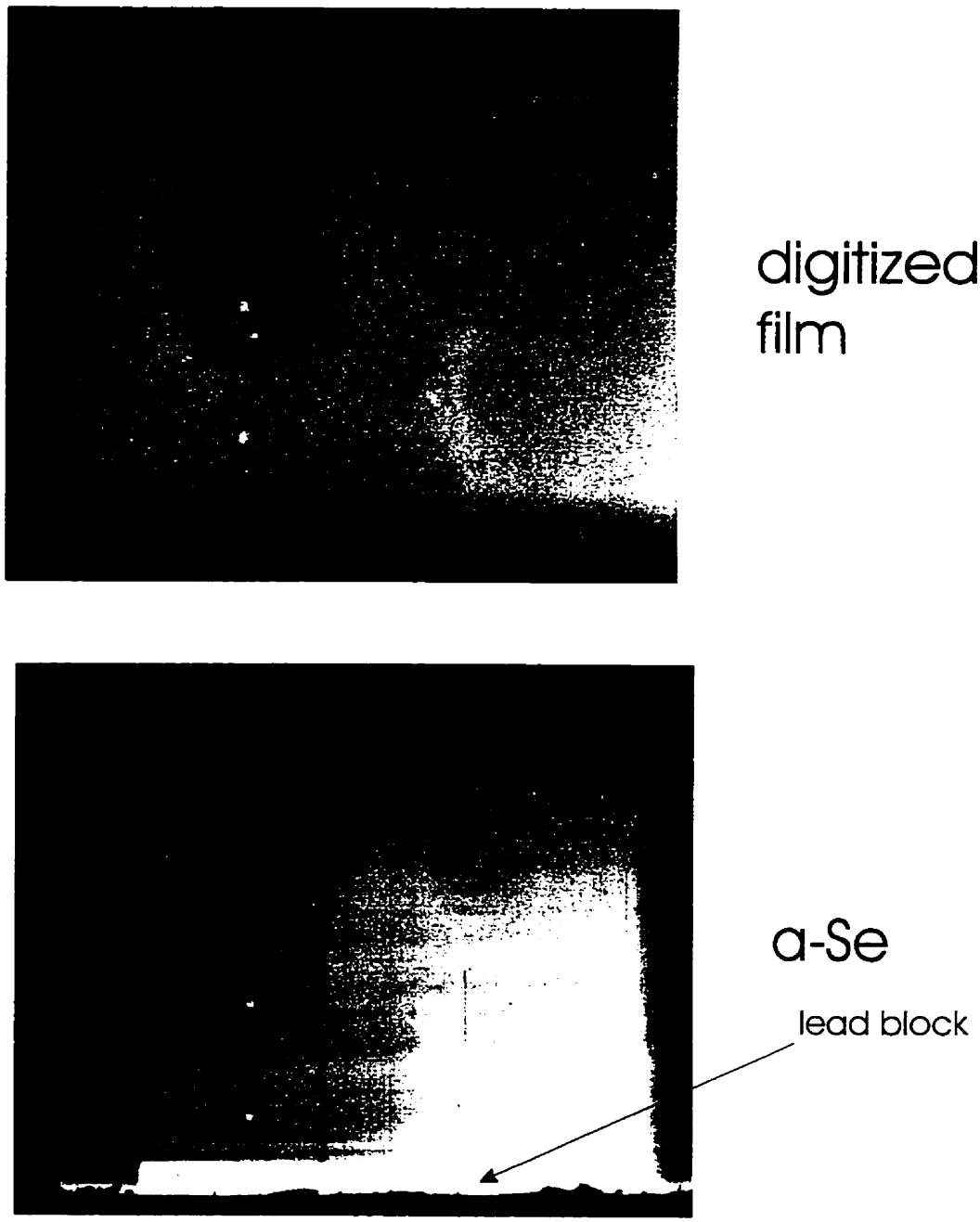

Fig. 3 Images of anthropomorphic phantom of half a head. Both images were produced using a 6 MV beam and less than 5 cGy radiation.

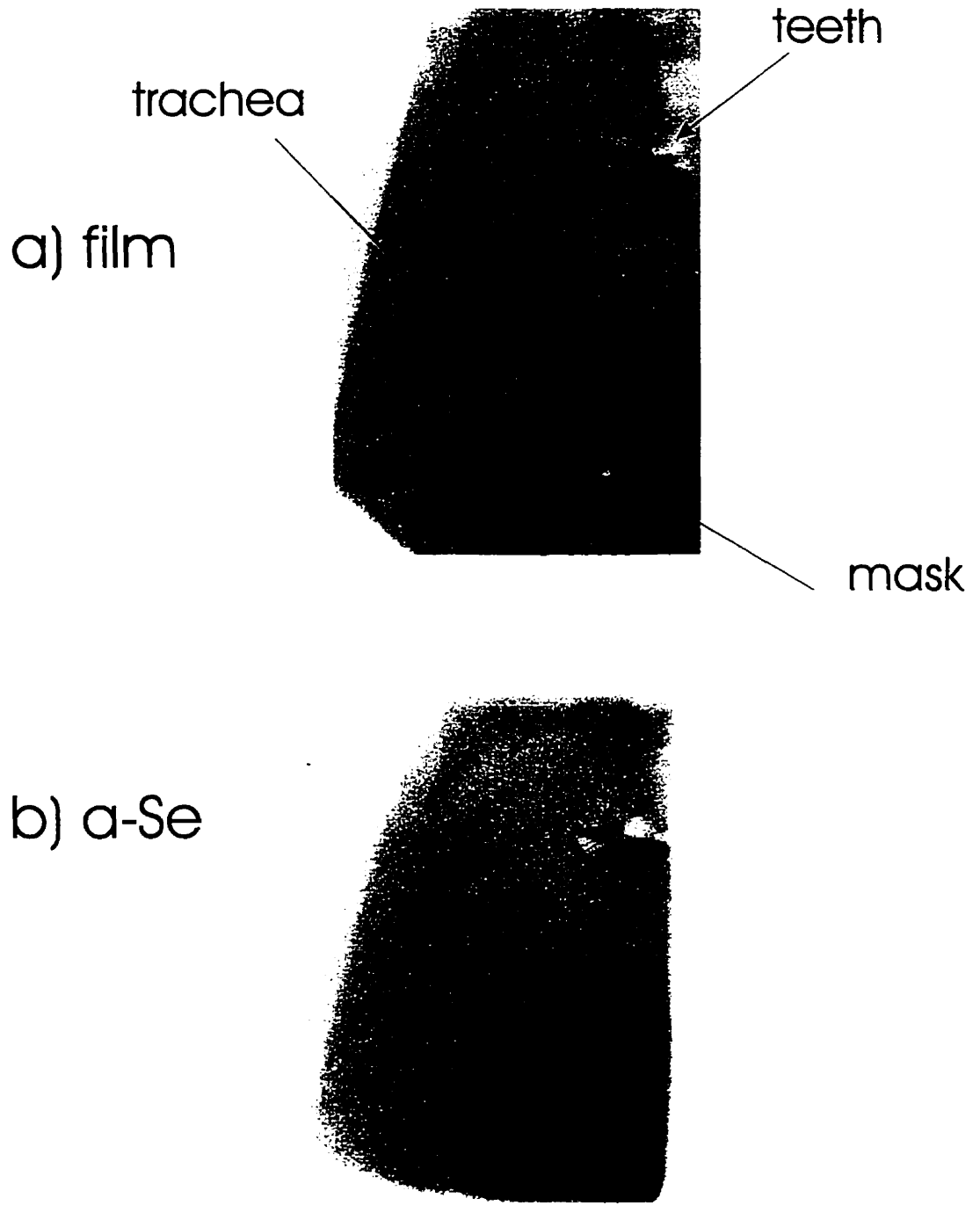

Fig. 4 Comparison of digitized portal film and a-Se image of patient head and neck undergoing radiation therapy. The images are the profile of a patient facing toward the right of the page. Both images were produced using 6 MV x-rays. The dose to the patient was ~ 3cGy for the film and ~ 4 cGy for the a-Se image. The lead marker placed on the film cassette produced the letters LLAT to indicate that this treatment was a left lateral field.

size of the laser spot. Thus, different pixel sizes could be imaged and viewed by expert observers over a variety of clinical sites to determine the largest pixel size acceptable. The images in Fig. 2 illustrate that the latent charge image on the free surface of the *a*-Se is superior to those from existing systems. Not only is the *a*-Se layer more sensitive from a contrast perspective, but the exquisite resolution that is produced using *a*-Se may permit the edges of a bone, or other critical structures to be seen. Furthermore, the resolution can be improved. The combination of copper, aluminum and *a*-Se detector used in the PID system is not optimal. Currently, Fallone and his colleagues[5] are working with Noranda Advanced Materials to test *a*-Se bonded to different substrates. The use of a higher density substrate (buildup material) should improve the resolution.[6] Additionally, since the *a*-Se is only ~150 μm thick, the sensitivity of the system can be increased by a factor of ~3 by increasing the thickness to 500 μm. This implies that all the *a*-Se images could be obtained with as little as 1 cGy of radiation.

V. CONCLUSIONS

This chapter has shown that the latent image on the surface of the *a*-Se is better than that that can be obtained from film or an existing electronic portal imaging device. Moreover these images can be obtained instantaneously unlike film. Currently the PID system takes approximately seven minutes to read out a plate, but there is little reason that this cannot be reduced by for instance, increasing the size of the pixels. Nevertheless, it is unlikely that this particular approach will be successful for portal imaging because it cannot provide real time feedback. Clearly the development of an artifact free, real time readout method with low noise (i.e. quantum noise limited) is required to obtain an optimal image. Nevertheless, the clinical images do show promise and further development of an appropriate readout system is the next step. Some of these readout approaches are outlined in the next chapter.

REFERENCES

1. J.A. Rowlands and D.M Hunter, "X-ray imaging using amorphous selenium: Photoinduced discharge (PID) readout for digital general radiography," *Med. Phys.*, **22**, 1983-1996 (1995).

2. J.A. Rowlands and D.M. Hunter, "X-ray imaging using amorphous selenium: A photoinduced discharge readout method for digital mammography," *Med. Phys.* **18**, 421-431 (1991).

3. J.A. Rowlands and J.E. Taylor, "Design of a laser scanner for a digital mammography system," *Med. Phys.*, **23**, 755-758 (1996).

4. There is variation between the image quality of portal imaging systems from the same manufacturer as shown in:

   S. Shalev, K.B. Luchka, and R. Rajapakshe, "Image quality in electronic portal imaging devices: A quantitative comparison (abstract)," *Med. Phys.*, **23**, 1131-1132 (1996).

5. H. Wang, T. Falco, and B.G. Fallone, "A metal screen-amorphous selenium based image receptor for megavoltage portal imaging (abstract)," *Med. Phys.*, **23**, 1130 (1996).

6. P. Munro, J.A. Rawlinson, and A. Fenster, "Therapy imaging: A signal-to-noise analysis of metal plate/film detectors," *Med. Phys.*, **14**, 975-984 (1987).

Chapter 6

Summary and Future Directions

"After a year's research, one realises that it could have been done in a week."

- [Sir] William Henry Bragg 1862-1942

I. SUMMARY

This thesis explored the potential utility of *a*-Se for portal imaging compared to existing systems. Chapter two described the measurement of quantum noise in a phosphor based fluoroscopic portal imaging system. A novel approach was established for measuring the x-ray quantum noise in fluoroscopic systems and applied to an experimental fluoroscopic system. We determined how far the system was from being quantum noise limited and consequently to what extent it was possible to reduce the secondary quantum sink, and hence improve the image quality, by better optical coupling. It was demonstrated that although it was possible in principle to modify existing fluoroscopic systems to the point where they were quantum noise limited at low spatial frequencies, the only way to make them quantum noise limited at high spatial frequencies was to reduce the demagnification, i.e., viewing a smaller portion of the phosphor screen. Unfortunately, this is not clinically acceptable since there is demand for bigger, not smaller, fields of view.[1] The radiobiological and image quality considerations in Chapter 1 indicated that the resolution must be at least 2 mm, but the results of Chapter 2 show that even if they were made quantum noise limited, existing fluoroscopic systems are only able to produce resolution of ~ 5 mm (i.e. spatial frequencies of ~0.2 mm^{-1}). Moreover, current systems are vastly dominated by video noise and not quantum noise. Thus, one conclusion of this work is that an improved portal imaging system design is required.

One very attractive possible approach is the use of flat panel imaging systems since these systems have direct coupling and therefore do not have a secondary quantum sink. Additionally, these systems are compact and therefore much less obtrusive than fluoroscopic systems. There are two possible sensors being considered for flat panel imagers: the phosphor screen and the photoconductor, amorphous selenium. The physics of fluoroscopic screens for portal imaging has been investigated

thoroughly,[2,3,4,5,6] and is relatively well understood. However, the signal and noise properties of *a*-Se for portal imaging had not, until this work, been quantitatively understood. In Chapter 3, the signal properties were examined and in Chapter 4, the noise properties were explored.

Chapter 3 described measurements of the sensitivity of a-Se to megavoltage x-rays in which both an x-ray energy and electric field dependence were found. The x-ray energy dependence was unexpected as previously most measurements were made over a relatively small range of diagnostic x-ray energies and the weak energy dependence was masked by experimental uncertainties. Both energy and electric field dependencies were attributed to recombination of electrons and holes. The data were compared to the predictions of two recombination mechanisms, geminate, as described by Onsager theory, and columnar. At high energies, the data was consistent with the predictions of the Onsager mechanism, but as the LET was increased by reducing the energy to the diagnostic range, columnar recombination also contributed. A detailed explanation for our results using a microdosimetric model that combined both mechanisms was provided.

In Chapter 4, we used this information and a Monte Carlo code to model the pulse height spectrum and from it, the zero spatial frequency detective quantum efficiency, DQE(0), of an *a*-Se detector. The model was extended as a function of spatial frequency by examining the mechanisms of image formation. We compared our model to measurement by using a Saticon, a commercial video tube with an *a*-Se target. Excellent agreement between measured and calculated DQE(f) was obtained, further strengthening our finding of an LET dependent sensitivity in Chapter 3. By comparing the predictions of our model to measured data, we concluded that a metal plate + *a*-Se layer of the same mass thickness as a phosphor (e.g. 400 mg/cm^2) would produce a superior image.

In Chapter 5, we produced portal images of both phantoms and a patient using a laser readout of *a*-Se. Although neither the readout nor the sensor were optimized for this application, the *a*-Se images were superior to those from existing approaches, demonstrating the potential for significant improvement.

In summary, the motivation for this work was to determine if *a*-Se could be used as a sensor capable of producing portal images with sufficient quality and resolution for dynamic conformal therapy. A quantum noise limited image up to the at least 0.5 mm^{-1} was required. The DQE(f) curves in Chapter 4 (Fig. 13) show *a*-Se meets this criterion. Moreover, they also show that a metal plate + 400 mg/cm^2 *a*-Se layer will produce an image with better sharpness than a phosphor screen of the same mass thickness. However, these results do not indicate that a phosphor screen is insufficient to meet the needs of conformal therapy. We are only able to conclude that *a*-Se has better resolution than a phosphor, but it remains unclear as to whether the higher resolution is actually necessary. Clearly, from the radiobiological requirements in Chapter 1, either a phosphor or *a*-Se will be sufficient. However, from the perspective of identification of landmarks described in section III.C.2 in Chapter 1, it is unclear if these higher spatial frequencies will permit better detection. Perhaps if the laser readout approach described in Chapter 5 is perfected, it could enable us to answer this question. Moreover, the choice of *a*-Se as a sensor may be useful because it permits easier readout. Some possible readout approaches are described next.

II. FUTURE DIRECTIONS

To satisfy the needs of dynamic conformal therapy, a "real time" ($\geq$ 1 frame/s) readout of *a*-Se is necessary. This thesis has provided the information required to optimize the design of the *a*-Se layer, given the constraints of the particular readout system. Below, a few possible readout mechanisms are outlined.

A. Laser Readout

The air gap PID method is only one of a variety of possible laser readout approaches. By introducing dielectrics to improve coupling between the probe and *a*-Se and by using a parallel readout method, Rowlands and Hunter[7] concluded that it is possible to produce ~ 1 image per second; a rate suitable for portal imaging.

B. Electron Beam Readout

Electron beam readout of *a*-Se was used in Chapter 4 to measure the DQE. A larger area vidicon employing *a*-Se has recently been constructed by Luhta and Rowlands for cardiac fluoroscopy.[7] Unfortunately, the electron beam optics require that the length of the tube be ~ 3 times the diameter of the active area of the tube.[8] For a 40 cm diameter sensor, the vidicon would become too long to be attached to an isocentric linear accelerator for portal imaging. However, cathode ray tubes have been constructed[9,10] in which the scanning electron beam is deflected by 90° just above the target. Adaptation of such beam optics to produce a flatter vidicon could permit electron beam readout to be

used for portal imaging. The results from Chapter 4 suggest that such a system would be quantum noise limited and capable of producing images in real time.

C. Electrometer Readout

A variety of electrometer readouts have been constructed in the past.[11,12] Fallone[11] and his colleagues are currently working on such a system for portal imaging. In a manner similar to the PID method, a small probe is capacitively coupled to the *a*-Se surface. The potential induced on the electrometer is a measure of the surface potential over the area of interest. Since this readout is non-destructive, the probe may be moved over the surface multiple times and the signal can be averaged. The electrometer probe method should be capable of producing images with a very high SNR(0), however, the resolution of this readout, which is approximately[13] equal to the spacing between the probe and the free surface of the *a*-Se, may be poor, since this limit is controlled by the breakdown field of the air between the probe and the free surface of the *a*-Se. For d_{Se}=100 μm at 10 V/μm,[8] the probe must be > 100 μm away. Thus, like the PID approach, significant engineering efforts are required to make good images. In addition, the *a*-Se should be made thick in such a system to maximize the voltage signal, which would in turn reduce the dynamic range.

4. Liquid Crystal Readout

A novel approach being pursued by Reippo and Rowlands[14] is the use of a liquid crystal for readout. Fig. 1 illustrates the idea in which a liquid crystal display is coupled to a layer of *a*-Se. The liquid crystals are sandwiched between two polarizers, thus as light enters, it is polarized in one plane. The liquid crystal molecules rotate the plane of polarization and hence modulate the amount of light that

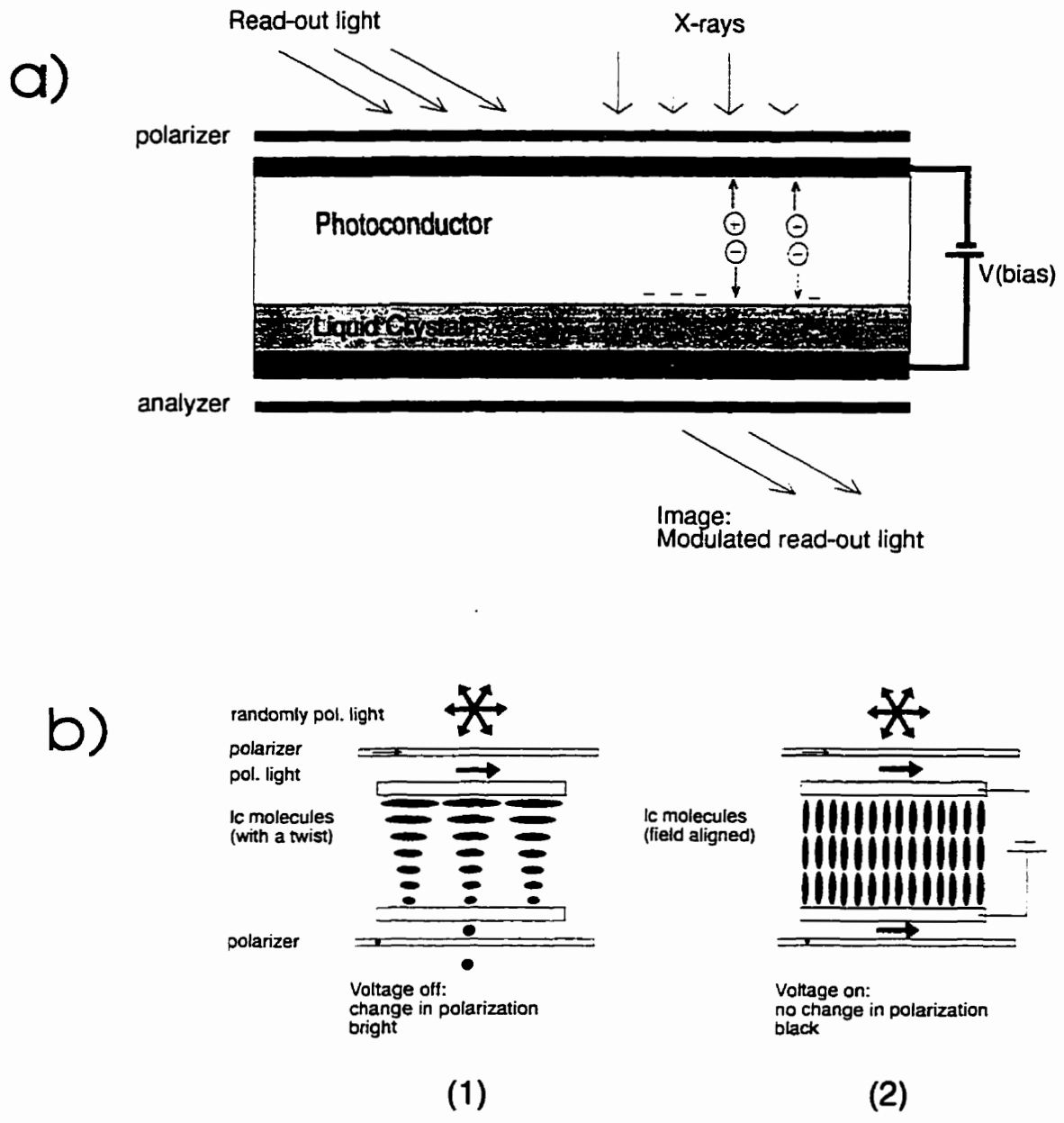

Fig. 1 Illustration of x-ray liquid crystal light valve. (a) Structure of the light valve (b) Operation of the display (1) no potential applied (off) (2) potential applied (on). This figure was provided by P. Rieppo.

exits through the polarizers on the other side. The latent charge image becomes visible since variations in the number of charges on the *a*-Se surface change the field across the liquid crystal molecules which causes them to twist and to modulate the light incident on them differently. Red light is used to view the display (because its energy is less than the band gap of *a*-Se, hence it does not create a signal). Such a sensor could replace the metal plate + phosphor screen in *existing* fluoroscopic portal imagers. Because the liquid crystal acts as a light modulator and does not produce the light directly, any amount of light can be used to readout the image and thus avoid the optical coupling problems found in phosphor based fluoroscopic imagers.

5. Flat Panel Readout

The active matrix flat panel readout method[15,16,17] is a very promising method for diagnostic radiography and fluoroscopy. Essentially, the idea, as illustrated in Fig. 2, is to have a two dimensional array of capacitors with *a*-Se evaporated over it. A thin evaporated counter electrode produces a field across the *a*-Se and the charges that form from x-ray interactions in the bulk produce electrons and holes which migrate to the electrodes on the array. The charges are stored on individual pixels until they are switched, typically by thin film transistors, onto the readout lines. The signals are then amplified, multiplexed and the image is produced. These systems are potentially capable of producing real time (30 frames/s), quantum noise limited images with good resolution (e.g. ~100 μm pixels). Alternative flat panel imagers which use a phosphor, photodiode and thin film transistor have been shown to produce conventional portal images comparable to digitized films[18] and will compete with the *a*-Se devices. Depending upon the material used to produce the transistor array and readout electronics, radiation damage may limit the lifetime of the device.[19,20,21,24] Since this type of detector currently has the greatest commercial interest and since it can be made slim and read out in

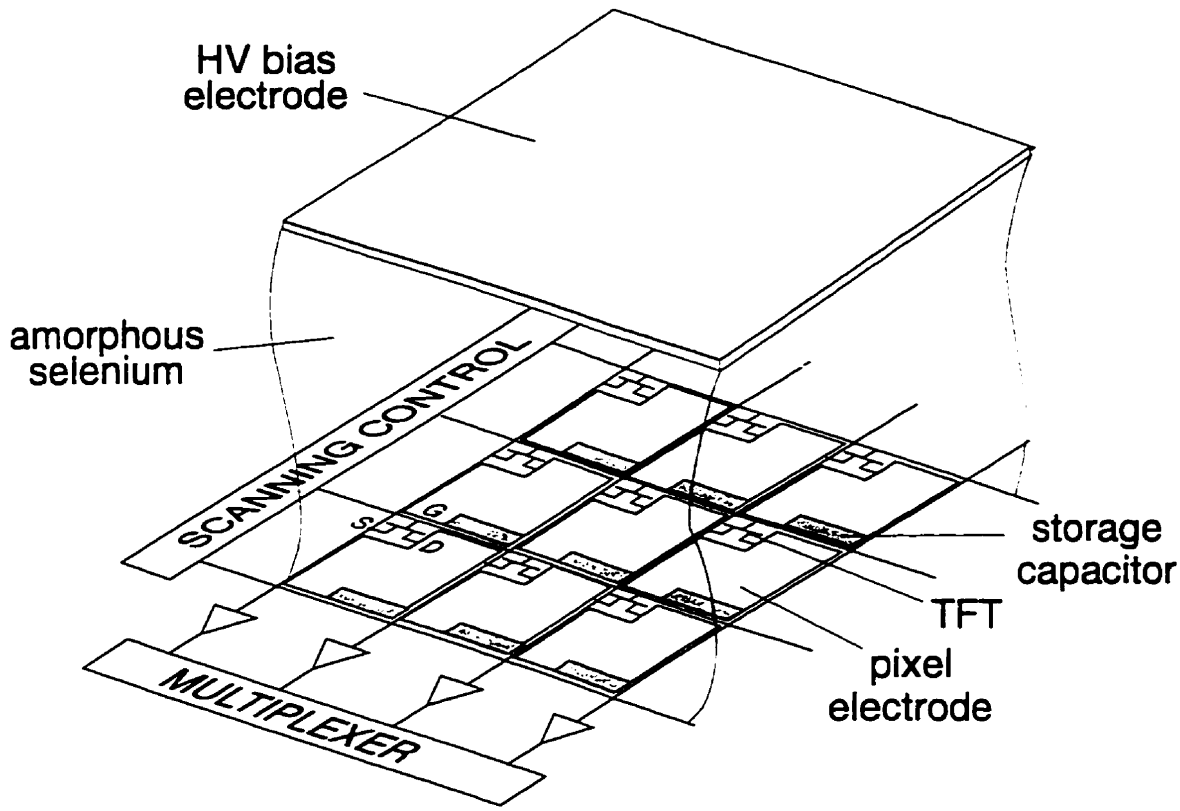

Fig. 2 Schematic illustrating a plat panel active matrix readout of a-Se. The bias electrode establishes a field of ~ 10 V/um. Charges are collected on the pixel electrodes and switched by thin film transistors (TFTs) to the readout rails into a multiplexer. Figure courtesy of W. Zhao.

real time, at the point of writing, it appears to be the most likely future readout technology. Assuming a 500 μm *a*-Se layer with a field of 10 V/μm, a 0.3 mm pixel, a readout rate of 30 frames/s, a dose rate of 5 R/s, and using the results of Chapters 3 and 4, the total signal should be ~ 10^8 electrons/pixel, with a corresponding quantum noise of ~$2x10^6$ electrons/pixel which is much greater than the readout noise of ~10^3 electrons/pixel of one such system,[21] thus, this approach could easily be made quantum noise limited.

While it appears likely that flat panels will become the dominant readout technology for x-ray transmission radiography and fluoroscopy, any of the above approaches may have applications in portal imaging in the future. There is little doubt that *a*-Se can play an important role in both the radiology and radiation therapy departments of the future. It is the author's hope that this work will contribute to the construction and design of such devices to aid in the implementation of conformal therapy and improve patient survival.

REFERENCES

1. A. Ezz, P. Munro, A.T. Porter, J. Battista, D.A. Jaffray, A. Fenster and S. Osborne, " Daily monitoring and correction of radiation field placement using a video-based portal imaging system: A pilot study," *Int. J. Radiat. Oncol. Biol. Phys.*, **22**, 159-165 (1992).

2. B. Wowk and S. Shalev, "Thick phosphor screens for on-line portal imaging," *Med. Phys.*, **21**, 1269-1276 (1994).

3. R.A. Buchanan, A.F. Sklensky, T.G. Maple, and H.N. Bailey, "Metal-phosphor intensifying screens for high energy imaging applications," *IEEE Trans. Nucl. Sci*, **NS-21**, 692-694 (1974).

4. T. Radcliffe, G. Barnea, B. Wowk, R. Rajapakshe, and S. Shalev, "Monte Carlo optimization of metal/phosphor screens at megavoltage energies," *Med. Phys.*, **20**, 1161-1169 (1993).

5. D.A. Jaffray, J.J. Battista, A. Fenster, and P. Munro, "Monte Carlo studies of x-ray energy absorption and quantum noise in megavoltage transmission radiography," *Med. Phys.*, **22**, 1077-1088 (1995).

6. B. Wowk, T. Radcliffe, K.W. Leszczynski, S. Shalev and R. Rajapakshe, "Optimization of metal/phosphor screens for on-line portal imaging," *Med. Phys.*, **21**, 227-235 (1994).

7. R. Luhta, Ph.D. thesis, University of Toronto, 1997.

8. G. Pang, R. Luhta, and J.A. Rowlands "Lens design for large area x-ray sensitive vidicons," (submitted to Medical Physics, 1996).

9. D. Gabor, P. Stuart, and P. Kalman, "A new cathode-ray tube for monochrome and colour television," *Proc. IEEE Part B*, **105**, 581 (1958).

10. W.R. Aiken, "A thin cathode-ray tube," *Proc. I.R.E.*, **45**, 1599 (1957).

11. W. Hillen, S. Rupp, U. Schiebel, and T. Zaengel, "Imaging performance of a selenium-based detector for high-resolution radiography," *Proc. SPIE*, **1090**, 296-305 (1989).

12. L.S. Jeromin and L.M. Klynn, "Electronic recording of x-ray images," *J. Appl. Photo. Eng.*, **5**, 183-189 (1979).

13. R.M. Schaffert, *Electrophotography*, (Focal Press, London, 1980) pp. 424-427.

14. P. Rieppo and J.A. Rowlands, "X-ray imaging with amorphous selenium: Theoretical feasibility study of a liquid crystal light valve for digital radiography," (submitted to *Med. Phys.* November 1996).

15. W. Zhao and J.A. Rowlands, "X-ray imaging using amorphous selenium: Feasibility of a flat panel self-scanned detector for digital radiology," *Med. Phys.*, **22**, 1595-1605 (1995).

16. D.L. Lee, L.K. Cheung, and L.S. Jeromin, "A new digital detector for projection radiography," *Proc. SPIE*, **2432**, 237-249 (1995).

17. L.E. Antonuk, J. Boudry, W. Huang, D.L. McShan, E.J. Morton, J. Yorkston, M.J. Longo, and R.A. Street, "Demonstration of megavoltage and diagnostic x-ray imaging with hydrogenated amorphous silicon arrays," *Med. Phys.*, **19**, 1455-1466 (1992).

18. L.E. Antonuk, J. Yorkston, W. Huang, H. Sandler, J.H. Siewerdsen and Y. El-Mohri, "Megavoltage imaging with a large-area, flat panel, amorphous silicon imager," *Int. J. Radiat. Oncol. Biol. Phys.*, **36**, 661-672 (1996).

19. L.E. Antonuk, J. Boudry, J. Yorkston, C.F. Wild, M.J. Longo, and R.A. Street, "Radiation-damage studies of amorphous-silicon photodiode sensors for applications in radiotherapy x-ray imaging," *Nucl. Instr. Meth.*, **299**, 143 (1990).

20. J. Boudry and L.E. Antonuk, "Radiation damage of amorphous silicon, thin film, field-effect transistors," *Med. Phys.*, **23**, 743-754 (1996).

21. W. Zhao, D. Waechter, and J.A. Rowlands, "Radiation hardness of CdSe thin film transistors," (to be submitted to *Med. Phys.* 1997).

IMAGE EVALUATION
TEST TARGET (QA-3)

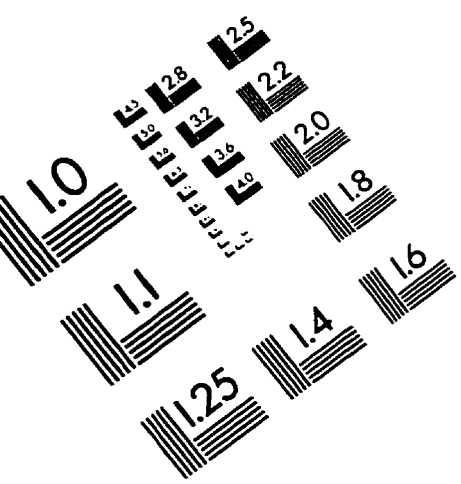

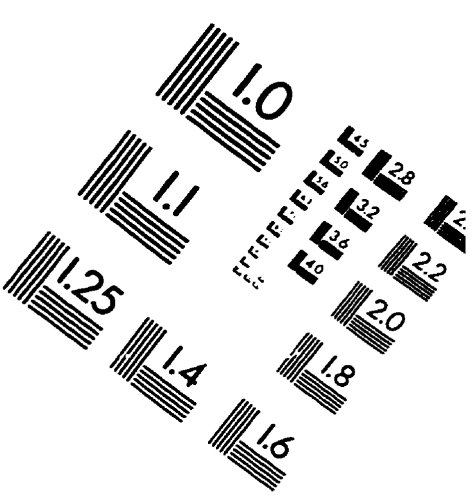

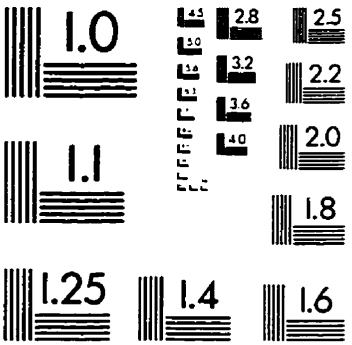

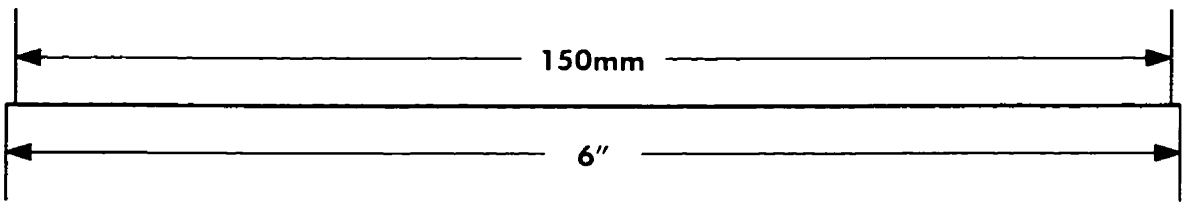

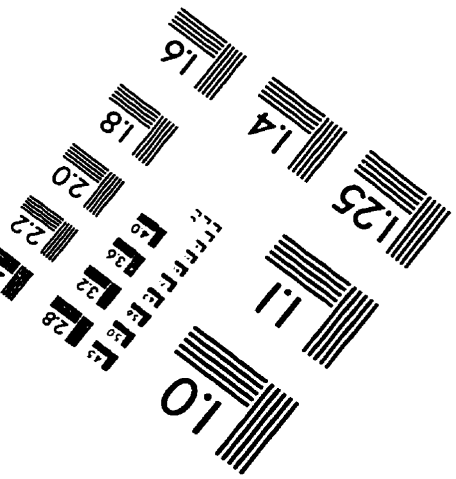

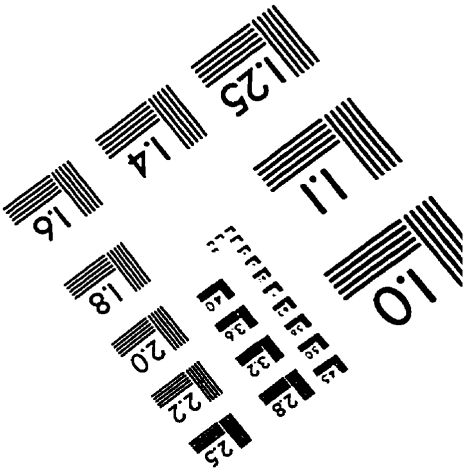

APPLIED IMAGE, Inc
1653 East Main Street
Rochester, NY 14609 USA
Phone: 716/482-0300
Fax: 716/288-5989